UNIVERSITY
OF OSLO

Master Thesis

Quinizarin as Organic Sensitizer in LnF_3 Thin Films for Photon Upconversion

Erlend Tiberg North

Materials Science for Energy and Nanotechnology
60 credits

Department of Chemistry
Faculty of Mathematics and Natural Sciences

“When light gives you red, make blue”

2022

Quinizarin as Organic Sensitizer in LnF_3 Thin Films for Photon Upconversion

Erlend Tiberg North

http://www.duo.uio.no/

Printed at Reprosentralen, University of Oslo

Abstract

This thesis illuminates the opportunities for Quinizarin (Qz) as an organic sensitizer in LnF_3 (Ln=Y, Nd, Tm, Yb) thin films for upconversion. Lanthanides show great promise as active materials for upconversion technologies, but struggle with very low absorption and thus, very low efficiency. We attempt to correct this by including a broad band absorber, in our case an organic dye. Atomic layer deposition (ALD) has been used to build the multilayered structures with control of the interatomic separations.

The project has been divided into multiple parts, focusing first on Qz as sensitizer and its properties in solid state by ALD growth of Ln_2Qz_3. The ALD growth of LnF_3 thin films was investigated and multilayered structures intended to show upconversion was made. Initial investigations of Qz show that as a dispersed molecule, its luminescence is heavily influenced by its environment, but indicates it could function as a sensitizer. When combined with $Ln(thd)_3$ as a precursor in ALD growth, it shows exceptionally good growth with high growth rate, as well as high optical absorption.

The growth and structure of LnF_3 thin films using NH_4F as fluorine source has been characterized using quartz crystal microbalance (QCM), with results indicating similar type of growth among all the tested lanthanides, apart for Nd, which proved more challenging. Uniform film with growth rates of around 0.6 Å/cycle were achieved, and NH_4F has been proven a good fluorine source in LnF_3 systems using $Ln(thd)_3$. Qz has been successfully incorporated into these films with high absorption for high Qz-content, as characterized by using ultraviolet, visible and near infrared spectroscopy (UV-Vis). However, the films were not luminescent, as aimed for, proving that there is more work to be done to understand the quenching mechanisms involved.

The upconversion structure itself has been investigated by growing and investigating multilayers of YbF_3 with Nd^{3+} and Tm^{3+}. Using cathodoluminescence (CL) both ions have been shown incorporated in the structure. The system shows different emission intensities depending on ion distance, with 0.8 nm being the most optimal for CL signal.

Acknowledgements

This thesis was submitted for the degree of Master of Science (MSc.) in Materials Science for Energy and Nanotechnology (MENA). The work was performed at the Nanostructures and Functional Materials (NAFUMA) group at the Department of Chemistry, Faculty of Mathematics and Natural Sciences, at the University of Oslo (UiO) from August 2020 to May 2022.

The biggest contributions were from my main supervisor Prof. Ola Nilsen and co-supervisor Dr. Per-Anders Stensby Hansen. To Per-Anders, thank you for your invaluable insight in all things optical, and continued support even after leaving UiO. You have been a joy to learn from. To Ola, your tireless dedication to the success of others have been a true inspiration. I will be forever grateful for your support and our frequent meetings and discussions.

The entire NAFUMA-group has given good insight, but especially the film group. I would like to thank the following for both scientific and moral support: Bhagyesh Purohit, Veronica Killi, Henrik Sønsteby, Melania Rogowska and Vegard Rønning.

Thank you to my fellow MENA-masters, who have been there from start to finish. I would like to especially thank Casper for in sharing both the pain and his input on design, and Amund and Ina for entertaining discussions. Thank you to Ola, Marlene and Kari for lunch breaks, Mats for ALD-companionship and Henry for the best jokes. A final thank you to Linn for giving me light when my thin films did not. You are a shining star and can accomplish anything you set your mind to.

Thank you to friends and family for supporting all my endeavors, and for listening to my science talks even if you do not understand them. It has been fun to lead student councils and my Dungeons & Dragons-groups has been an excellent break from studying. Thank you to my sister for her support and insight, dad for being proud of my accomplishments and mom for endless love and cheering me over the finish line.

Erlend Tiberg North

University of Oslo, May 2022

List of Abbreviations

acac	acetylacetonate
ACQ	Aggregation-Caused Quenching
AFM	Atomic Force Microscopy
AIE	Aggregation-Induced Emission
ALD	Atomic Layer Deposition
CL	Cathodoluminescence Spectroscopy
CVD	Chemical Vapor Deposition
EMU	Energy Migration-Mediated Upconversion
ESA	Excited State Absorption
ETU	Energy Transfer Upconversion
FTIR	Fourier-Transform Infrared Spectroscopy
GPC	Growth Per Cycle
Hfac / Hhfac	1,1,1,5,5,5,-hexafluoro-pentane-2,4-dione
HSE	Health Safety Environment
LED	Light Emitting Diode
Ln / Ln^{3+}	Lanthanide ion
MBE	Molecular Beam Epitaxy
MENA	Materials Science for Energy and Nanotechnology
MLD	Molecular Layer Deposition
MSc.	Master of Science
NAFUMA	Nanostructures and Functional Materials
NIR	Near infrared
OLED	Organic Light Emitting Diode
PL	Photoluminescence Spectroscopy

PLD	Pulsed Laser Deposition
QCM	Quartz Crystal Microbalance
Qz	Quinizarin (1,4-Dihydroxyanthraquinone)
RIM	Restriction of Intramolecular Motion
RMS	Root Mean Square
SE	Spectroscopic Ellipsometry
SPM	Scanning Probe Microscopy
Thd / Hthd	2,2,6,6-tetramethyl-3,5-heptadione ligand / protonated version
TMA	Trimethylaluminium / $Al(CH_3)_3$
ToF-ERDA	Time-of-Flight Elastic Recoil Detection Analysis
UiO	University of Oslo
UV	Ultraviolet
UV-Vis	Ultraviolet, Visible and Near Infrared Spectroscopy
XPS	X-ray Photoelectron Spectroscopy
XRD	X-Ray Diffraction
XRR	X-Ray Reflectivity

Frequently Mentioned Structures

Compound	Chemical formula	Chemical structure
Al(acac)$_3$	$Al(C_5H_7O_2)_3$	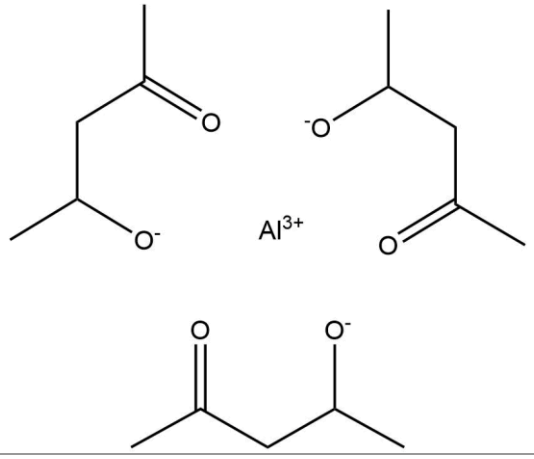
Ammonium fluoride	NH_4F	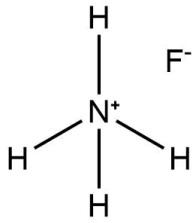
Nd(thd)$_3$	$Nd(C_{11}H_{19}O_2)_3$	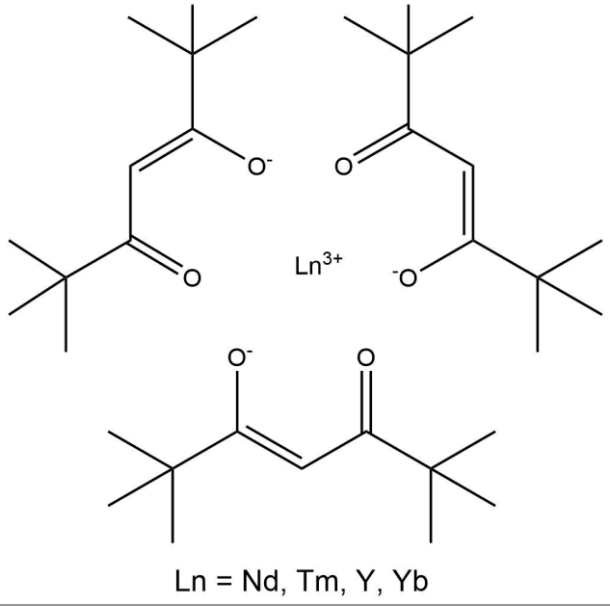 Ln = Nd, Tm, Y, Yb
Tm(thd)$_3$	$Tm(C_{11}H_{19}O_2)_3$	
Y(thd)$_3$	$Yb(C_{11}H_{19}O_2)_3$	
Yb(thd)$_3$	$Y(C_{11}H_{19}O_2)_3$	

Quinizarin	$C_{14}H_8O_4$	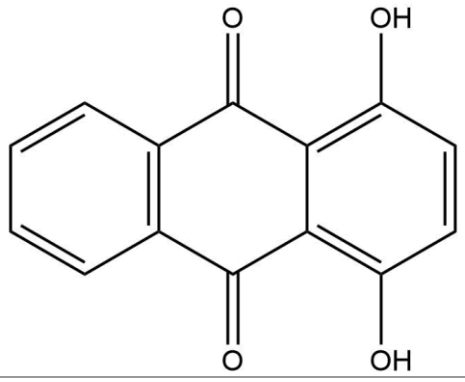
TMA	$Al(CH_3)_3$	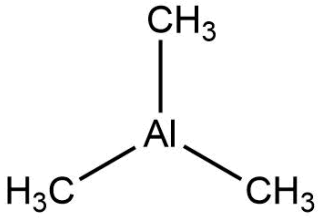

Contents

1 Introduction

1.1 Motivation

With today's climate crisis, scientists all over the world are scrambling to develop technologies that can reduce costs, climate footprints and power consumption. Meanwhile, an increasing world population and demands for increased economic standards causes a higher pressure for developing technologies that can improve living standards, often without compromising for the above. The COVID-19 pandemic is also a reminder that while technologies keep progressing, emerging viruses and bacteria remain a threat and demands further research in antibacterial materials.

One concept showing great promise for use in many technologies is photon upconversion. It can be used to create materials with bactericidal properties, by converting visible light to ultraviolet (UV) that can kill bacteria or viruses [1, 2]. When applied in photovoltaics, upconversion converts light that otherwise would be wasted into suitable energy to bridge the band gap in solar cells [3, 4]. In photocatalysis, the high energy emitted from upconversion systems can provide the required energy to pass the activation barrier for reactions, such as water-splitting for hydrogen production [5]. It can enable the use of extreme-UV lithography, allowing to further decrease the feature size of microelectronic devices, improving their efficiency [6]. In the production of high energy UV-lasers or -diodes, photon upconversion can reduce costs by producing UV light from cheap and efficient visible or near infrared light diode sources [7].

However, upconversion systems are not easily obtainable or highly efficient. One challenge with upconversion systems today is their sensitivity to the concentrations of the active materials, leading to concentration quenching. There is a fine balance between having just enough active material to provide an efficient upconversion system, while minimizing the alternative losses leading to reduced efficiency. To limit such losses requires fine-tuned structures to control interatomic distances [8, 9]. This means good control of the synthesis of such materials is crucial. Another issue is that most upconversion systems are based on lanthanides that themselves absorb light rather poorly, leading to inefficient processes. This calls for combining these with

something else that can absorb the light required for the lanthanide upconversion system [10, 11].

1.2 Thesis Objectives

The ultimate goal of this project is to create upconverting structures based on LnF_3 thin films as activators and emitters with an organic dye as sensitizer to increase the absorption of broadband wavelengths. A sensitizer is a molecule that can absorb light and transfer it to the upconversion system. By choosing a sensitizer with a broad absorption band we can increase the efficiency of lanthanide-based upconversion systems in these broadband light conditions. The thin films will be made using the ALD technique, a gas phase deposition-based process suitable for construction of layered structures with atomic precision. Lanthanides are great elements for upconversion, but their absorption bands are weak and narrow, leading to lower efficiency when excited using broadband light. This is where organic dyes prove useful for the project, as they have wide absorption bands and much higher absorption strengths.

This project is in large part based on the work of Silje Holm Sørensen, who investigated different perylenes as sensitizers in in the same upconversion systems [12]. For this project, the organic dye known as Quinizarin (1,4-Dihydroxyanthraquinone) will be used, and from here on it will be referred to as Qz. The project is divided into multiple parts.

The first steps are to investigate whether Qz is suitable as a sensitizer for upconversion systems made by ALD. The dye has previously been examined in a similar setting in combination with aluminium [13], proving that Qz can be used as a reactant by ALD, as well showing sensitizing qualities. However, here it will be explored as a reactant in combination with the less reactive lanthanide precursors.

The second main part of the project will be the exploration of deposition of LnF_3 films, where Ln=Y, Nd, Tm and Yb, using NH_4F as fluorine source. These films will lay the foundation for incorporating Qz in fluorides as part of an upconversion system. NH_4F has been used as an ALD precursor before, both for LnF_3, and for other thin films, though it is still not widely used [6, 12, 14, 15]. Qz-doped LnF_3 thin films will be investigated for sensitizing properties, and films of YbF_3:Nd,Tm will be explored with

varying spacing between the Nd and Tm layers to study the upconversion system itself. Finally, the goal is to deposit a film of our upconversion system with Qz incorporated as a sensitizer. The following sections will give an overview of concepts utilized in the project, with emphasis on their history and previous work.

1.3 Atomic Layer Deposition (ALD)

ALD is a thin film synthesis technique that separates itself from other thin film techniques in how it deposits highly controlled and uniform films by exposing the substrate to the precursors in a sequential manner. This opens for self-limiting growth, which can provide utmost control of deposited material.

1.3.1 Background

The ALD principle was discovered in the Soviet Union in the 1960s, although not disclosed to the western part of the world until after the collapse of the union. The technique is therefore better known to us as developed by Tuomo Suntola in Finland in the 1970s to solve the challenges in formation of electroluminescent thin film display devices [16], and was patented in 1977 [17]. ALD has a long background related to luminescence, but has since then, become increasingly more applied in many technologies, particularly in microelectronics [18, 19]. The technique is known by many names, one of them being Molecular Layer Deposition (MLD), when instead of atoms, whole molecules are deposited. Our deposition of Qz-based materials is technically MLD rather than ALD, but throughout the thesis the method will be referred to as ALD for ease of understanding.

1.3.2 ALD of Lanthanides

Though a few lanthanides have already been deposited as fluorides, they are most commonly known deposited as oxides. Numerous reports have been made about deposition of lanthanides by ALD[20, 21], while Hansen et al. published a study of all the optically active lanthanides (Pr, Nd, Sm, Eu, Tb, Dy, Ho, Er, Tm, Yb) in 2013, where the optical properties of their oxide films were provided, along with sublimation temperatures of $Ln(thd)_3$ (thd = 2,2,6,6-tetramethyl-3,5-heptadionedionate) precursors [22].

LnF_3 thin films by ALD have not been as widely explored, but some work has been done as presented in Table 1.1, where YF_3 is included for completeness.

Table 1.1: Thin films of LnF_3 deposited by ALD with their GPC, deposition temperatures and source article.

Product	Cation precursor	Anion precursor	GPC [Å/cycle]	Deposition temperature [°C]	Reference
YF_3	$Y(thd)_3$	TiF4	1.3 at 250 °C	175 – 325	[23]
LaF_3	$La(thd)_3$	TiF_4	5.2 at 250 °C	225 – 350	[24]
GdF_3	$Gd(thd)_3$	NH_4F	0.2 at 300 °C	275 – 375	[6]
TbF_3	$Tb(thd)_3$	TiF_4	0.8 at 300 °C	175 – 350	[25]

Atosuo et al. studied growth of TbF_3 and GdF_3 and found low impurities of H, C, N and O, with nearly constant growth per cycle (GPC) for GdF_3 by NH_4F as fluorine source in contrast to TbF_3 using TiF_4 as fluorine source where the growth rate decreased with increasing temperatures [6, 25]. YF_3 and LaF_3 are similar to TbF_3 in impurities and changes in growth rate [23, 24]. All LnF_3 films show an increase in crystallinity with increasing temperatures.

1.3.3 ALD of Fluorides

Fluorides are transparent in UV and their low refractive index is an advantage in applications related to optics [26]. They also have low phonon energies, being an advantage over oxides. Having low phonon energies decreases the chances of multiphonon relaxation, which in turn increases upconversion efficiency. This will be elaborated on in 2.1.1. These properties have led to the choice of fluoride as the matrix for this project. Fluoride thin films have been deposited with many different types of precursors by ALD, and we can divide them into different categories.

The first category uses HF as the actual fluoride source. One of the simpler precursors is to use pure HF gas, however, it poses a high health, safety and environment (HSE) risk. HF-pyridine has also been used as a fluoride precursor [27]. The precursor is a liquid at room temperature allowing for safer use than gas cylinders of HF, having a boiling point of 19.5 °C. The precursor of choice for this project is NH_4F. It was already used as a precursor in 1994 for synthesis of fluorides of Ca, Sr and Zn [28]. NH_4F

decomposes to HF and NH_3 between 260 and 400 °C. Since it decomposes locally in the reactor chamber the risks are smaller during handling of the precursors.

The second category uses metal fluorides that decompose and react via a ligand exchange reaction in the reaction chamber, releasing F for growth. A widely used precursor is TiF_4, as used in deposition of LaF_3, YF_3 and TbF_3 with $Ln(thd)_3$ as cation precursor [23-25]. It can give a high growth rate, but there is a risk of Ti impurities, which can lead to quenched emission in luminescent thin films. This is due to a charge transfer between Ti^{4+} and certain Ln^{3+} ions [29]. Another example is TaF_5, which was reported to provide better transparency at high growth temperatures than TiF_4 in the deposition of MgF_2 [30].

The third category uses compounds as plasma to grow fluorides. SF_6 plasma has been explored in deposition of both LiF and AlF_3, with results indicating that the plasma reacts with the ligands and/or surface, favoring short pulse times. Nevertheless, it is presented as a promising precursor as an alternative to the aforementioned metal fluorides and pure/mixed HF [31, 32].

The final category uses organofluorines. 1,1,1,5,5,5,-hexafluoro-pentane-2,4-dione (Hfac or Hhfac) has been used in the deposition of multiple compounds. Putkonen et al. used ozone to activate Hhfac on the surface, while reporting less than 2 at.% of O [33]. Tiruin et al. used Hhfac in the deposition of LiF and found formation of an LiF-CF_x hybrid layer [34].

1.3.4 Hybrid thin films

Hybrid thin films consist of both organic and inorganic molecules. One of the first hybrid thin films synthesized with ALD was deposited in 2004 by Nilsen et al. [35]. Hybrid films have been of increasing interest since the late 2000s, and applications include amongst others sensors, protective coatings and solar cell applications [36].

Luminescent hybrid films are quite novel. An upconverting hybrid film with Yb and Er was deposited by Tuomisto et al., but the organic molecule did unfortunately not act as a sensitizer [37]. This work did, however, show that hybrid films for upconversion can be made with organic molecules and lanthanides.

1.4 Luminescence and Optical Conversion

Luminescence is light emission from a material with origin from any process other than black-body, also known as heat, radiation. Some types of luminescence are chemiluminescence (excitation from a chemical reaction), electroluminescence (excitation from an applied voltage) and photoluminescence (excitation from absorbed light). Materials exhibiting photoluminescence are known as phosphors, owing its name to the element of phosphorus. Phosphorus was the first material discovered to exhibit luminescence, not by photoluminescence, but rather by chemiluminescence under the oxidation of phosphorus in air [38].

Plasma display panels, fluorescent lamps, light emitting diodes (LEDs) and organic light emitting devices (OLEDs) are all technologies where luminescence is used. They rely on either electro- or photoluminescence to excite an electron from a low-energy state, typically the ground state, to higher-energy excited state. The electron will then de-excite, releasing energy in form of a photon. The wavelength of this photon depends on the energy gap between the excited and de-excited state, and this wavelength can be tuned by changing the host lattice or ions that the phosphor consists of. The ions can serve different purposes, but where an ion is the source of the emitted photon it is called an activator. Often there are ions that are optimized for absorbing incoming energy and transferring it on to the activator. These are known as sensitizers, and are generally used in optical conversion processes [39].

1.4.1 Optical conversion

Optical conversion is the concept of absorbing one wavelength of light and emitting another. This is part of photoluminescence, and can be divided into down- and upconversion, both of which are visualized in Figure 1.1. In downconversion, short-wavelength photons are converted into more than one longer-wavelength photon. If there is only one outgoing photon, we call it downshifting. Upconversion is the process where multiple longer-wavelength photons are converted into short-wavelength photons.

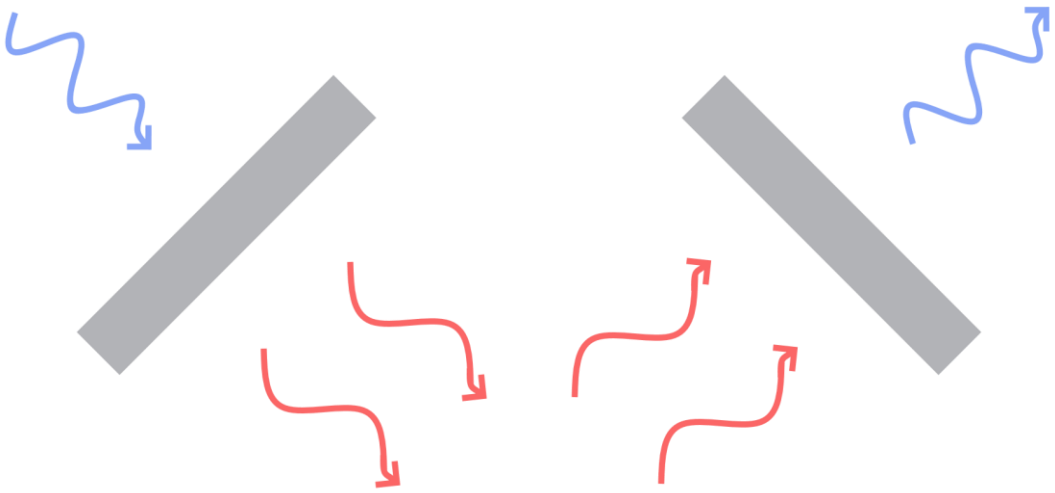

Figure 1.1: A photon of high energy transforms into two photons of lower energy by downconversion (left). Two photons of lower energy transform into a photon of higher energy through upconversion (right).

Downconversion materials are also known as quantum-splitting or multiphonon-emitting phosphors and are important to, amongst others, display and lighting industries. Quantum-splitting phosphors that convert gamma and X-rays to visible light are known as scintillators and play an important role in detector systems where their emitted light is used by photosensitive devices.

As previously mentioned, upconversion materials have many use-cases. Both up- and downconversion materials can be made by rare earth metals, and fluorides are not an uncommon form to find them in [39].

1.5 Previous Work with LnF_3 and Upconversion

Lanthanide fluorides have been used for upconversion before, but has not been explored much with ALD. This subchapter will present an overview the most relevant work done on lanthanide fluorides for upconversion and as thin films, as well as provide an overview of upconversion thin films and organic sensitization in these.

1.5.1 LnF_3 Nanoparticles for Upconversion

Lanthanide-doped fluoride nanoparticles for upconversion often consist of a core-shell structure [40-42]. Here, the activator ion is generally in the core of the nanoparticle, while the absorbers/sensitizers, often Yb^{3+}, are located in the shell. By separating the optically active ions with an inactive host lattice material, concentration quenching can be prevented. LaF_3 nanoparticles doped with various Ln^{3+} were investigated by Stouwdam et al. and showed good tuning of emission wavelength by changing the dopant [43]. By using Yb^{3+} as sensitizer in LaF_3:Er^{3+}, they managed to increase the Er^{3+} emission by 20%. Nanoparticles of lanthanide-doped $NaYF_4$ are rather popular being one of the most efficient upconverting materials known [40]. These particles have been studied by attaching various ligands and surfactants for controlling and studying their activity with various sizes and morphology [44].

Upconversion nanoparticles often struggle with low efficiency, with effects from size and surface being more impactful than for bulk materials [45]. A way to increase this efficiency is by using organic molecules that can better absorb the incoming light. However, this approach has been proven difficult as there is little control the density of organic molecules on the particle surface, and they show low stability [11]. Nanoparticles also struggle where the activator is in the core of a core/shell nanoparticle, as the emitted light must travel past the absorbing layer. This is not a problem in thin films, as the absorbing layer can be placed on either side of the structure, and transparent substrates can be used [12]. The work of Hansen et al. showed that optical conversion materials can be deposited as thin films with ALD, and also shows promise with organic dyes as sensitizers to increase the absorption [15].

1.5.2 Thin Films for Upconversion

Upconversion thin films have been synthesized before with various techniques, but is not widely explored with ALD [46]. As examples, pulsed laser deposition (PLD) has been used to deposit $LaEr(MoO_4)_3$ thin films with upconversion from near infrared (NIR) to visible light [47]. Using molecular beam epitaxy (MBE) LaF_3:Nd^{3+} has upconverted NIR to UV [48]. Other methods include spin-coating, which have been used to create some lanthanide-doped thin films and were able to avoid the deteriorating heat treatment that typically leads to clustering of the lanthanides and concentration quenching [49]. ALD has been used to create luminescence with Er-doped Al_2O_3 thin films [50], though organic sensitization with ALD is not widely used.

1.5.3 Organic Sensitized Upconversion Thin Films

There has been done work on organic sensitizers in lanthanide luminescence systems [51]. Organic sensitization for thin films using ALD not deeply explored but is gaining traction. Gieraityte et al. has reported blue, red and red upconversion using a hybrid Ln-pyrazine thin film [52].

There is some experience in our research group, where Hansen et al. has shown promise with the development of a multilayered organic-inorganic nanocomposite with successful aromatic sensitization. [15]. Luminescent films using Tb-doped TiO_2 were made with terephthalic acid as sensitizer for downshifting, but no transfer between was obtained [53]. Sørensen worked on our same upconversion system with perylenes as sensitizer, but did not observe any luminescence [12].

2 Theory and Methods

This chapter provides an overview of the optical properties of lanthanides, along with the transfer mechanisms of the proposed upconversion system. The theory of ALD, the deposition technique of choice, will be explained, and the relevant aspects of the characterization methods used in the project will be presented.

2.1 Optical Properties of Lanthanides

Lanthanides are good candidates for upconversion of photons, as previously alluded to in 1.2. The 4f-orbitals of these elements contain optically relevant electronic states that are not bonding, as outer shells of 5s and 6s shield the 4f-orbitals [Ronda (luminescence-book)]. This results in f-orbitals that do not change with its surroundings. As a consequence of this, lanthanides also have sharp absorption- and emission lines. This, combined with their environmental insensitivity, makes them suitable as phosphors when used as dopants in other materials.

The f-f transitions in lanthanides are parity forbidden according to the Laporte rule since the transition does not lead to a change in symmetry. However, the transitions become partially allowed due to small shifts in the ligand field that give rise to asymmetry. These shifts are quite small due to the lanthanides' insensitivity to their environments. Partially allowed transitions leads to long enough lifetimes to allow energy transfer to occur rather than losing it to multi-phonon relaxation, but also means that lanthanides have weak absorption. Figure 2.1 shows an energy level diagram for the lanthanides with luminescent properties relevant for upconversion.

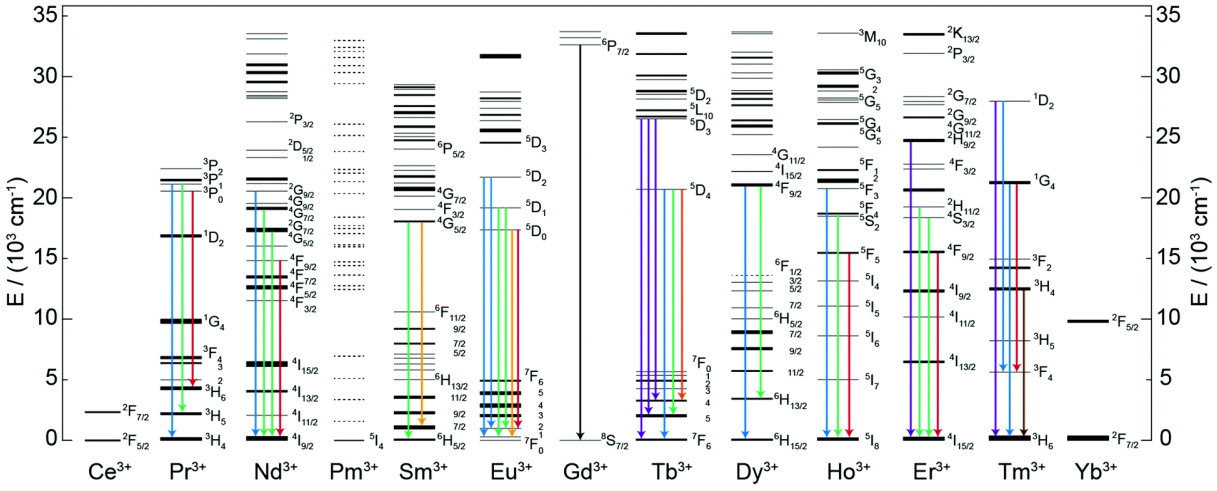

Figure 2.1: Partial energy level diagram of lanthanide ions commonly used for upconversion. Typical radiative transitions are highlighted. From [54].

To optimize our system, it is useful to know the mechanisms that may lead to upconversion, and the alternative mechanisms that rather lead to non-radiative loss. The theory for such mechanisms is well described by [39] and [9]. A brief extraction is given in the following subchapters.

2.1.1 Efficiency- and Loss Mechanisms

The Quantum Efficiency of a photoluminescent system is given as the number of photons generated per incoming photons and is given in Equation (2.1).

$$\eta = \frac{(1-r)[h\nu]}{\beta E_g} \cdot \eta_t \eta_{act} \eta_{esc} \tag{2.1}$$

where r is the backscatter coefficient, accounting for photons that are scattered by the surface do not enter the material, $h\nu$ is the average photon energy of the emitted photons, βE_g is the energy needed to create an electron-hole pair, η_t is the efficiency of the transfer from sensitizer to activator in a photoluminescent system, η_{act} is the quantum efficiency of the activator and η_{esc} is the probability that generated photons will escape the material.

The quantum efficiency includes all possibilities for interactions of an incoming photon with the material, and includes the following mechanisms for loss:

1. The absorbed energy is not transferred to the luminescent ion (η_t)
2. The energy is transferred, but leads to non-radiative decay (η_{act})
3. The generated photon is reabsorbed by the system (η_{esc})

The first mechanism for loss arises when energy absorbed by the sensitizer is lost rather than being transferred to the activator. It can for example be re-emitted or quenched before transferring. By ensuring that our sensitizer ion emits at wavelengths that our absorbing ions can absorb and adjusting the distance between them we can minimize this loss.

The second mechanism comes from cases where the energy that reaches the activator is not emitted. It can for example be lost to multiphonon relaxation, concentration quenching or absorption by an impurity. The loss can be minimized by choosing a host lattice with low phonon energies and activator ions with large enough energy gaps to avoid multiphonon relaxation. Generally, this energy gap should be wider than he energy of 5 phonons, which shows that low phonon energies will allow for a wider selection of activator ions. Controlling the concentration of activator ions and avoiding impurities will work positively on avoiding concentration quenching and unwanted absorption.

The third mechanism can be minimized by choosing a host lattice that does not absorb at the same wavelengths as the generated photons. This is normally not a problem for lanthanide systems, as they are weakly absorbing, but since we use an organic dye, the likelihood increases, and we should make sure the organic dye does not absorb the luminescence.

In order to promote energy transfers and avoid loss, understanding the mechanisms behind transferring energy is beneficial.

2.1.2 Energy Transfer Mechanisms

For the absorbed energy to reach our activator and lead to luminescence we need the energy to be transferred from the sensitizer and through the system.

Energy transfer can originate from either electrostatic or exchange interactions. Both require an overlap in the emission and absorption spectrums for the sensitizer and the activator ion, but only exchange interaction requires a physical overlap of atomic orbitals. In coulomb interaction, the sensitizer transfers energy to the activator by creating dipole or quadrupole oscillations at the activator. If R_{SA} is the distance between sensitizer and absorber, a dipole-dipole interaction decays proportionally to R_{SA}^{6}, dipole-quadrupole with R_{SA}^{8} and quadrupole-quadropole with R_{SA}^{10}. The ranges of these interactions become 3.5, 0.8 and 0.2 nm, respectively. Where Exchange interaction consists of a physical exchange in electrons. The sensitizer transfers an excited electron to the activator, while the activator transfers a lower energy-state electron in return. The energy transfer here is proportional to $exp(-R_{SA}/L)$, with L being determined by the van der Waals radii of the interacting ions. Due to this dependance, the rate for exchange interactions drops very quickly when distance is larger than 1 nm. by These energy transfer mechanisms are visualized using energy diagrams in Figure 2.2.

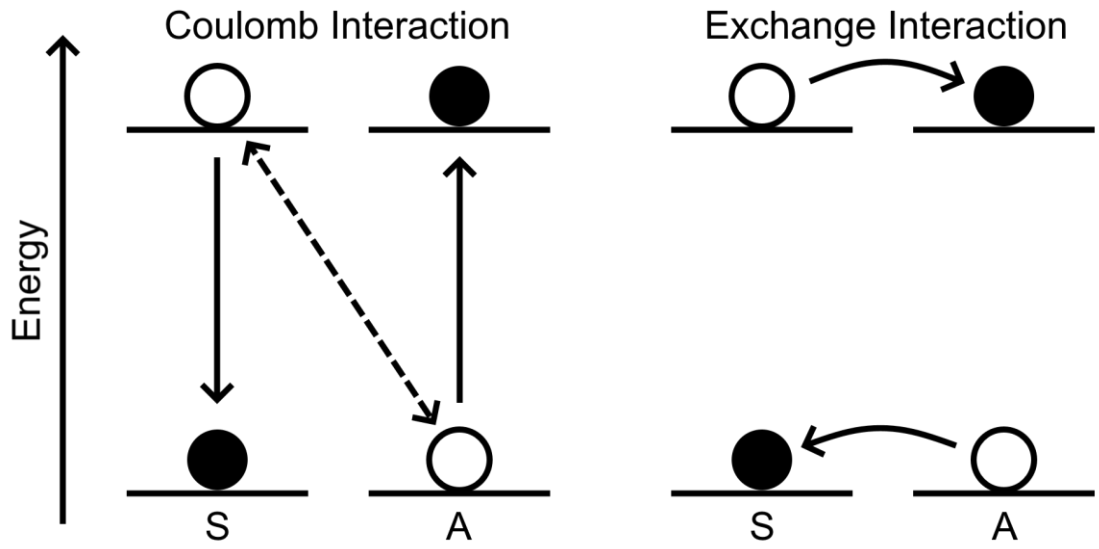

Figure 2.2: Energy level diagram showcasing coulomb and exchange interaction. The stapled arrows show the coulombic interaction between sensitizer (S) and absorber (A) ion.

2.1.2.1 Energy Transfer in Upconversion Systems

The above energy transfer mechanisms are used in upconversion systems, but to explain upconversion we need to look more specifically at how energy is transferred in these systems. There are four main energy transfer processes that are important for upconversion. Two of them relate to energy absorption, being ground-state absorption (GSA) and excited-state absorption (ESA). In addition, there is energy transfer upconversion (ETU) and cross-relaxation. An illustration of these is shown in Figure 2.3.

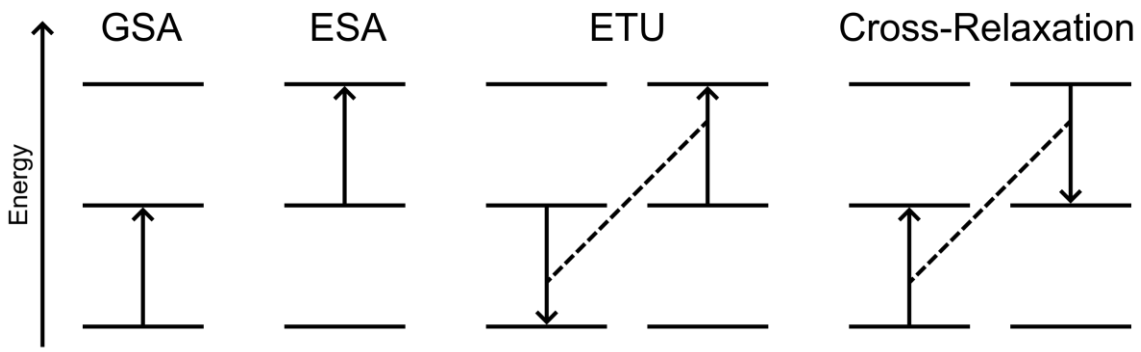

Figure 2.3: Energy diagram showing four energy transfer mechanisms central in upconversion. From left to right: ground-state absorption, excited-state absorption, energy transfer upconversion and cross-relaxation. Adapted from [39].

In GSA and ESA an incoming photon excites an electron from the ground state or an excited state, respectively, to a higher state. When a system has two ions in an excited state, ETU can take place. Here, one of the electrons relaxes to a lower energy-state while the other excites to a higher energy-state. Lastly, there is cross-relaxation. This is a subgroup of coulomb interaction, where only part of the energy is transferred. It functions as the reverse of ETU, as presented in the figure above. An electron at a lower energy-state is excited, while an electron at a higher energy-state de-excites. Since we do not excite an electron to a higher-than-original energy-state, cross-relaxation is often unwanted. However, it can also be useful. In this project, cross-relaxation is used for multiple of the energy transfers that move the absorbed energy to the activator ion.

The project uses energy-migration-mediated upconversion (EMU). This is similar to ETU, but the sensitizer and activator are separated by one or more types of ions. An energy level diagram showing EMU is given in Figure 2.4. The ions in the system are

divided into four parts: sensitizers, migrators, accumulators, and activators. The sensitizer's job is to absorb incoming photons. The migrator transports, or "migrates", the energy given from the sensitizer through the structure to the accumulator. Here, the energy is accumulated by absorbing each incoming energy-packet and being excited to constantly higher energies. This is hence the ion where the upconversion takes place. The accumulator transfers its energy to the activator ion, which then emits the resulting higher-energy photon. It should be noted that ions can inhabit more than one role, and depending on the system, the energy is accumulated before it is migrated.

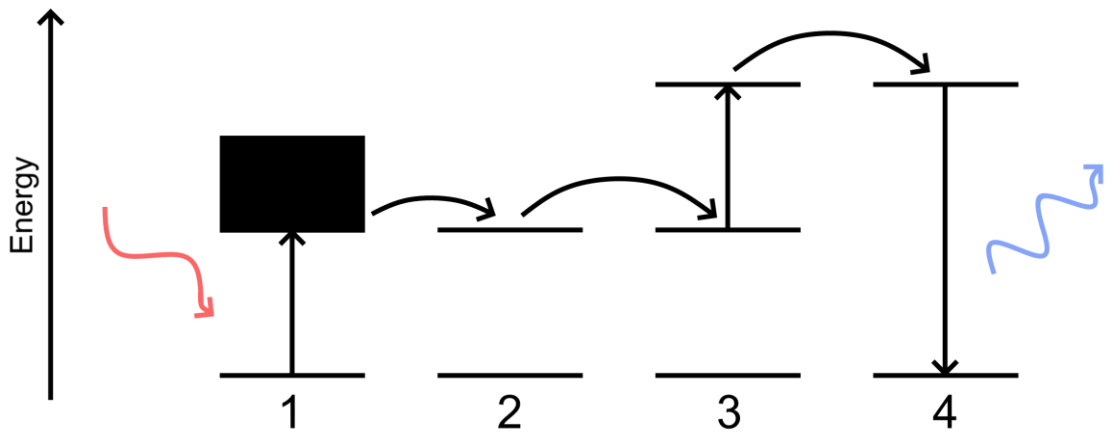

Figure 2.4: Schematic energy diagram showing energy migration-mediated upconversion where 1 is sensitizer, 2 is migrator, 3 is accumulator, and 4 is activator.

2.1.3 The Upconversion System

The upconversion system planned in this work is given in Figure 2.5 together with how we visualize the transfer of energy. The organic sensitizer is Qz, which will absorb the incoming light. As an organic dye, Qz has a wide energy band, meaning it can absorb broadband light for use in the upconversion process. The absorbed energy will be transferred to a Nd^{3+}-ion, which provides a better fit between the Yb^{3+}-matrix and Qz to contribute to a higher efficiency. Yb^{3+} is a migrator and will transfer the energy further on to Tm^{3+}, which is both accumulator and activator. Here, the energy will be gathered as the excited state is excited further up the ladder-like energy bands before finally emitting as a high-energy photon. The ions will be separated by a certain distance of YbF_3 to avoid loss mechanisms from occurring. An illustration of this is given in Figure 2.6.

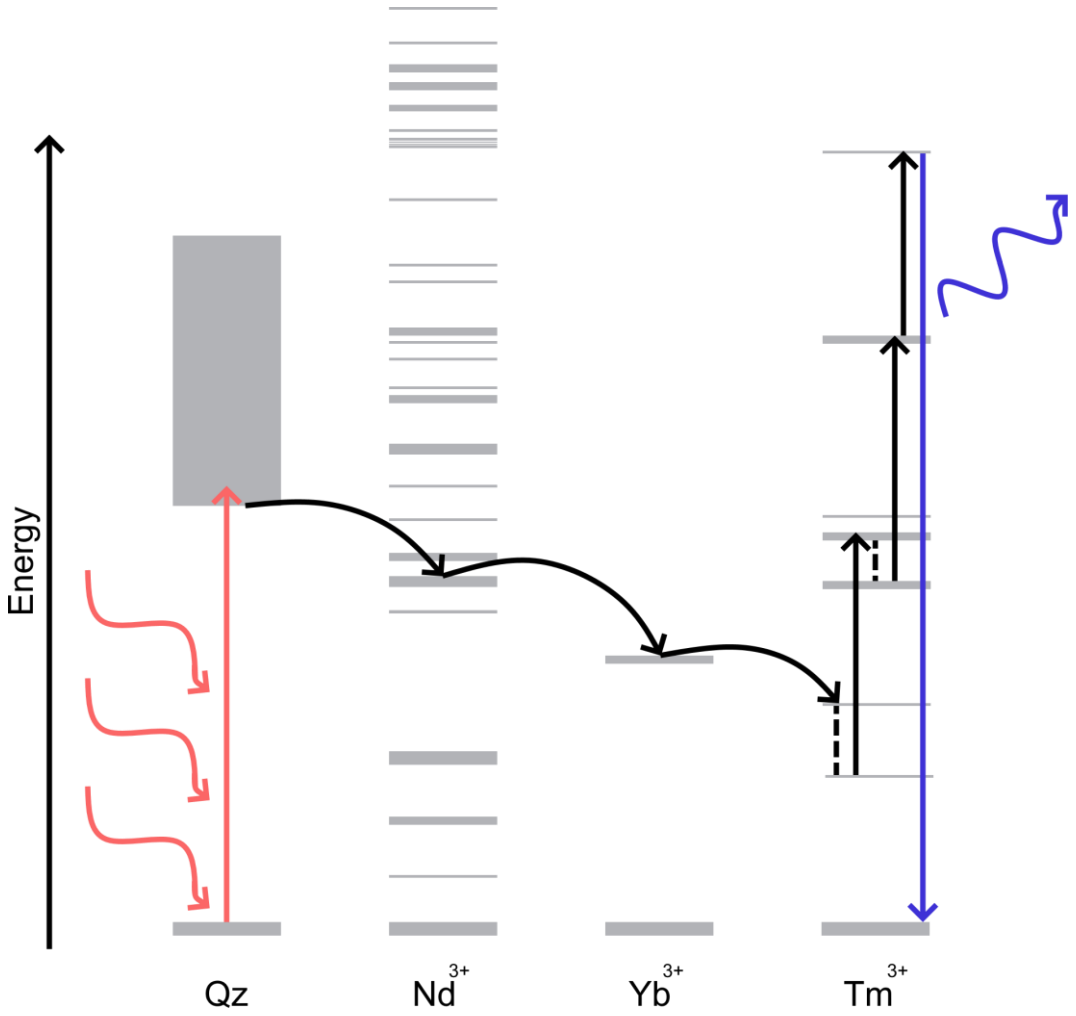

Figure 2.5: Schematic energy level diagram of the different compounds in our upconversion system. Incoming photons excite Qz. This energy is transferred to Nd^{3+}, then Yb^{3+}, before reaching Tm^{3+}. Here the energy accumulates up and finally emits a photon with higher energy than the incoming ones. Adapted from [12].

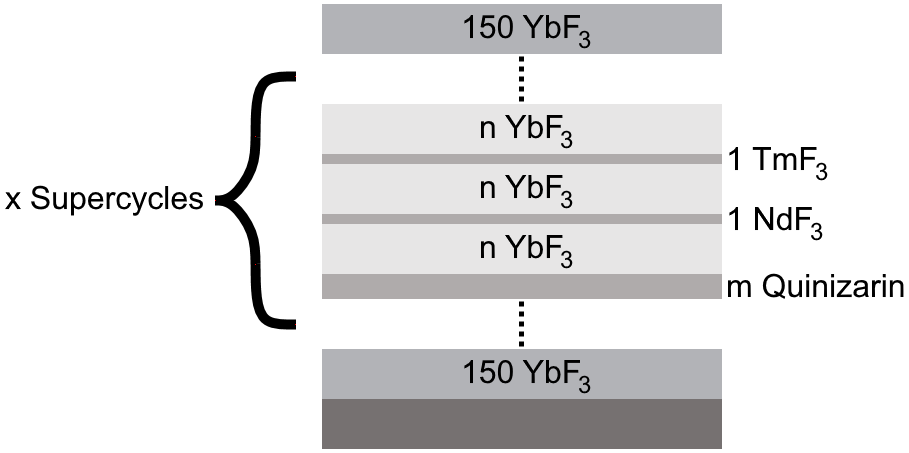

Figure 2.6: An illustration of our planned deposition layers for the system. 1, 150, n and m refer to number of deposition cycles. The system will consist of x supercycles deposited within a matrix of YbF3. Adapted from [12].

2.2 Atomic Layer Deposition (ALD)

Atomic layer deposition is a thin film synthesis technique using reactions between the gas phase and an active surface to grow compounds. In contrast to Chemical Vapor Deposition (CVD) where multiple precursors can be introduced simultaneously and gas phase decomposition can lead to growth on the substrate, ALD introduces its precursors in a sequential manner. Each precursor is separated in time and space using purging steps with inert gas to avoid gas phase reactions. In addition, each reaction between surface and precursor is self-limiting, meaning that the precursor does not react with its own adsorbed layer, hence it cannot grow more than a monolayer.

ALD is performed at elevated temperatures in a vacuum system. The precursors can be either solid, liquid or gas, but they all need to be volatile under the ALD conditions. During this project we have mostly used solid type precursors in ALD, where the precursors are sublimed by heating under vacuum. The precursor is carried into the reaction chamber by an inert gas. Figure 2.7 shows the different steps in a single ALD cycle, using H_2O and TMA as precursors, with N_2 as the inert purging gas.

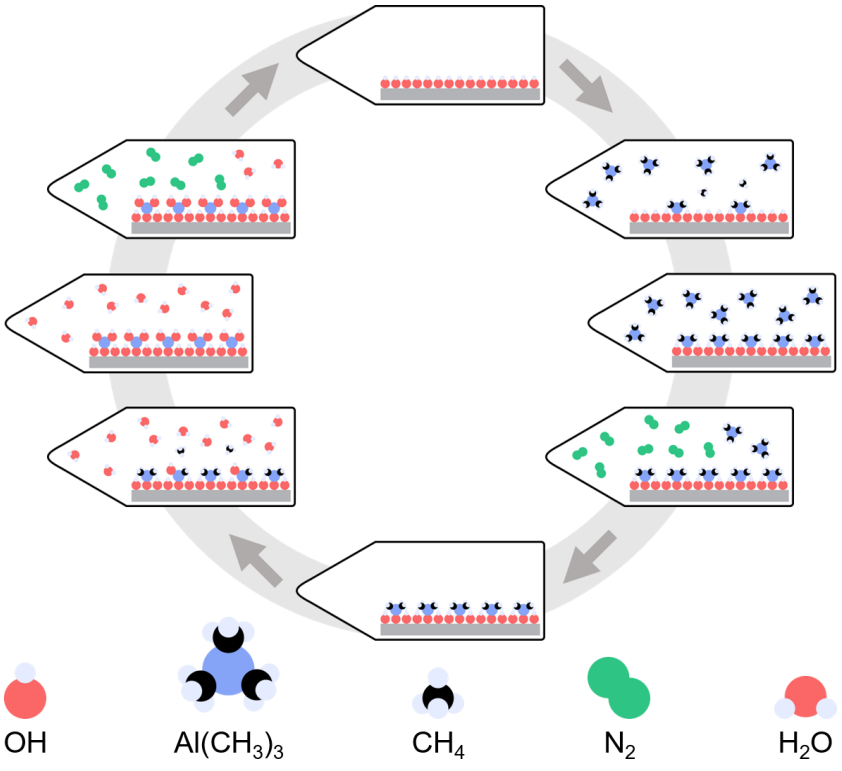

Figure 2.7: Illustration showing the cyclic character of ALD. Here highlighted using growth of Al_2O_3. Adapted from [55]

2.3 Characterization

This section presents the fundamentals of various characterization techniques used in the project, from optical methods to x-ray based techniques and more.

2.3.1 Optical Characterization

2.3.1.1 Spectroscopic Ellipsometry (SE)

Spectroscopic Ellipsometry is an optical non-destructive spectroscopy technique sued to characterize thickness, roughness, and refractive index (*n*) of transparent and absorbing thin films. The technique can determine the optical properties of films with thickness between 0.1 nm - 200 µm by using linearly polarized light. The beam of light is converted to elliptically polarized light when scattered off the sample, and a detector equipped with a polarization filter measures the beam's change in phase and polarization. Figure 2.8 shows a sketch of the technique's basic principles.

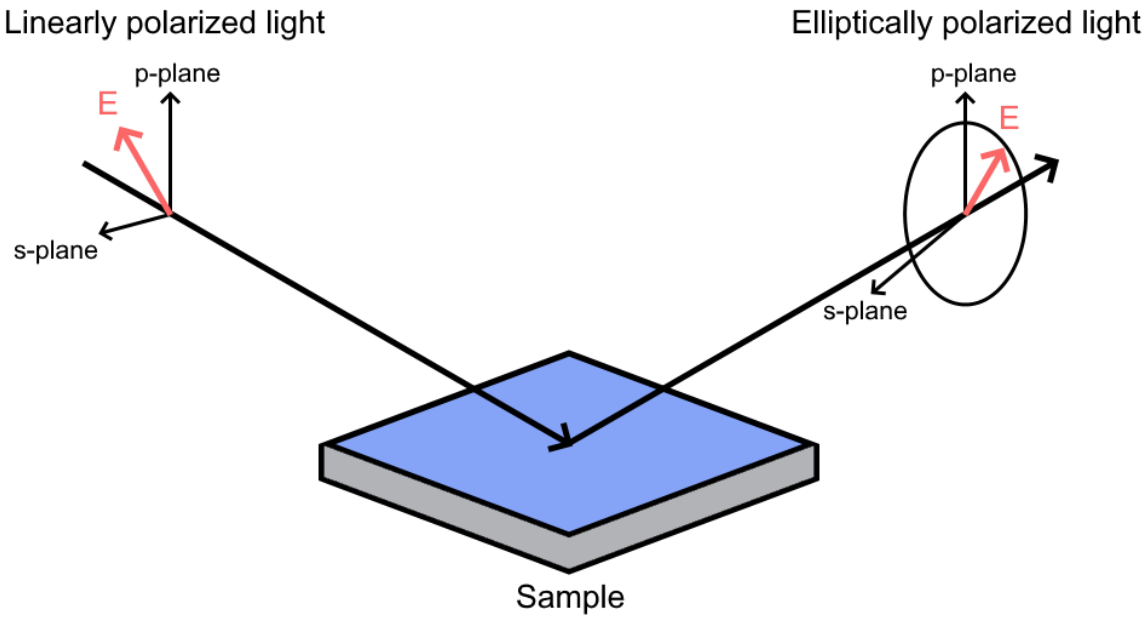

Figure 2.8: Sketch showing the basic principle of spectroscopic ellipsometry. Incoming linearly polarized light becomes elliptically polarized upon scattering from the sample. Adapted from [56].

Upon fitting the data to an optical model, the film's characteristics can be obtained. The Cauchy model is one such model that can be used on non-absorbing films. Other models must be used to model absorbing films, such as oscillator theory. Here, the dielectric polarization caused by incoming light is modelled using various oscillators, for example Gaussian, Harmonic and Lorentz oscillators [57].

2.3.1.2 Fourier-Transform Infrared Spectroscopy (FTIR)

Fourier – Transform Infrared Spectroscopy (FTIR) is a spectroscopy technique that utilizes infrared light to excite vibrations in a sample. FTIR is only sensitive to vibrations that induce a change in dipole moment. An overview of such vibrations can be used to determine how the bonds are structured in a thin film sample. Where a dispersive technique gathers signals for different wave numbers (frequencies) separately, FTIR uses a Fourier transform method to obtain the signals for these wave numbers at the same time [58].

2.3.1.3 Ultraviolet-Visible Spectroscopy (UV-Vis)

UV-Vis is an optical characterization technique that uses broadband ultraviolet, visible or near infrared light. This light passes through or onto a sample, where some of the photons will be absorbed by the material and induce electronic transitions. By measuring the remaining light, one can gain information about these transitions.

UV-Vis is generally used to measure transmitted light (T) and reflected light (R) and is combined to determine the absorbed light (A) of the material investigated using Equation (2.2).

$$A=1-T-R \tag{2.2}$$

In contrast to FTIR, UV-Vis is a dispersive technique, where, using a prism or grating that disperses light, the signal is detected by scanning through wavelengths sequentially.

When performing a measurement, it is normal to measure a reference to determine a baseline for the relative response from the sample. For transmittance, the reference is air, while for reflectance a $BaSO_4$ standard is frequently used due to the near 100% reflectance.

2.3.1.4 Photoluminescence Spectroscopy (PL)

Photoluminescence spectroscopy (PL) is an optical characterization technique. Like for UV-Vis, PL uses a light source, typically of UV or visible wavelength, to illuminate a sample. The light that is absorbed can lead to electron excitations that again can lead to photon emission from the sample (photoluminescence) once the electrons de-

excite again. Due to loss mechanisms such as phonon vibration, the emitted wavelengths are longer than the incoming ones, known as a Stokes shift. Where UV-Vis often uses broadband light and observes the remaining light to gain an absorption spectrum, PL commonly uses LEDs or other monochromatic light sources. Rather than recording the reflected light, it records light emitted from the sample to report the photoluminescent activity. Since PL gives an emission spectrum, we often want to omit the light from the excitation source. This is frequently performed by using various optical filters, such as a long-pass filter which only transmits longer wavelengths above (lower energy) a certain value. A long-pass filter for 400 nm, for example, would block all light with a wavelength shorter than 400 nm.

PL uses a light source, prism or grating to disperse light, and a detector. The light source is either a photon diode, xenon lamp or laser. A simplified schematic of a PL setup is given in Figure 2.9.

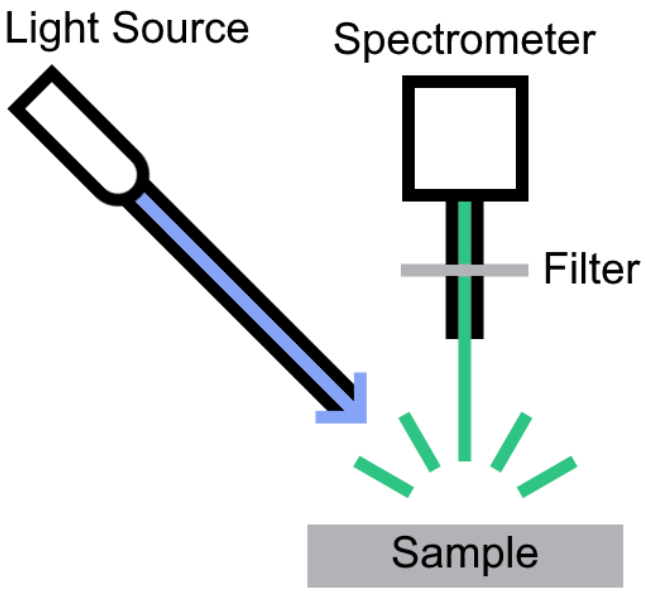

Figure 2.9: A schematic illustration showing PL spectroscopy. A light source emits light on a sample, which then emits luminescent light that is caught and passed through a filter before reaching a spectrometer.

2.3.1.5 Cathodoluminescence Spectroscopy (CL)

CL uses a high energy electron beam to excite a sample. The electrons scatter inelastically, causing a plethora of energy transitions in the sample. These transitions can lead to photon emissions giving rise to a wide emission spectrum. One can assume that doing CL will excite all possible transitions, allowing to detect impurities and different compounds from analyzing the spectra. The high energy from CL also allows to see transitions that PL would not be able to excite.

2.3.2 X-Ray Characterization

X-rays are commonly used in characterization of materials. They are normally generated by excited states from deaccelerating high energy electrons, so-called bremsstrahlung, or “braking radiation”. This project uses X-Ray Diffraction (XRD) and X-Ray Reflectivity (XRR) to analyze thin films.

2.3.2.1 X-Ray Diffraction (XRD)

XRD is a technique where scattering of X-rays is used to examine the crystal structure, or lack of such, in a sample. As X-rays illuminate the sample, they scatter when interacting with atoms. For amorphous samples, coherent scattering is not possible, while the repetitive pattern of rows and columns in crystalline samples gives rise to constructive interference and distinct peaks in a diffraction pattern. This is best visualized using Bragg’s Law, which shows how these angles are related to the distance between columns of atoms. An X-ray incoming at an angle θ, will scatter out with the same angle θ.

A schematic showing diffraction is given in Figure 2.10.

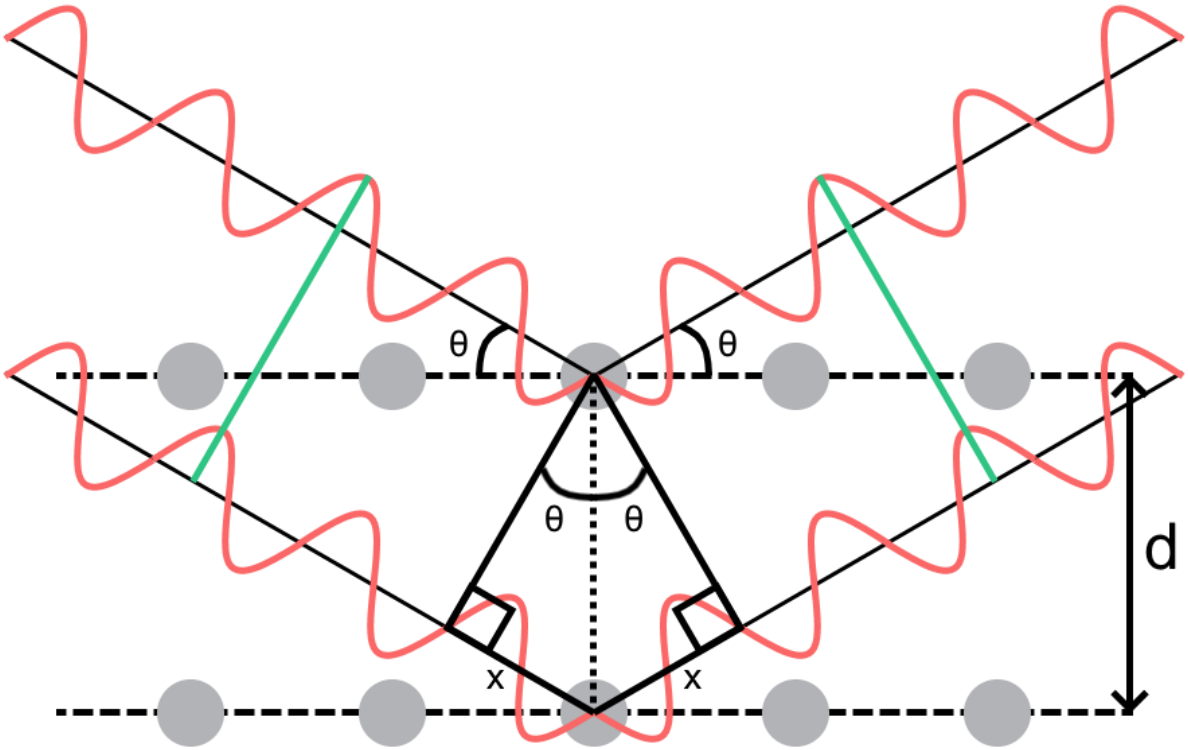

Figure 2.10: A schematic showing the Bragg condition.

Using the figure above, one can see that the X-ray interacting with the lower column travels an extra path length, denoted by the two *x*'s. This path length related to the incoming angle, θ, and the lattice distance, *d*, through trigonometry, giving rise to the definition of Bragg's Law [58] as given in Equation (2.3) with multiplicity *n* and wavelength λ.

$$n\lambda = 2d\sin\theta \tag{2.3}$$

2.3.2.2 X-Ray Reflectivity (XRR)

XRR is a technique where X-rays reflect from a thin film. The X-rays reflect on the top and bottom of a sample's interfaces causing interference. This leads to the formation of oscillations known as Kiessig fringes [59]. The fringes allow us to gain insight into a thin film as they change depending on the density, thickness and roughness of the film. Increased density leads to increased incident angle before drop-off, increased thickness leads to higher oscillation frequency, and increased roughness increases the dampening of the oscillations. An illustration of a typical XRR spectrum is given in Figure 2.11.

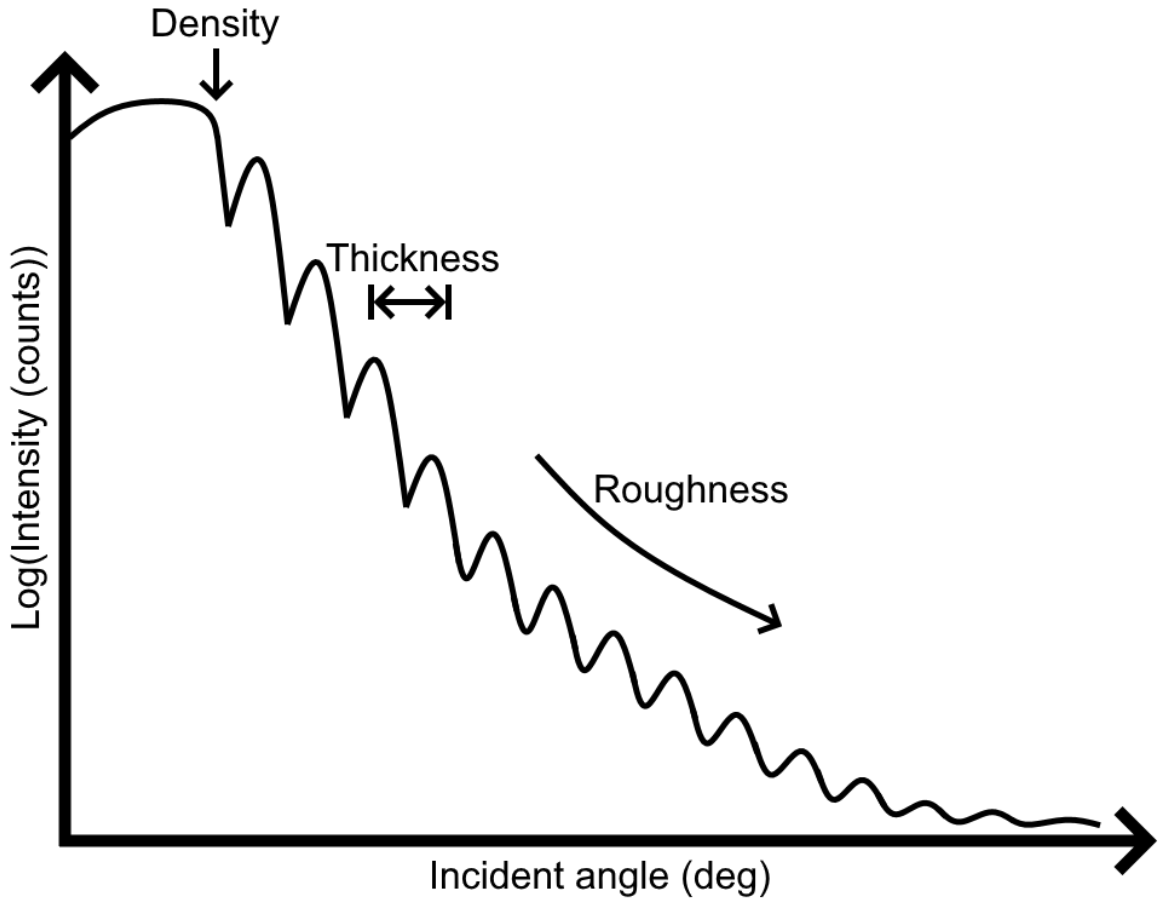

Figure 2.11: Illustration of an XRR spectrum. The annotations show the features that are used to measure density, thickness and roughness.

2.3.3 Atomic Force Microscopy (AFM)

AFM is a microscopy technique used to probe and map surfaces on the micro- and nanoscale. It is a type of Scanning Probe Microscopy (SPM), and utilizes a sharpened tip, that scans across the surface. The AFM instrument detects near-field forces

between the tip and the sample. There are several types of near-field forces, such as, van der Waals and electrostatic forces. A key element of the AFM is how the cantilever functions as a microscopic force sensor. The tip is located at the end of the cantilever, and the detection of near-field forces is measured by deflection of a laser light illuminating the cantilever [58]. A schematic illustration of the AFM principle is given in Figure 2.12.

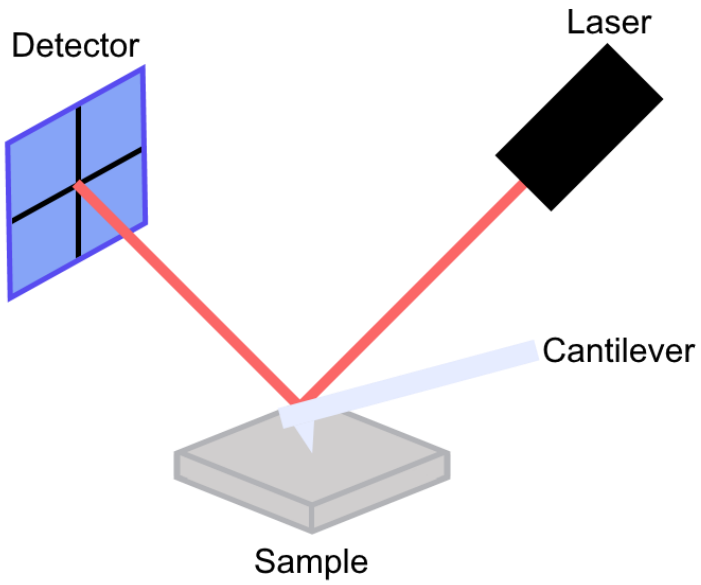

Figure 2.12: An illustration of how an AFM signal is formed.

AFM can provide insight into the topography of a surface by creating an image of the raster scan. The surface roughness and its shape can support ideas on whether the surface is amorphous or crystalline. One central parameter is the surface roughness. We utilize the Root Mean Square (RMS) roughness, S_q, which is defined in [60] and given in Equation (2.4) .

$$S_q = \frac{1}{N}\sum_{i=1}^{1}(z_i - \bar{z})^2 \qquad (2.4)$$

Where N denotes the number of height values of the measurement, z_n denotes the i-th height value, and $\bar{z}$ denotes the mean height in the measurement.

2.3.4 Quartz Crystal Microbalance (QCM)

QCM is an in-situ technique used for characterizing growth mechanisms of thin films. It relies on the physics of a piezoelectric quartz crystal and its resonant frequency. A piezoelectric material vibrates with a natural frequency that can be measured. The resonant frequency of this vibration changes with the total mass of the crystal, enabling us to detect any deposition that occurs directly on the crystal. The Sauerbrey's equation [61], provided in Equation (2.5) below, shows the relation between change in mass and frequency.

$$\Delta f = -\frac{2f_0^2 \Delta m}{A\sqrt{\mu\rho}} \tag{2.5}$$

Δf is change in resonant frequency, f_0 is the resonant frequency for the crystal before coating, Δm is mass change, A is crystal area, μ is shear modulus and ρ the quartz crystal density.

3 Experimental

This chapter contains traceable information about the precursors and experimental methods that were utilized. Firstly, the preparation of ethanol solutions of Qz and ions will be explained. Then, synthesis of the thin films and the setup for this, before diving into the characterization of the structures and their optical properties.

3.1 Ethanol solutions

An overview of the compounds used for ethanol solutions is given in Table 3.1. The compounds were weighed out using a Mettler AT200 laboratory weight (d=0.01 mg) before being dissolved in ethanol. Upon use, small amounts of these solutions were transferred to glass containers using Finnpipette pipettes.

Table 3.1: List of compounds used in ethanol solutions, with purity, CAS number LOT number and supplier.

Compound	CAS number	Purity	Product Number	LOT Number	Supplier
Ethanol	64-17-5	≥99.8%	20821.330	Multiple bottles	VWR Chemicals
$AlCl_3$	7446-70-0	97%	3373-100		KEBOLab
$YCl_3 \cdot 6H_2O$	10025-94-2	99.99%	464317	MKBQ5485V	Sigma Aldrich
Hthd	1118-71-4	≥98%	155756	BCBJ5218V	Sigma Aldritch
$Yb(thd)_3$	15492-52-1	99%	70-0100	27296300	Strem Chemicals
$Y(thd)_3$	15632-39-0	>98%	39-1000	34690100	Strem Chemicals
$Nd(thd)_3$	15492-47-4	99%	60-8750	A7762079	Strem Chemicals
$Al(acac)_3$	13963-57-0	99.999%	674753	0000053081	Sigma Aldrich
Qz	81-64-1	96%	Q906	BCCB1275	Sigma Aldrich

3.2 Deposition of Fluoride Thin Films

3.2.1 Atomic Layer Deposition

Thin film depositions were performed using an ALD reactor constructed at the Department of Chemistry UiO. The reactor is based on the design of an ASM Microchemistry F-120 reactor. A schematic of the reactor and its eight temperatures zones is given in Figure 3.1.

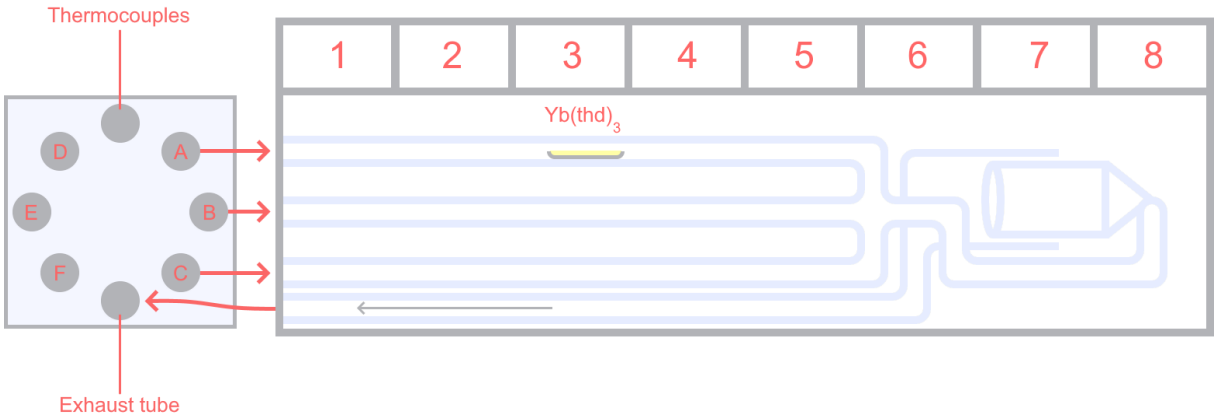

Figure 3.1: Schematic showing the ALD reactor with temperature zones, exhaust tube, reaction chamber and precursor tubes containing Yb(thd)$_3$. Adapted from [56].

Each zone is heated by its own heating coil and is separated by a metal sheet to provide a certain amount of insulation between them. The temperature zones from 1 to 5 are used for subliming the precursors. Usually, only zone 1 to 4 is used for this, but Nd(thd)$_3$ was moved to zone 5 due to many precursors requiring different temperatures. The reaction chamber is in zone 6 and 7, and zone 8 is used as a control zone.

To provide vacuum, a set of two vacuum pumps are utilized, all shared by the four reactors of the research group. The smaller one, Pfeiffer Vacuum Duo 10, is used to evacuate the reactor from ambient pressure to ca. 10 mBar, while the larger pump, Pfeiffer Vacuum Okta 500 M, brings the pressure further down and maintains it at ca. 5 mBar during deposition. An N2-Sirocco-5 was used as an external N_2-source, with an N_2 5.0, Nippon Gasses gas bottle as backup.

3.2.2 Precursors

An overview of the precursors used for ALD deposition is given in Table 3.2, in addition to $Nd(thd)_3$, $Yb(thd)_3$, $Y(thd)_3$ and Qz from Table 3.1. To confirm that the reactor was working optimally we also deposited a set of standard thin films of Al_2O_3 using $Al(CH_3)_3$ and Type II H_2O.

Table 3.2: List of precursors used in ALD deposition, with purity, CAS number LOT number and supplier.

Precursor	CAS number	Purity	Product number	LOT number	Supplier
NH_4F	12125-01-8	≥99.99%	338869-100G	S34814	Sigma-Aldrich
$Tm(thd)_3$	15631-58-0	98%	69-7000	26450800	Strem Chemicals

3.2.3 Substrates

The project used multiple substrates, each with their own purpose. They are listed in Table 3.3, and Figure 3.2 shows their standard positions in the reaction chamber. The glass plates were washed in ethanol and blow dried. Silicon, fused silica and sapphire substrates were cleaned with dry cleaning wipes and blow dried to remove dust. The electropolished steel substrates were covered in protective tape on arrival, and these surfaces are considered clean upon removing the tape. The substrates were given ID by scratching patterns on their backside. The silica, sapphire and glass substrates were included in depositions where UV-Vis measurements were intended. Electropolished steel was included for depositions where FTIR was intended. The silicon substrates were included in all depositions, generally as 1x1 cm^2 substrates placed on either end of the 5.1 x 7.6 cm^2 glass plate, and at times longer (1 x 5 cm^2 - 1 x 7 cm^2) strips were used along the flow direction to observe gradients along the flow, and from side to side by placing one on each side of the glass plate.

Table 3.3: Substrates used for ALD.

Type of substrate	Information	Supplier
Silicon	Single crystal Si(100)	University Wafer
Fused Silica (SiO_2)		University Wafer
Electropolished Steel		Rimex Metals Group
Glass (SiO_2)	Microscope coverslips	Chemi-teknik AS
Sapphire	Single crystal Al_2O_3(111)	University Wafer

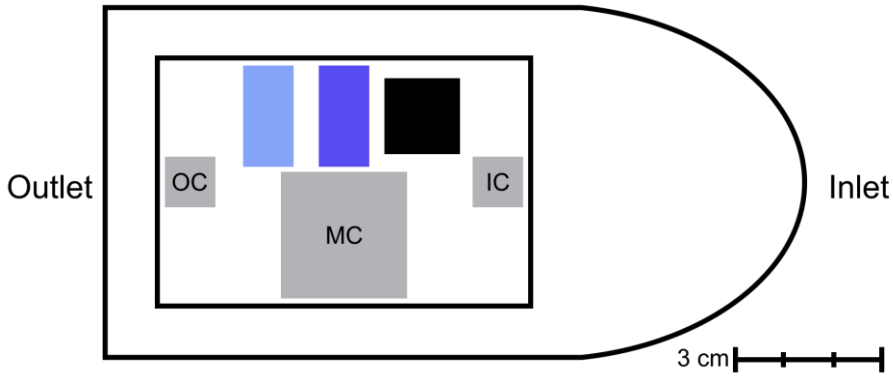

Figure 3.2: Illustration of the reaction chamber seen from above. The substrates were placed on a glass plate. From left to right: grey substrates are silicon, light blue is fused silica, blue is sapphire, and black is electropolished steel. The annotations: OC, MC, and IC denote the standard naming convention for each location on the glass place.

3.2.4 Parameters

All depositions occurred at pressures between 1.7 and 2.9 Torr. Standard depositions were performed at 175 °C for 1000 cycles (250 cycles for Qz-films) with the temperature zones heated as shown in Table 3.4. Most all depositions used nitrogen flows of a total of 500 sccm to guide the precursor flows. The sublimation temperatures for each precursor were adopted from [22], with the sublimation temperature of $Y(thd)_3$ being from [12] and Qz from [13]. The temperatures used for each precursor can be found in Table 3.5.

Table 3.4: Temperature for each zone in the ALD reactor.

Zone	**1**	**2**	**3**	**4**	**5**	**6**	**7**	**8**
Temperature [°C]	80	100	125	130	155	175	175	175

Table 3.5: Overview of precursors and their temperatures during deposition.

Precursor	**NH_4F**	**$Nd(thd)_3$**	**$Tm(thd)_3$**	**$Yb(thd)_3$**	**$Y(thd)_3$**	**Qz**
Temperature [°C]	80	155	125	125	130	125

3.3 Characterization

This chapter provides an overview of how the various characterization techniques were performed, and equipment used.

3.3.1 Spectroscopic Ellipsometry

To determine the thickness, roughness, and refractive indexes of the thin films, we used a J.A. Woollam alpha-SE ellipsometer. The measurements were performed at an incident angle of 70 ° and for wavelengths between 380 and 900 nm. The refractive index was noted at 632.8 nm for all samples. Complete EASE version 4.92 from J.A. Woollam was used to model the optical properties. The Cauchy function was used as standard approach for the transparent films. For the absorbing films with Qz, the properties were modelled using wavelengths between 700 and 900 nm using the same model. This is a range of wavelengths were Qz is considered transparent, and hence allowing for use of the Cauchy function. For a selection of Qz-containing films, a custom model using Gaussian and Lorentz-oscillators was created and used in conjunction with the standard Cauchy model, to ensure the results were accurate. This because a narrower selection of wavelengths decreases accuracy and increases uncertainties. However, as the Cauchy model and custom model estimated similar results, the Cauchy model proved accurate enough for our needs. For estimating errors, investigations of fit parameter uniqueness for thickness found that an error of ±0.1 nm was reasonable.

3.3.2 Fourier-Transform Infrared Spectrometry

A Bruker VERTEX 70 FTIR spectrometer was used in reflection mode to acquire the FTIR spectra. All measurements were performed using electropolished steel substrates, using a clean substrate for measuring the background. The data were further treated using the software OPUS version 7.0 from Bruker.

3.3.3 Photoluminescence Spectroscopy

To perform PL spectroscopy, we used an Ocean Insight FLAME miniature spectrometer for the UV-Vis range (200 – 900 nm) and an Ocean Insight NIRQuest Near-Infrared spectrometer for the IR range (900 – 1700 nm). The setup consisted of

multiple Ocean Insight UV and visible LEDs as light sources often combined with long-pass filters from Newport to remove the LED light from the measured signal. We also used Ocean Insight's solarization and extreme solarization resistant fibers. The setup was used to measure fluorescence as well as UV-Vis transmission and reflectivity, though we mainly used the dedicated UV-Vis setup mentioned in 3.3.4 for this purpose. All data were recorded using the software OceanView 2.0 from Ocean Insight, before further evaluation using Python 3.10.2 [62].

3.3.4 UV-VIS Spectroscopy

UV-Vis measurements were performed with a Shimadzu UV-3600 Photospectrometer operating between 200 and 1700 nm. For the UV area of the spectrum a D_2 lamp was used, while a halogen lamp was used for visible and NIR wavelengths. There were two detectors used, an InGaAs photodiode for 900 – 1700 nm, and a photomultiplier tube for 180 – 900 nm. To record data, we used the software UVProbe version 2.43 from Shimadzu.

3.3.5 Cathodoluminescence

Cathodoluminescence was performed on a JEOL JSM-IT300LV Scanning Electron Microscope at UiO MiNaLab. The microscope uses a thermionic-emission LaB_6 electron gun and is equipped with a Delmic SPARC Cathodoluminescence system detector. The measurements were performed by Jon Borgersen at MiNaLab, and data obtained was evaluated using Python [62].

3.3.6 X-Ray Diffraction

For the XRD measurements we used a Bruker AZS D8 Discover in Bragg-Brentano mode, performing θ-2θ scans. The instruments is equipped with a Ge(111) Johanssen monochromator, a Lynxeye detector and a 90 position sample changer. The instrument uses Cu $K\alpha_1$ radiation to scan samples. We performed θ-2θ scans from 2° to 60° and varied the time scale from 1 to 10 depending on required resolution. the data was analyzed in DIFFRAC.EVA Version 6.0.0.7 from Bruker.

3.3.7 X-Ray Reflectivity

A Panalytical Empyrean diffractometer with Cu radiation was used to perform the XRR measurements. It has both a PixCel 2×2 and scintillation counter detector, the latter one being used to perform XRR. The data was evaluated using the software X'Pert Reflectivity 1.3a from Panalytical.

3.3.8 Atomic Force Microscopy

To perform AFM, we used a Park Systems XE-70 atomic force microscope. The instrument was placed inside an anechoic box and on top of an anti-vibration stage to reduce the disturbance caused by external vibrations during the measurements. All measurements were performed on samples on silicon substrates in non-contact mode with a non-contact high-resolution tip from Park Systems and a scan rate of 0.5 Hz. To analyze data, we used the software Gwyddion version 2.60 [63].

3.3.9 Quartz Crystal Microbalance (QCM)

The QCM setup used to study growth in-situ was made by Ola Nilsen at the Department of Chemistry. Two α-quartz crystals of 6 MHz with gold contacts from Inficon were separated by 5 cm on a holder in a customized reaction chamber. The signal was recorded by an SQM-160 Inficon system and logged using a homemade Arduino-chipset. The data obtained was evaluated using a Python program developed by Ola Nilsen.

4 Results

This section presents results obtained from the experiments performed and is divided into four parts. The first part investigates the eligibility of Qz as a sensitizer. Then, the structural and optical properties of Ln_2Qz_3 films will be presented, before presenting results from LnF_3 films. Lastly, results obtained from investigating Qz-doped LnF_3 films will be shown.

4.1 Eligibility of Qz

The project builds on the idea that Qz can work as a sensitizer in a solid structure. This is not certain, but hard to disprove. A sensitizer is a good absorber that also can transfer the absorbed energy to other parts of the system. We know that luminescence can change when going from liquid to solid and vice versa. Still, investigation of solutions will give valuable insight into the interaction between Qz and the cations in our system. Preliminary investigations were therefore performed by creating liquid solutions where the optical activity could be characterized. Al was included as Al_2Qz_3 has been recently investigated [13].

4.1.1 Ethanol solutions

To investigate the interaction between Qz and the various cations, ethanol solutions of these cations were prepared. Each solution was 5 mL and contained 10^{-4} M Qz and 10^{-3} M of the cation compound, with a sample of pure ethanol included as a reference. The compounds investigated were $AlCl_3$, YCl_3, $Nd(thd)_3$, $Y(thd)_3{\cdot}H_2O$, $Yb(thd)_3$ and $Al(acac)_3$.

4.1.1.1 PL of solutions

Each solution was visually inspected under UV and visible light. Pictures of the solutions are given in Figure 4.1.

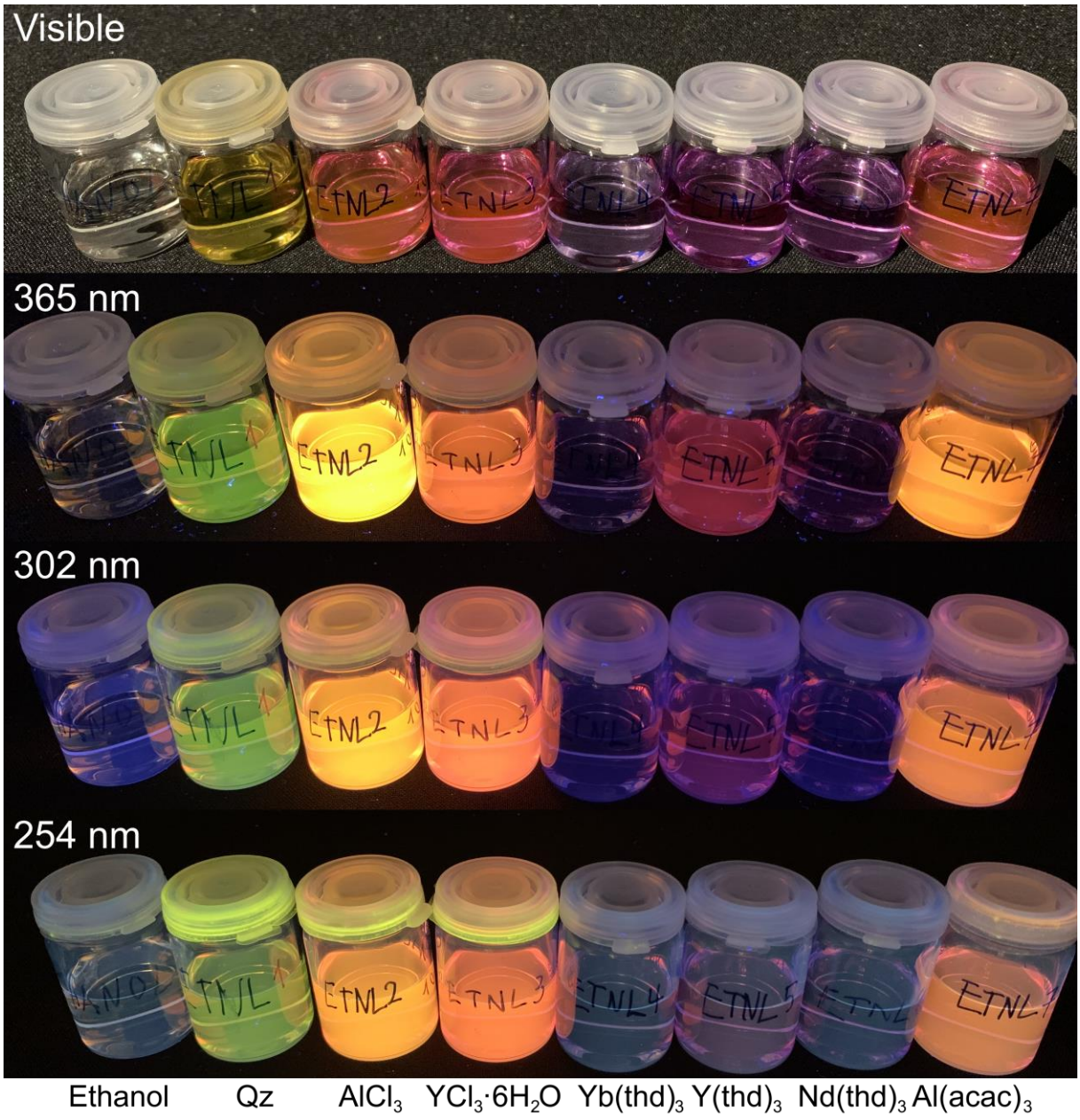

Figure 4.1: Pictures of ethanol solutions taken under visible light (a) and UV (b-d). b) 365 nm c) 302 nm and d) 254 nm. All but the left-most sample contain Qz.

To quantify the luminescence more accurately, PL measurements were performed on each sample using a 365 nm excitation source with a 435 nm long-pass filter. The integration time was 500 ms with results being averaged over 10 measurements. The PL spectra are given in Figure 4.2.

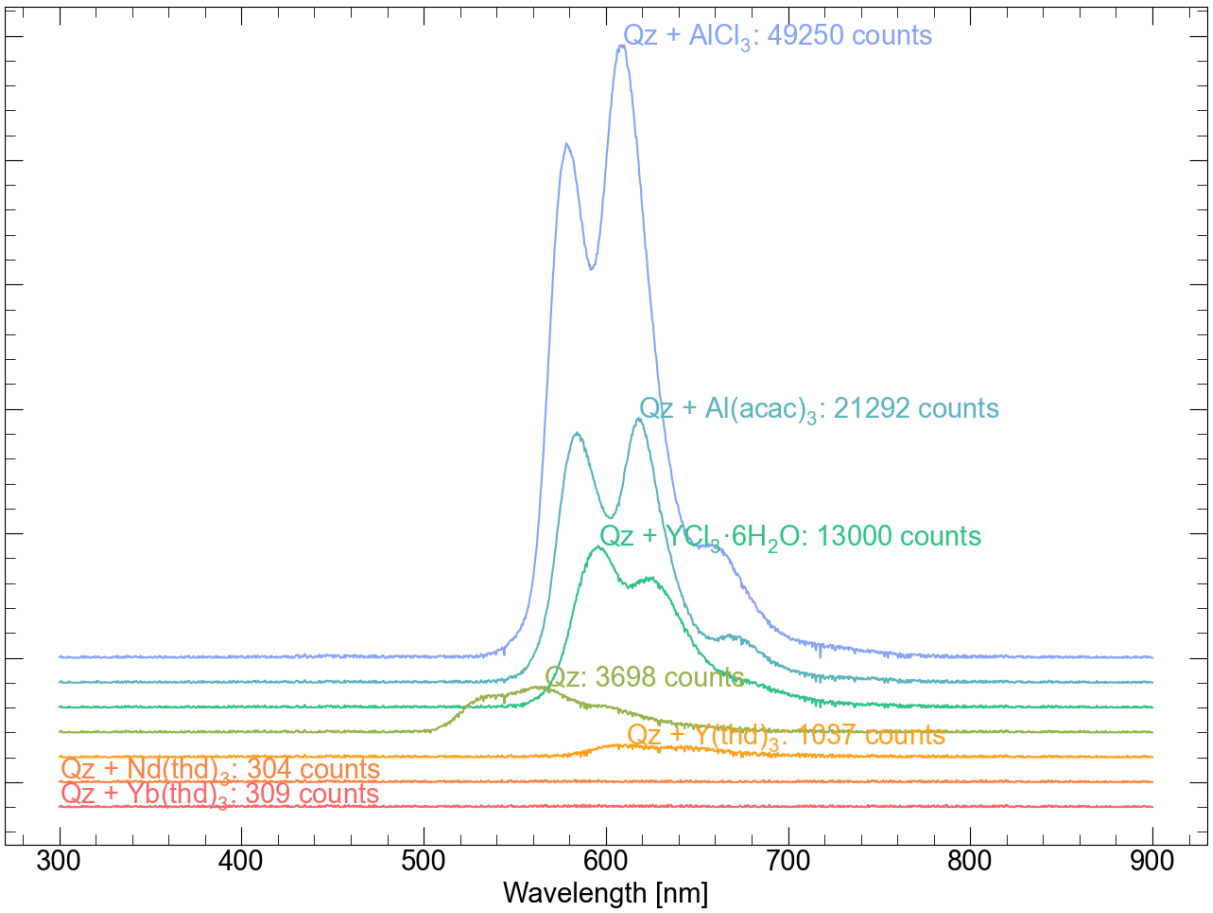

Figure 4.2: PL spectra of different ethanol solutions using a 365 nm excitation source with a 435nm long-pass filter. The annotated value shows the maximum value of each measurement.

The visual inspection indicates that the Cl-solutions luminesce quite well, whereas the thd-solutions do not show any noticeable activity, though $Y(thd)_3 \cdot 6H_2O$ does luminesce weakly. This is confirmed through the PL spectra. The $Al(acac)_3$-solution is weaker in intensity than the $AlCl_3$-solution, yet still much more active than the thd-solutions, even more so than YCl_3. Nd^{3+} and Yb^{3+} luminesce in the NIR region, but no activity was found through PL with an NIR detector. The decreased activity from thd-solutions made us wonder if the large thd-molecule was quenching the luminescence, either through steric hinderance or by absorbing the energy from Qz and decaying non-radiatively.

4.1.1.2 Ethanol solutions with Hthd

To gain a better understanding of thd's effect on the luminescence, new Qz- and $Y(thd)_3 \cdot 6H_2O$-samples were prepared. To these we added Hthd to a concentration of 10^{-3} M. These solutions were inspected visually under visible and UV light. Pictures of these solutions, together with ones not containing Hthd, are given in Figure 4.3.

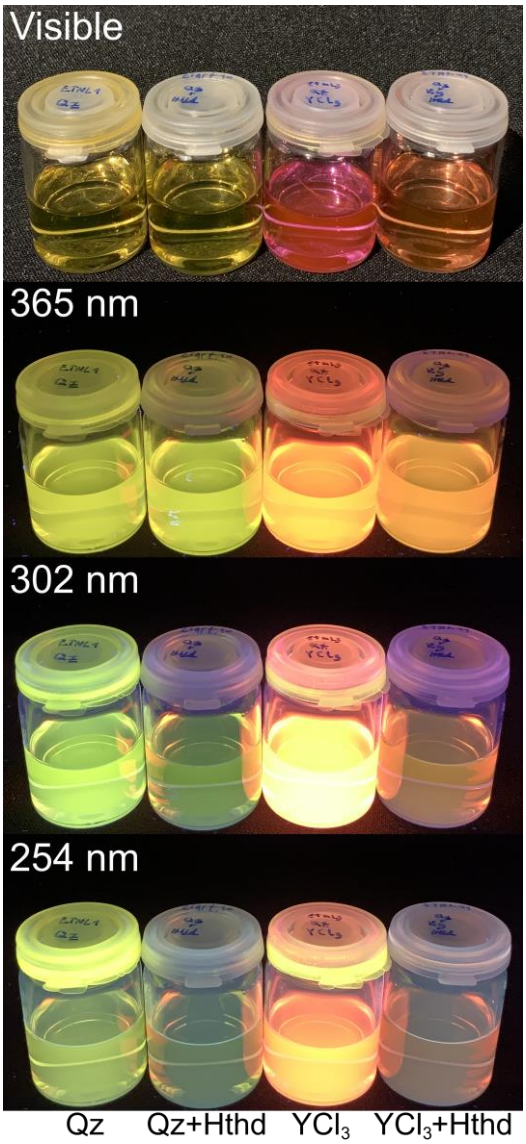

Figure 4.3: Pictures of ethanol solutions comparing intensity with and without Hthd present. YCl_3 is $YCl_3 \cdot 6H_2O$.

The luminescence under UV is vastly different in intensity, with the solutions containing Hthd being much weaker under the shorter wavelengths. This indicates that thd in fact is quenching the luminescence of the solution somehow, and likely shift the luminescence as there is a color difference between $Y(thd)_3 \cdot 6H_2O$ with and without Hthd.

Overall, we observe that our Y^{3+}-solutions do luminesce. This indicates that Y_2Qz_3 has the possibility to work as a sensitizer in our thin film system, provided that it also luminesces when condensed as a solid film.

4.1.1.3 Drying of solutions

Some amounts of $AlCl_3$ and Qz were dissolved in ethanol and allowed to dry. The same was performed for $YCl_3 \cdot 6H_2O$ and Qz. After drying, the remaining powders were scraped together and investigated under a UV lamp, and no luminescence was observed.

4.2 Deposition of Ln_2Qz_3

With preliminary investigations of Qz luminescence complete, the work on depositing thin films could begin. When creating an upconversion system, controlling the distance between ions is crucial to maximize efficiency. Sufficient knowledge about the properties of Ln_2Qz_3 thin films is therefore important. This subsection investigates the properties of Y_2Qz_3 and Y_2Qz_3 films using QCM, XRD and XRR for characterization of the growth and its structure. FTIR, UV-Vis and PL was performed to understand the optical properties of the films. SE was used for characterization both of growth and structure through thickness and roughness, while also being used to measure index of refraction. The films were as a standard deposited at 175 °C using 250 cycles. The standard cycle for Y_2Qz_3 was 2 s / 1 s / 3 s / 1 s for $Y(thd)_3$ / purge / Qz / purge, while Yb_2Qz_3 had 3 s for the $Yb(thd)_3$ pulse.

4.2.1 QCM of Y_2Qz_3 from $Y(thd)_3$ and Qz

Y_2Qz_3 was investigated using QCM to characterize the growth and optimize pulse and purge times. The QCM responses for pulse and purge cycles are given in Figure 4.4. The response is normalized with respect to the response of an average buffer cycle and is converted to mass per area through film density measured by XRR. The XRR results were not ideal, so the density, and as such the mass, is likely higher. A calculation is presented in the Appendix (Appendix A:I).

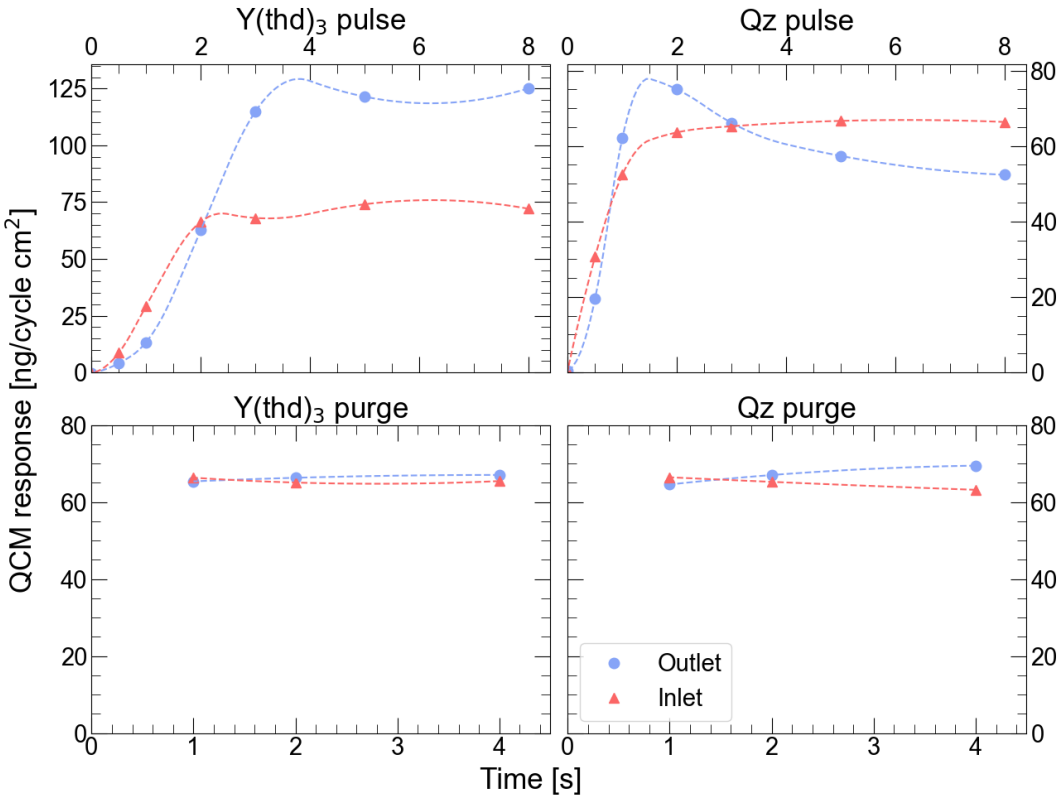

Figure 4.4: QCM response with varied pulse and purge parameters for Y(thd)3 and Qz at 175 °C. The QCM response is normalized in regard to the response of an average buffer cycle (2 s / 1 s / 3 s / 1 s). The measurement of density with XRR was not optimal, so the QCM responses are likely slightly larger.

The data shows that $Y(thd)_3$ saturates at two to three seconds, with a small delay between the inlet and outlet. Qz saturates around two seconds as well. The purges are quite stable already at one second. This indicates that the chosen standard cycle was within sufficient range, though increasing the $Y(thd)_3$ pulse to 3 s would increase the likelihood of full saturation, as 2 s is right on the cusp of saturation. The discrepancy between inlet and outlet could be due to turbulence in the chamber and inlet was decided to be the more trustworthy measurement.

An average long run for this QCM measurement is given in Figure 4.5. It shows the mass increasing during pulses and decreasing somewhat during purges. The signal oscillates with a period of around 1 s (1 Hz), but they are small enough in amplitude to not disturb the overall shape of the graph. The oscillation is attributed to the heating elements affecting the QCM signal when turning off and on while regulating the temperature. There are dips for the purges, that correspond well with desorption of physiosorbed reactants. In addition, we observe a negative response after saturation for the Qz pulse and the two purges.

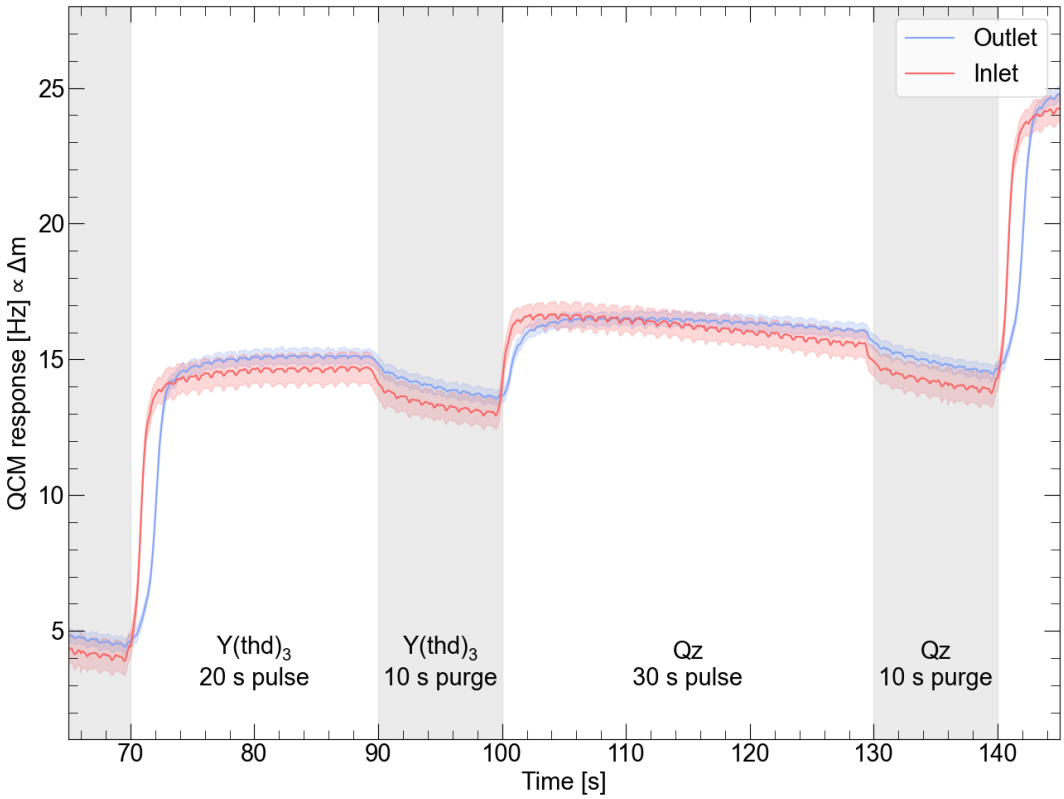

Figure 4.5: Average of 25 QCM long cycles for Y_2Qz_3 growth. Pulses are in white, while purges are in gray. Each step is named with their precursor and duration.

4.2.2 FTIR of Y_2Qz_3

FTIR was performed for a sample of Y_2Qz_3 on an electropolished steel substrate. The results are given in Figure 4.6, together with Qz powder and Al_2Qz_3 film. The results show similarities between the powder and the Qz-films, indicating that Qz is part of the structure, and intact.

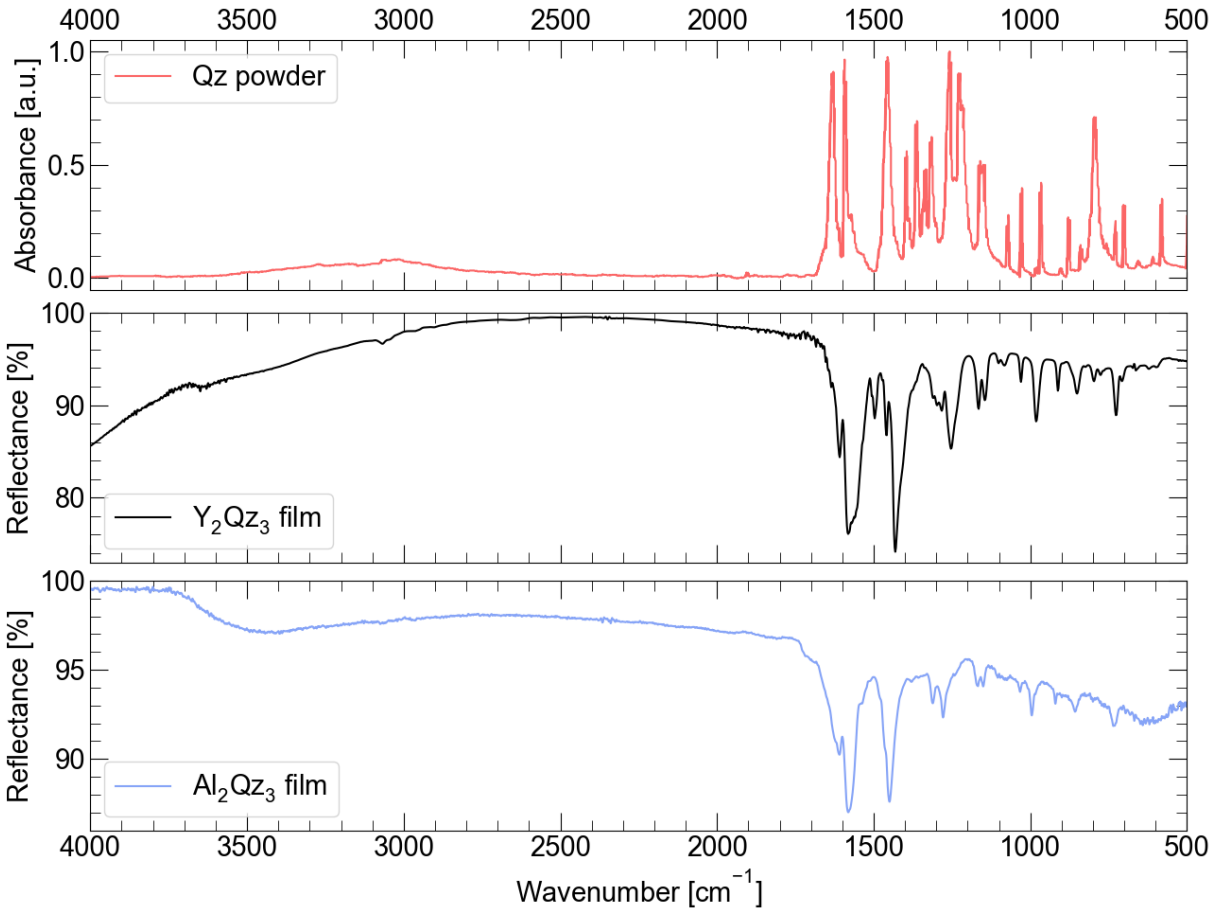

Figure 4.6: FTIR data showing reflectance for a sample of Y_2Qz_3 deposited with 1000 cycles on an electropolished steel substrate. Al_2Qz_3 was measured on a steel substrate and is obtained from [13]. Qz powder was measured in KBr pellets and was obtained from [64]

4.2.3 PL of Ln_2Qz_3

PL was performed with both UV-Vis and NIR detectors on samples of Y_2Qz_3 and Yb_2Qz_3, as well as inspected visually under UV light, and no luminescence was observed.

4.2.4 UV-Vis of Ln_2Qz_3

The transmission and reflectivity of Y_2Qz_3 and Yb_2Qz_3 was measured using UV-Vis, and the data for each was combined as given in Equation (2.2) to calculate their absorption. This is given in Figure 4.7 together with pure glass, and a solution of 10^{-3} M Qz in 5mL ethanol.

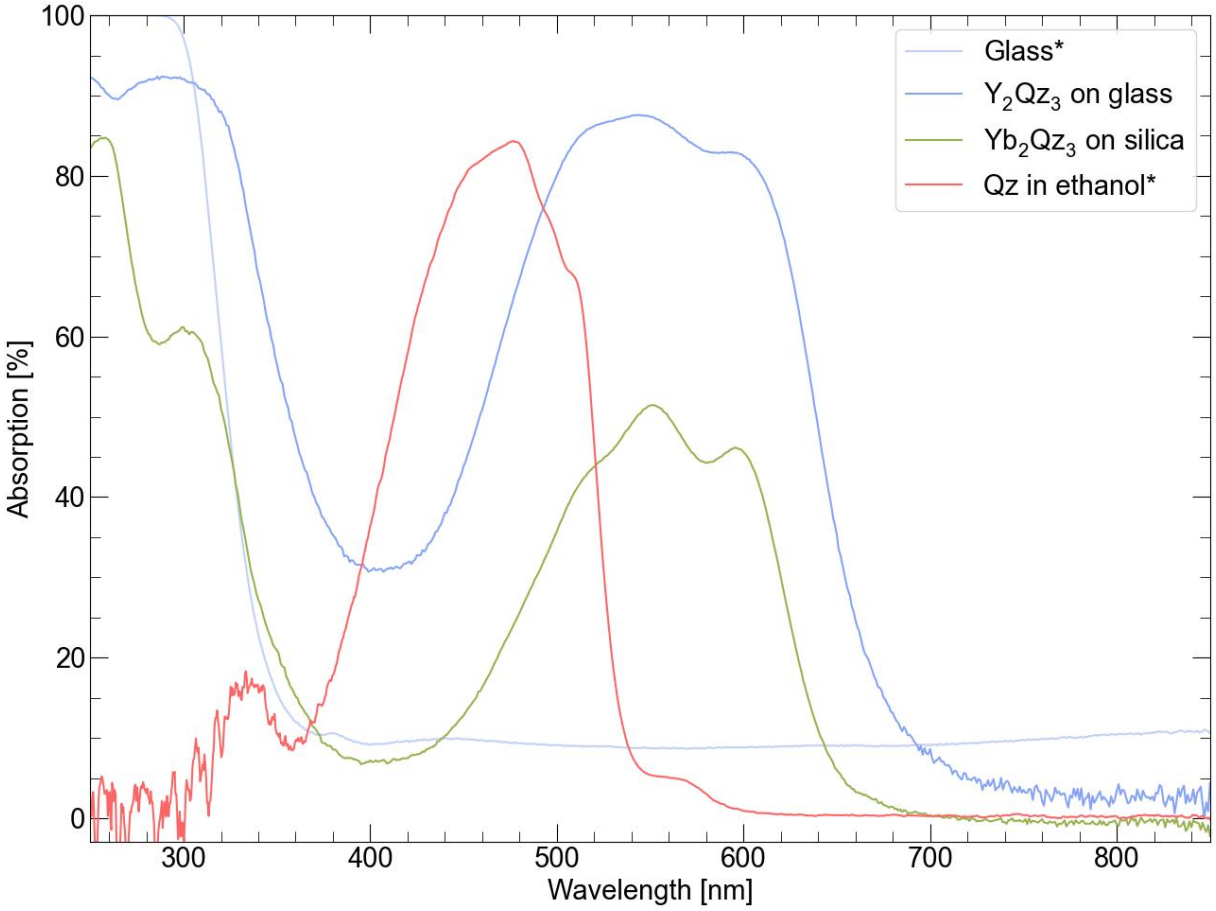

Figure 4.7: Absorption from UV-Vis of a sample of Y_2Qz_3 with 1000 cycles on a glass substrate, a sample of Yb_2Qz_3 with 250 cycles on a silica substrate, a sample of clean glass and a solution of 10^{-3} M Qz in 5 mL ethanol. The data marked with * was calculated using 1-T. The data for the solution was averaged over five data points to reduce noise.

The data shows absorption in the UV, though some of this is attributed to the glass substrate for Y_2Qz_3, as this absorbs in UV. It looks like there are three peaks in the visible spectrum: around 520, 550 and 600 nm. We also observe a red-shift for the absorption going from uncoordinated Qz in solution to metal-coordinated Qz in film.

4.2.5 Temperature dependence on growth of Yb_2Qz_3

With Y_2Qz_3 being well understood, we decided to determine the growth and structure of Yb_2Qz_3, as they seem to grow similarly. Growth of Yb_2Qz_3 was investigated for deposition temperatures between 175 °C and 300 °C, all with 250 cycles.

4.2.5.1 GPC

The growths of Yb_2Qz_3 were investigated using SE. The GPC of these films are given in Figure 4.8 and show a decrease in growth rate with increasing deposition temperature.

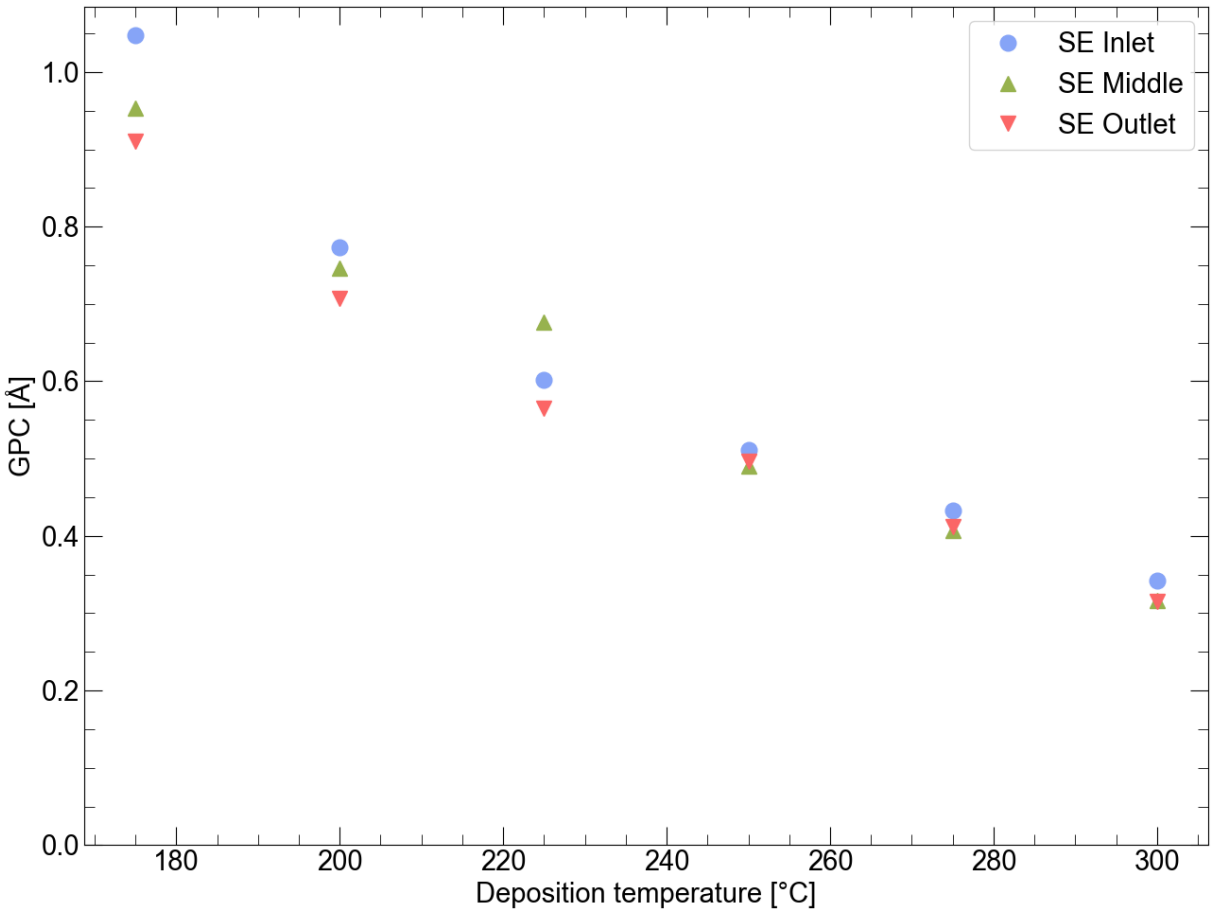

Figure 4.8: GPC of Yb_2Qz_3 vs. deposition temperature. The individual error is smaller than the data markers, and the real error is visualized through including three data points per temperature. The stapled line shows a 1st degree polynomial fit based on the average values.

4.2.5.2 Roughness

Roughness was characterized using SE, with XRR and AFM at 175 °C, and the results are given in Figure 4.9.

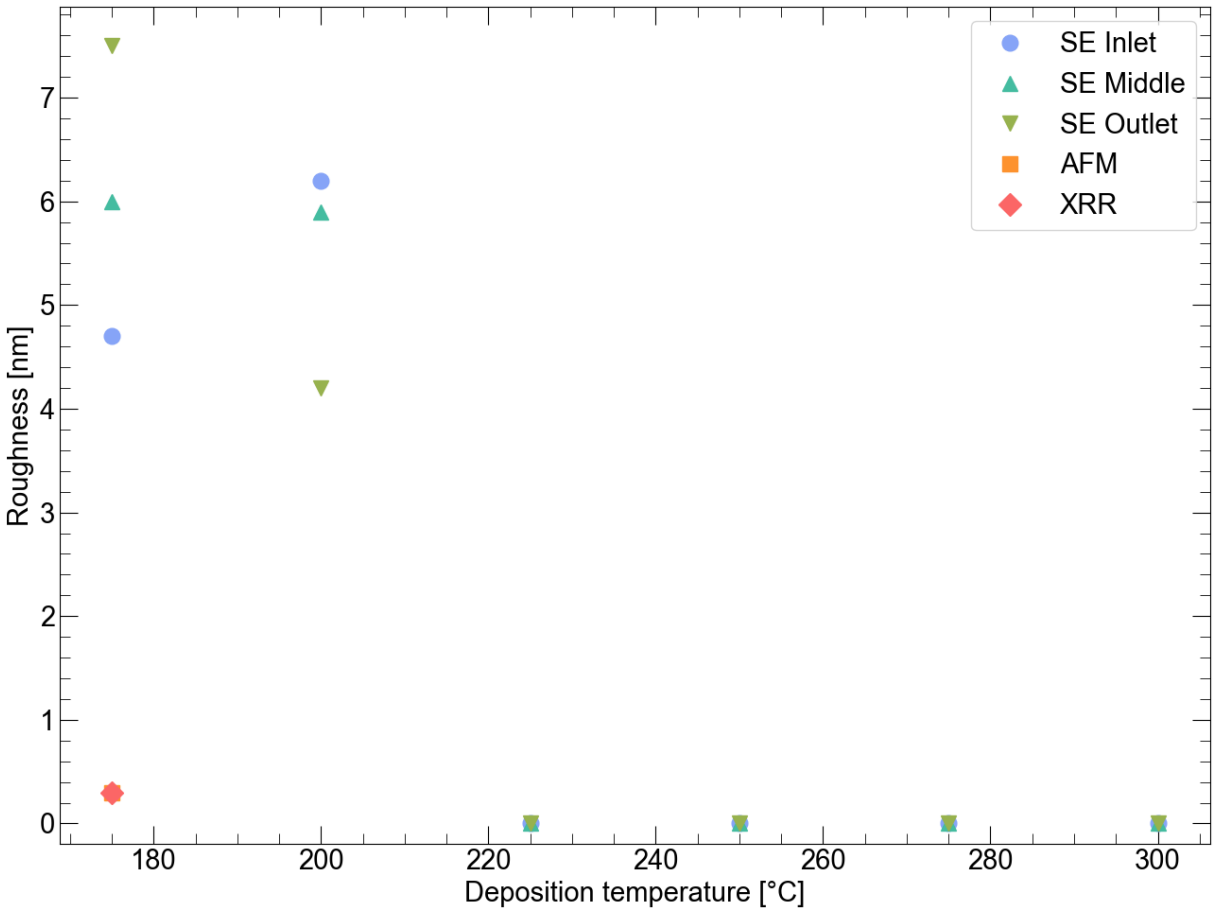

Figure 4.9: Roughness of Yb_2Qz_3 vs. deposition temperature.

At low temperatures, there is an observable roughness that disappears for depositions at 225 °C and above. The low roughness could point towards an amorphous structure, with an ordering at lower temperatures. Since the roughness measured by AFM and XRR is so low, the high values from SE may be misleading.

4.2.5.3 Topography

AFM was performed to investigate the topography and determining surface roughness. In Figure 4.10, an image is given for 175 °C, and shows what resembles crystalline growth, with an overall low roughness.

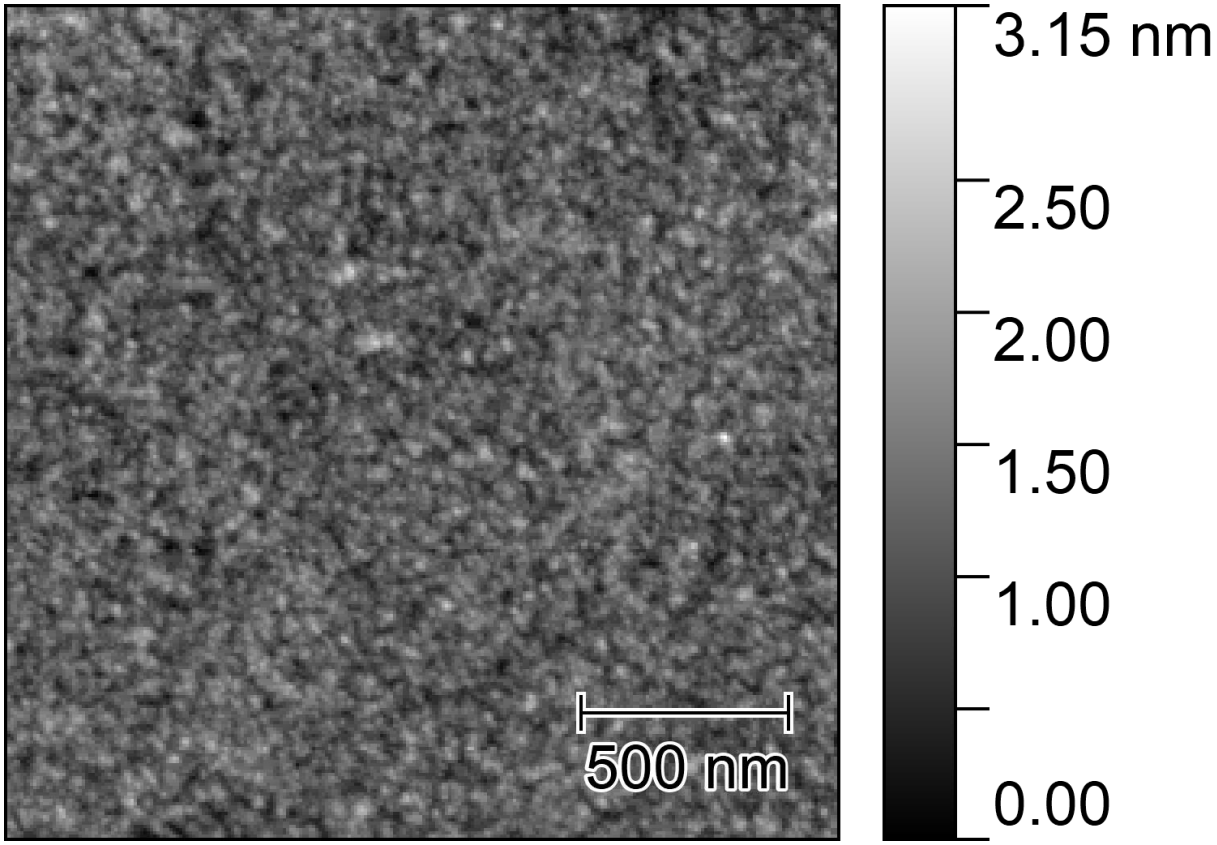

Figure 4.10: 2·2 um^2 AFM image of Yb_2Qz_3 deposited at 175 °C.

4.2.5.4 Crystallinity

Thin films of Yb_2Qz_3 deposited at different temperatures were investigated by XRD to determine the film crystallinity. The resulting diffractograms are given in Figure 4.11, and all show amorphous character for all of the deposited films. Though, there is a small bump around 10° that that could reflect a local ordering This disappears for deposition about around 225 °C.

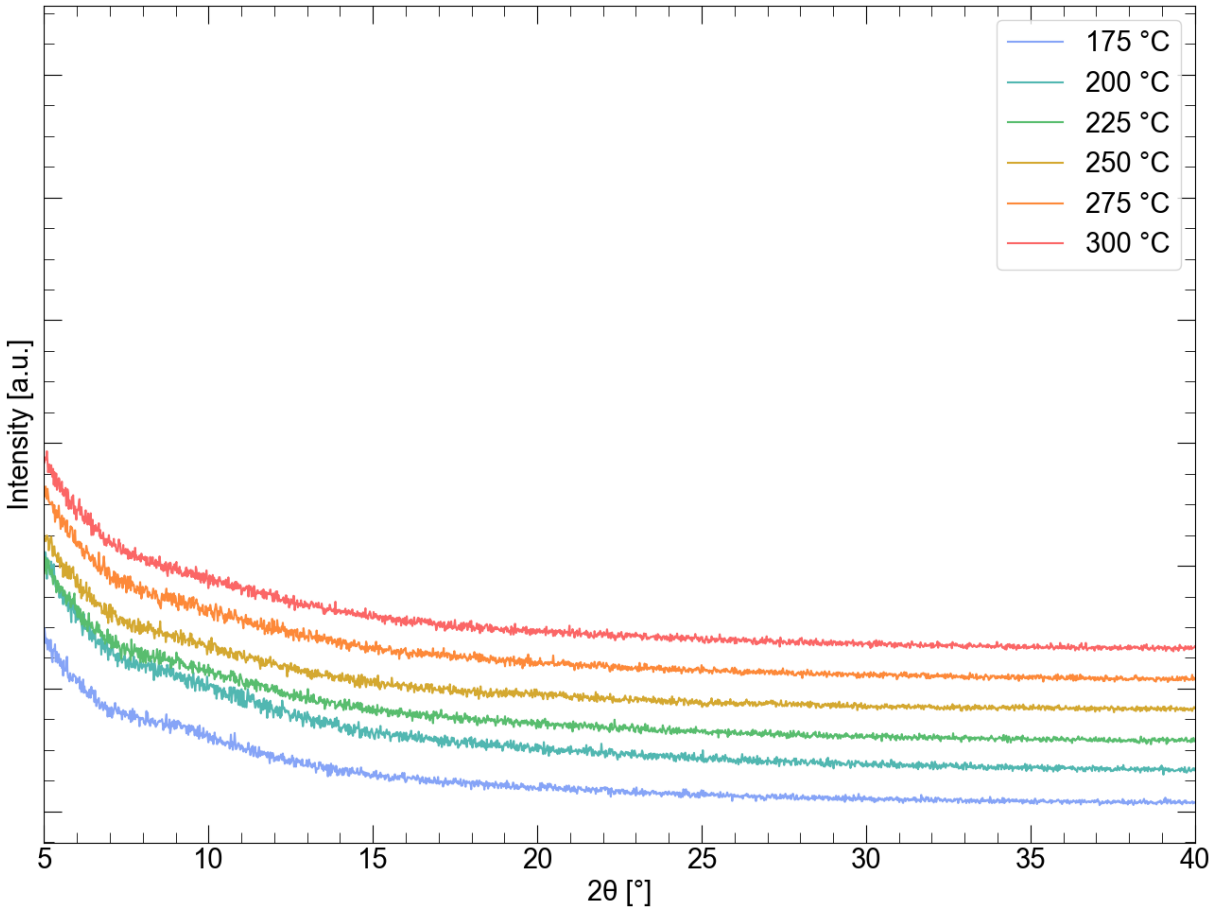

Figure 4.11: XRD spectra of Yb2Qz3 thin films deposited at temperatures between 175 °C and 300 °C. Each measurement is staggered, so intensities are not comparable.

4.2.6 Films

Multiple films of Y_2Qz_3 and Yb_2Qz_3 were deposited. The same Qz precursor was used multiple times without observable changes in growth or visible changes to the powder, indicating it did not decompose. The deposited films show a pink color for low thicknesses with purple for thicker films. Table 4.1 compares two standard films deposited at 175 °C using 250 cycles. The growth rate is high, and the films are quite

even, with 7% difference between inlet and outlet for Y_2Qz_3 and 14% difference for Yb_2Qz_3.

Table 4.1: Film thickness, mean growth rate per cycle, mean roughness and mean refractive index of Ln_2Qz_3 thin films.

Sample	**Film thickness [nm]**			**Growth rate [Å/cycle]**	**Roughness [nm]**	**Refractive index**
	Inlet	Center	Outlet			
Y_2Qz_3 (ETN4014)	87.5	-	81.3	3.4	7.0	1.97
Yb_2Qz_3 (ETN4063)	104.8	95.3	91.1	3.9	6.1	1.96

4.3 Deposition of LnF_3

To characterize growth of LnF_3-types of materials we deposited films of YbF_3, TmF_3, NdF_3 and YF_3. This would provide valuable insight into how these films grow, allowing us to optimize parameters to obtain an ideal ALD growth. It would also give us a good baseline for designing multilayer films later. As a standard, we deposited 1000 cycles at 175 °C, using pulse and purge times of 2 s /1 s /3 s /1 s for $Ln(thd)_3$ / purge / NH_4F / purge. $Yb(thd)_3$ was pulsed for 3 s instead, as it grew more evenly than for 2 s. As most lanthanides grow in a similar way, YbF_3 was investigated the most thoroughly, while TmF_3 and NdF_3 and YF_3 were assumed to be similar in growth and structure to YbF_3. The films were investigated using QCM, XRD and XRR for structural- and growth characterization. SE was used for characterization both of growth and structure through its thickness and roughness, while also being used to measure the index of refraction.

4.3.1 Anion precursor investigation with QCM of NH_4F

One of our initial investigations were to clarify whether LnF_3 films made from treated and untreated anhydrous NH_4F would grow differently. We were suspicious of whether any moisture content in the NH_4F would lead to uncontrolled growth. We investigated this by performing in-situ QCM of YbF_3 with two forms of anhydrous NH_4F. One was stored in a desiccator with P_2O_5 to avoid possible hydration (treated), while the other was stored in the originally purchased container (untreated). The QCM response from precursor pulses and purges are given in Figure 4.12.

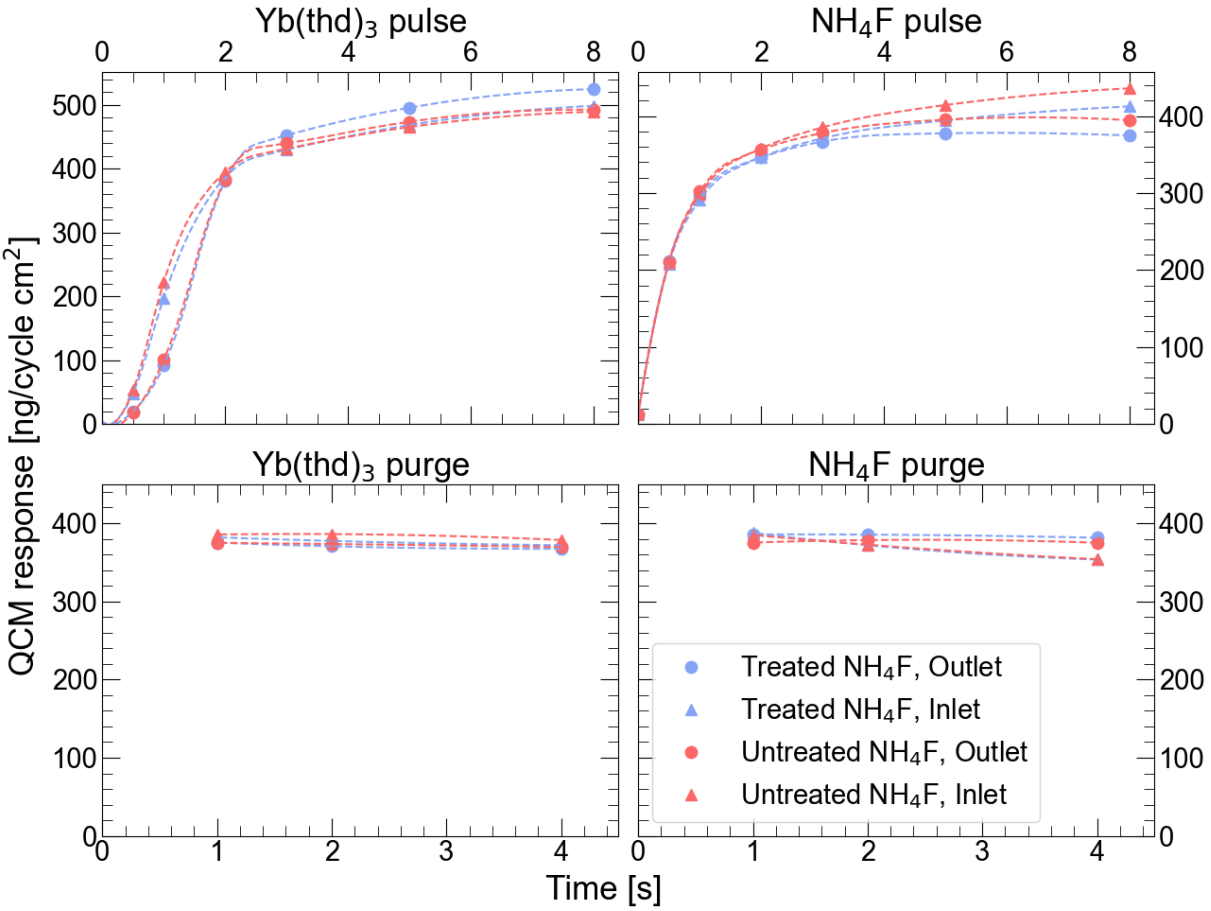

Figure 4.12: QCM response with varied pulse and purge parameters for $Yb(thd)_3$ and NH_4F at 175 °C.

The experiment indicates that there is little to no difference between using treated or untreated NH_4F. Both systems show an identical saturation for the precursor pulses, as well as equally stable purges.

Figure 4.13 presents the long runs for each system. Again, the depositions look indistinguishable, indicating there is little to no difference between treated and untreated NH_4F. Additionally these figures showcase well how the precursors react

and adhere to the surface. The first step shows a large growth as $Yb(thd)_3$ absorbs on the surface. Some of these will react and chemisorb, while others are weakly bonded, being phsysiorbed. The next step is a purge and shows a small decrease in mass. This corresponds to removal of these physisorbed compounds. The NH_4F pulse results in a decrease rather than an increase, reflecting release of heavier thd-type ligands when NH_4F reacts. Finally, the last step of the cycle, a purge, shows again a mass decrease as the physisorbed NH_4F is removed.

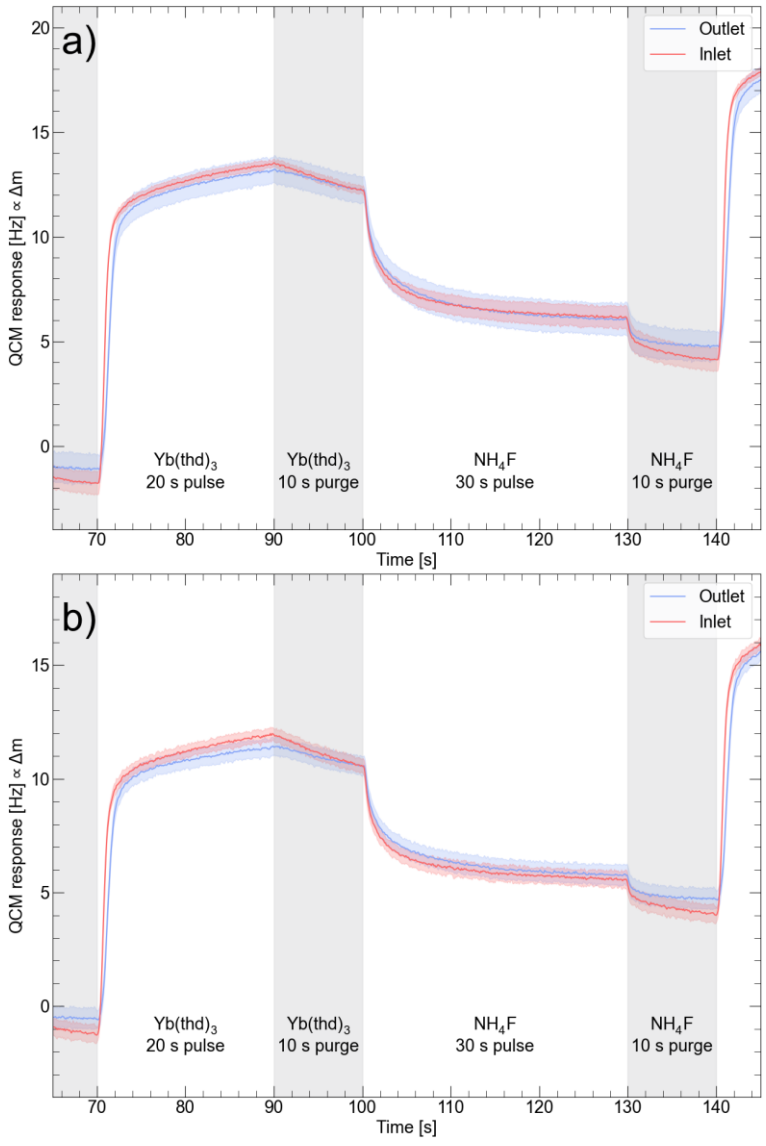

Figure 4.13: Average of 25 QCM long cycles for YbF_3 growth using treated (a) above) and untreated (b) below) NH_4F. Pulses are in white, while purges are in gray. Each step is named with their precursor and duration.

Though both treated and untreated NH_4F showed similar results, we settled on using treated NH_4F to avoid potential impurities from presence of water in the compound, as this can work as a reactant and lead to growth of oxides.

4.3.2 QCM of YbF_3 from $Yb(thd)_3$ and NH_4F

The anion precursor investigation also forms the basis for selecting the pulse and purge parameters for growth of YbF_3. Figure 4.12 shows that $Yb(thd)_3$ and NH_4F is at the cusp of saturation for a 2 s pulse. We therefore settled for a 3 s pulse for of both reactants for the following experiments. The purges showed little to no difference with increasing purge time, indicating that a purge time of 1 s was enough.

4.3.3 QCM of NdF_3 from $Nd(thd)_3$ and NH_4F

Like for YbF3, NdF3 was investigated with QCM. Figure 4.14 shows that there is no saturation for Nd(thd)3 indicating there could be a CVD component to the film growth. The NH_4F pulse does show an initial saturation, but then increases again around 5 s.

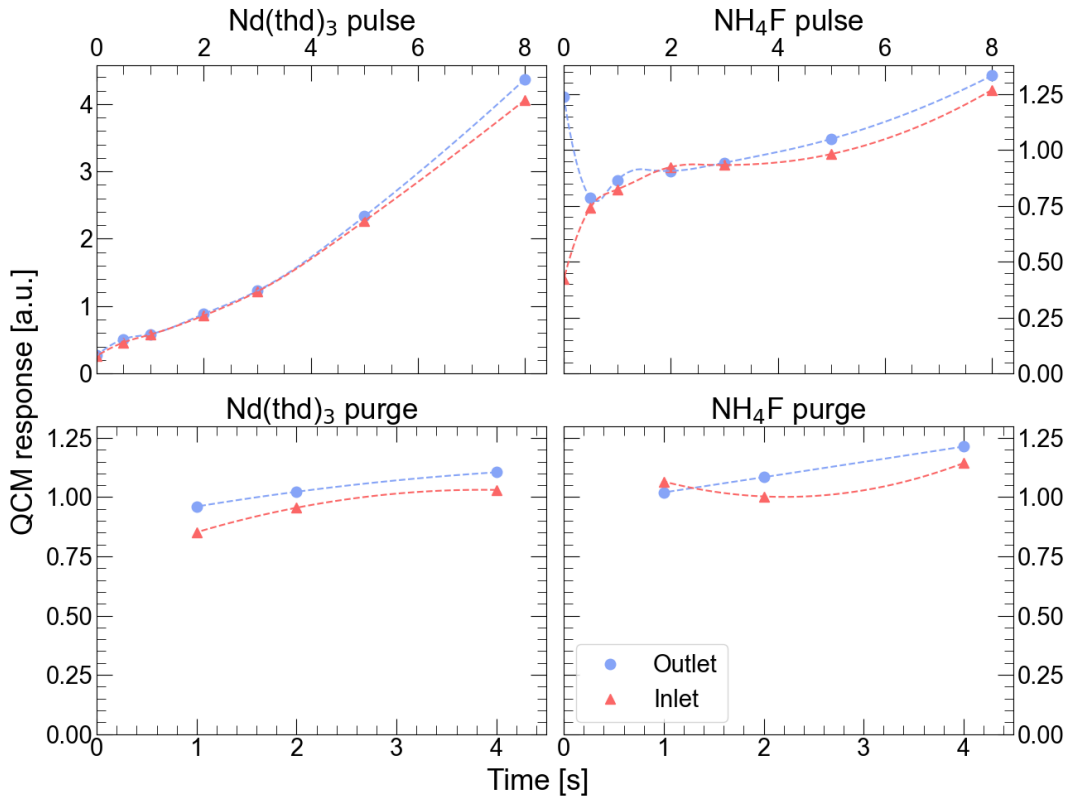

Figure 4.14: QCM response with varied pulse and purge parameters for $Nd(thd)_3$ and NH_4F at 175 °C. The QCM response is normalized in regard to the response of an average buffer cycle (2 s / 1 s / 3 s / 1 s).

In Figure 4.15 an average long cycle QCM response for NdF_3 is given. It shows that even for 20 s $Nd(thd)_3$-pulses there is no saturation. Though, the NH_4F pulse seems to saturate. There is a slight mass increase during the purges, even though the purges do show to remove physisorbed species. This appearance is most likely due to thermal fluctuations during growth, though they could also indicate a possible leak.

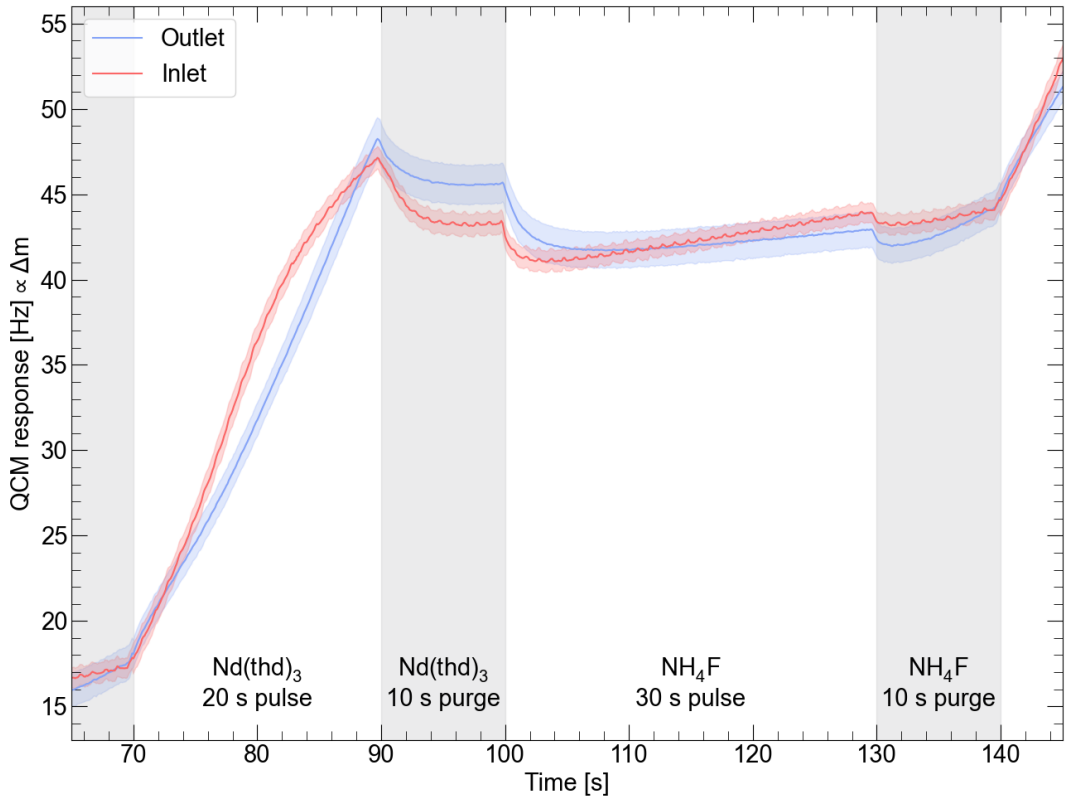

Figure 4.15: Average of 16 QCM long cycles for NdF_3 growth. Pulses are in white, while purges are in gray. Each step is named with their precursor and duration.

4.3.4 QCM of TmF_3 from $Tm(thd)_3$ and NH_4F

QCM investigation of TmF_3 was performed, with the results given in Figure 4.16. There is a clear sign of saturation during pulsing of $Tm(thd)_3$, although not complete, indicating there could be a CVD component in the growth. The NH_4F pulse appears more clearly saturating at around 3 s, despite scattering of the data.

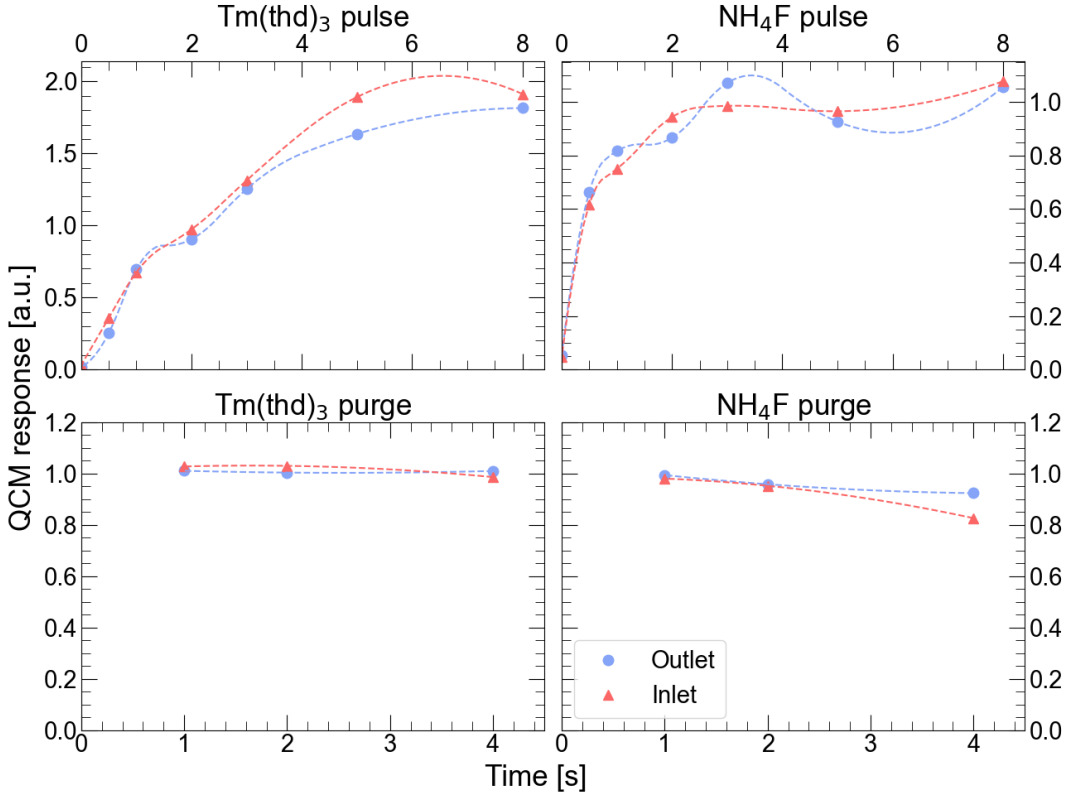

Figure 4.16: QCM response with varied pulse and purge parameters for $Tm(thd)_3$ and NH_4F at 175 °C. The QCM response is normalized in regard to the response of an average buffer cycle (2 s / 1 s / 3 s / 1 s).

An average long cycle is given in Figure 4.17. This shows large uncertainties, but overall, the shape we would expect. The $Tm(thd)_3$ pulse shows a clear initial rise in mass before reducing its mass increase, though the growth does not completely halt. This indicates partial CVD growth.

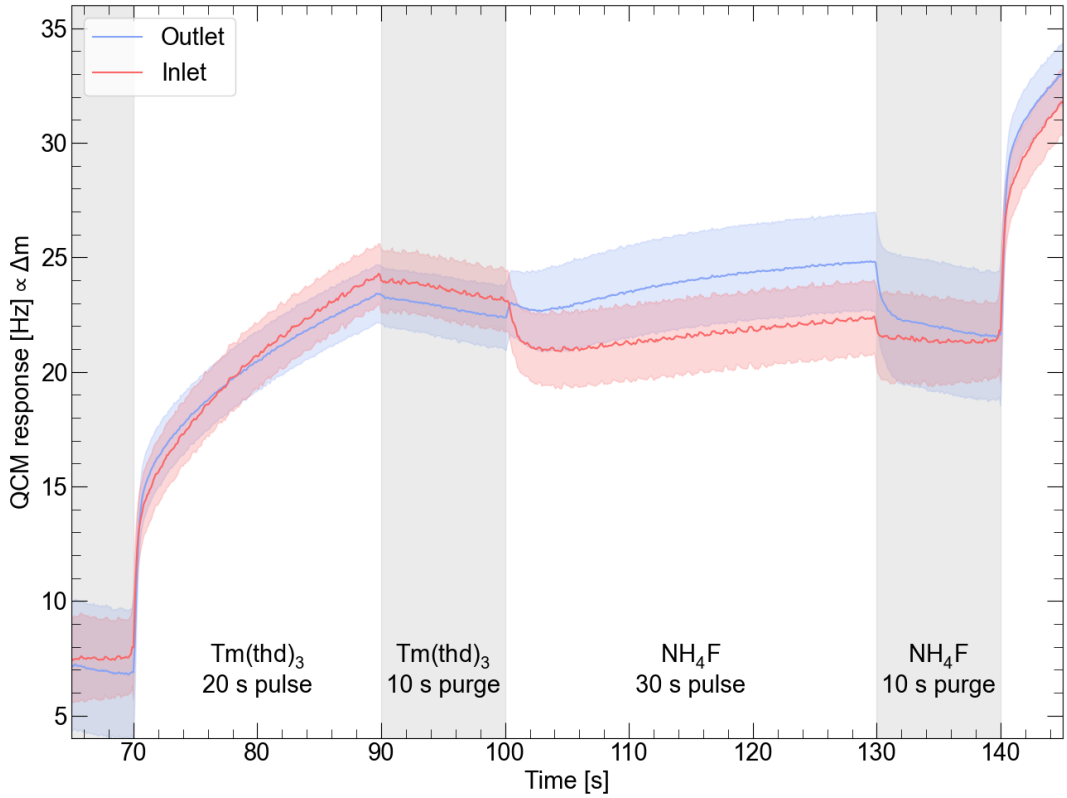

Figure 4.17: Average of 16 QCM long cycles for TmF_3 growth. Pulses are in white, while purges are in gray. Each step is named with their precursor and duration.

4.3.5 QCM of YF_3 from $Y(thd)_3$ and NH_4F

Results from QCM measurements of YF_3 are given in Figure 4.18. There is a very slow saturation of $Y(thd)_3$, likely showing a CVD component in the growth. The NH_4F pulse shows a slight decrease for long pulse times. This may be due to thermal effects from how the QCM experiment was performed. There is a discrepancy between inlet and outlet for the NH_4F purge. Still, the purges seem sufficient at 1 s.

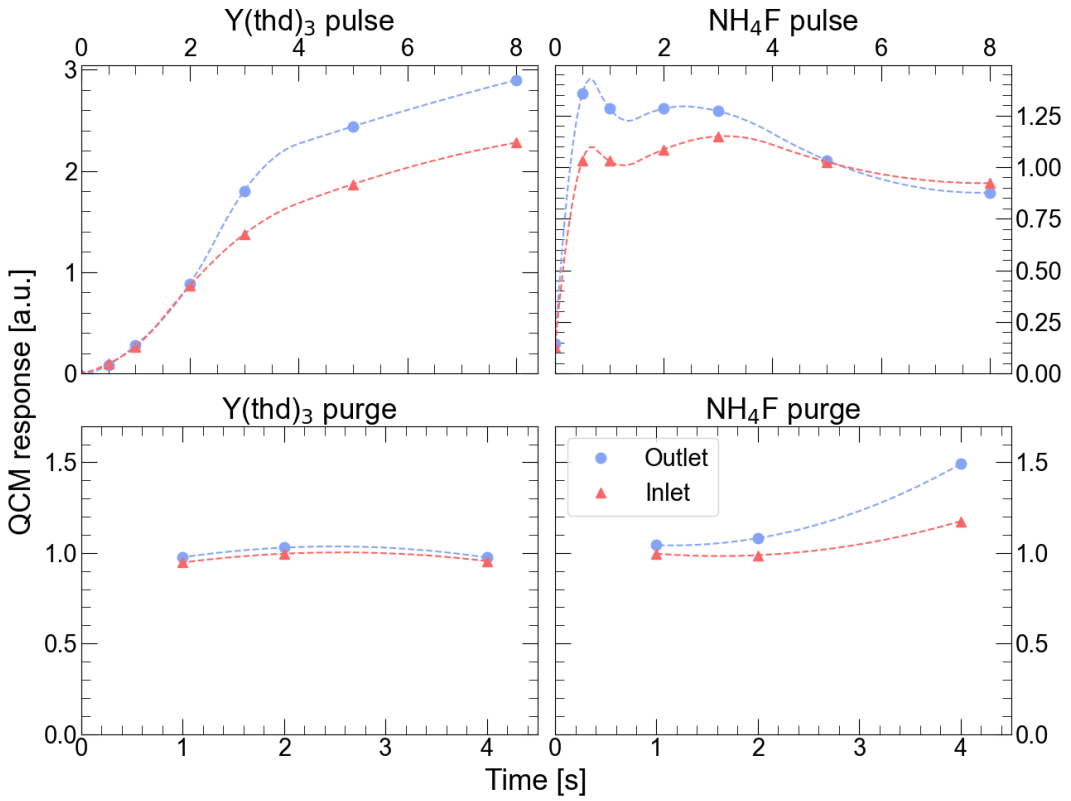

Figure 4.18: QCM response with varied pulse and purge parameters for $Y(thd)_3$ and NH_4F at 175 °C. The QCM response is normalized in regard to the response of an average buffer cycle (2 s / 1 s / 3 s / 1 s).

In Figure 4.19 an average long cycle of YF_3 is given. It clealy shows a slowing of $Y(thd)_3$ growth during its pulse, where the excess is desorbed during the following purge.There is a near saturation of NH_4F, with a clear removal of physisorbed species during the purges.

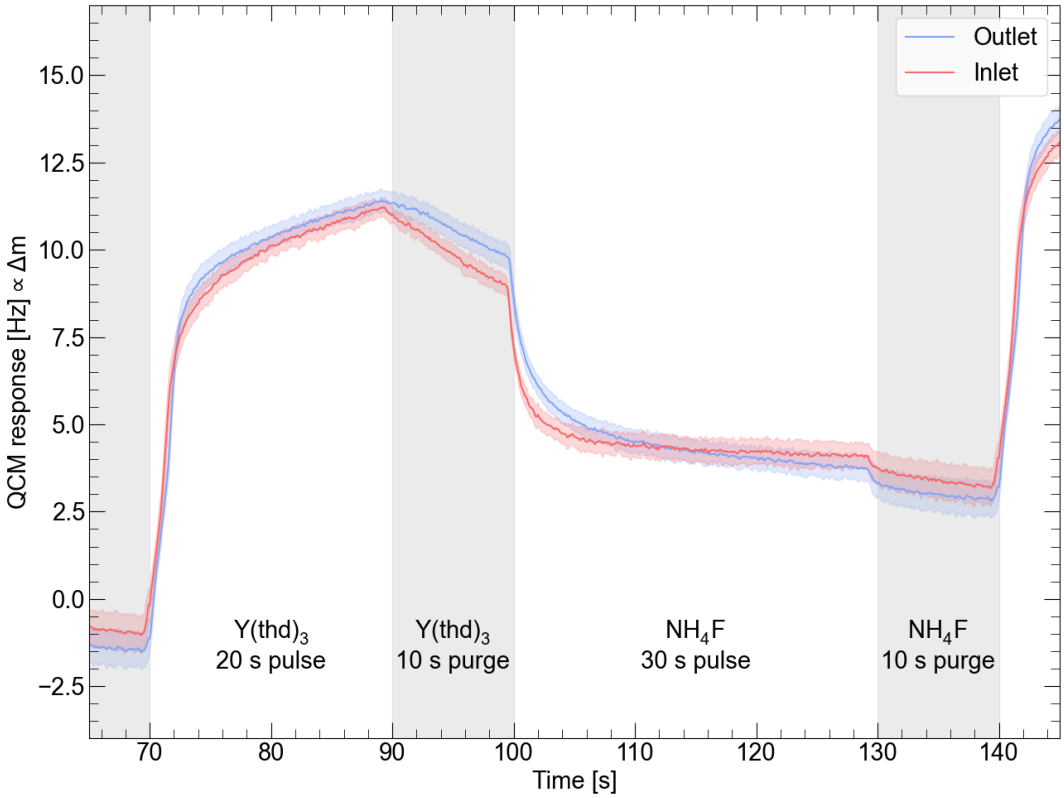

Figure 4.19: Average of 9 QCM long cycles for YF_3 growth. Pulses are in white, while purges are in gray. Each step is named with their precursor and duration.

4.3.6 Temperature dependence on growth of YbF_3

YbF_3-films were deposited at temperatures between 175 °C and 300 °C to investigate how its growth and structures changes with increasing temperatures. All films used 3 s / 1 s / 3 s / 1 s for $Yb(thd)_3$ / purge / Nh_4F / purge and 1000 cycles.

4.3.6.1 Growth Per Cycle (GPC)

To investigate the growth of YbF_3-films we performed SE and XRR measurements. The Growth Per Cycle (GPC) for these are given in Figure 4.20. The measurements from SE are given for 175, 200, 225, 250, 275 and 300 °C. XRR results are provided for 175, 225 and 300 °C.

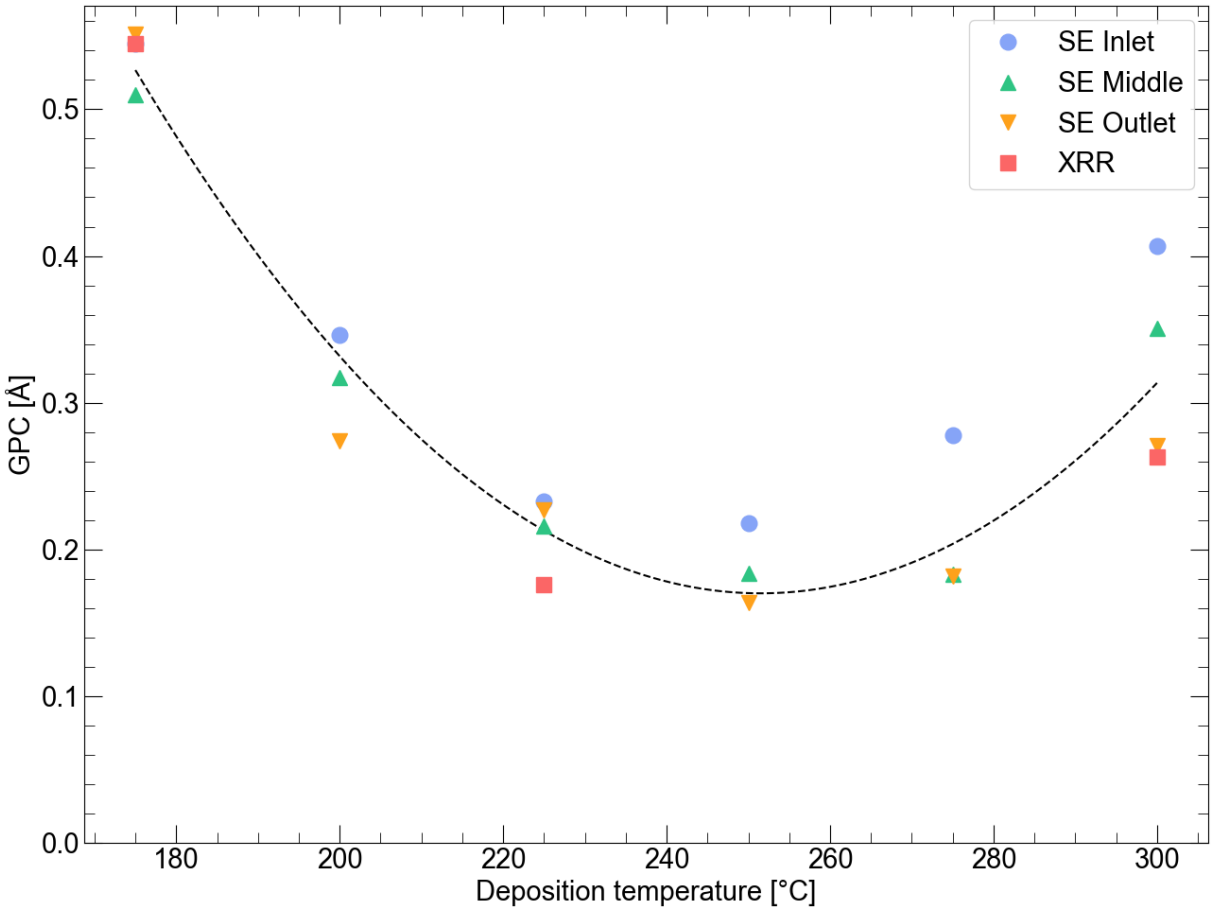

Figure 4.20: Thickness of YbF_3 vs. deposition temperature, with a black stapled line showing a 2nd degree polynomial fit of average measurements. Ellipsometry measurements were performed on samples near inlet, middle and outlet in the reaction chamber. XRR measurements were performed on a sample from around the middle.

The data shows a decrease in growth with increasing temperature, until around 250 °C, where it begins increasing. This indicates a change in growth mechanism or film structure, for example a change from growth of amorphous to crystalline material.

4.3.6.2 Roughness

Roughness was measured using SE, XRR and AFM. The results of which are given in Figure 4.21.

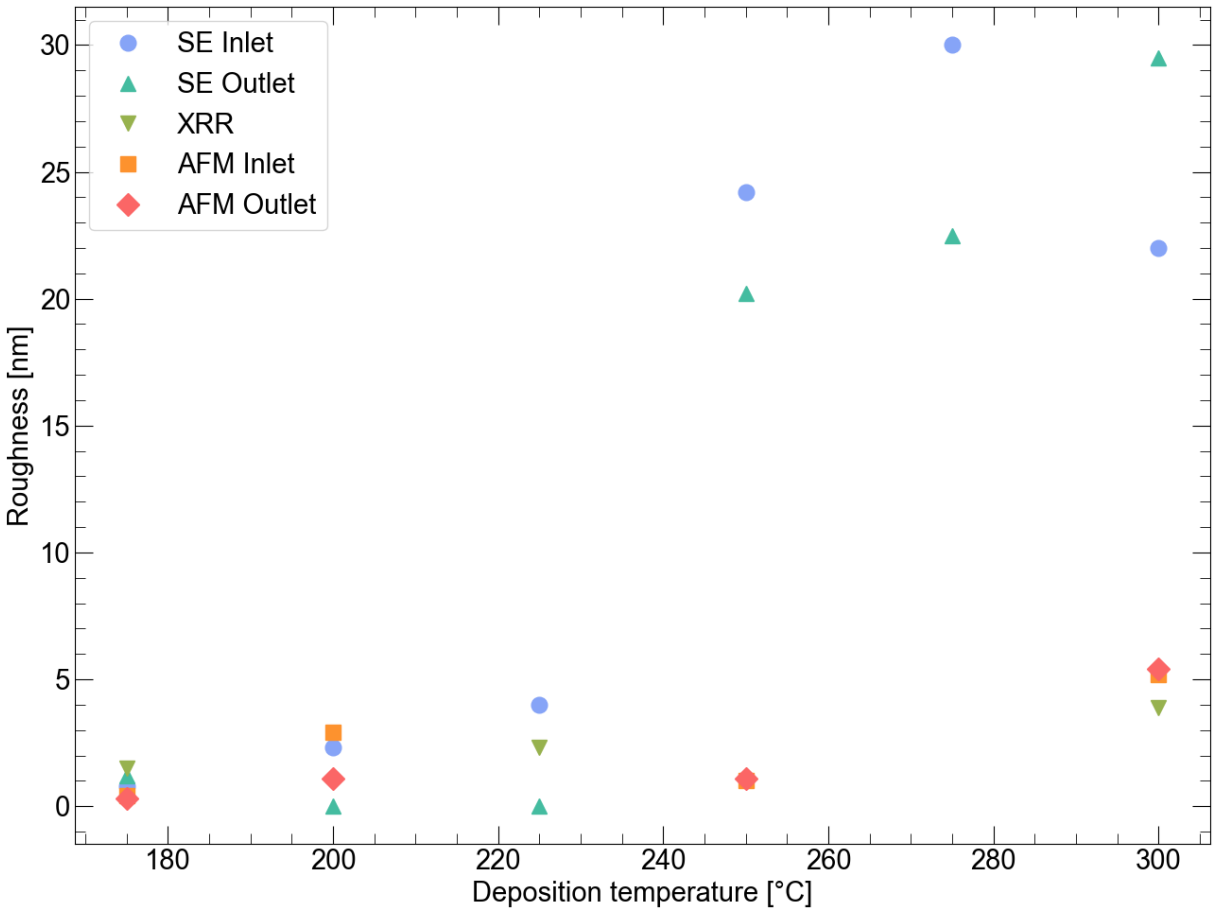

Figure 4.21: Roughness of YbF_3 vs. deposition temperature. SE was performed for all temperatures. XRR was performed for 175, 225 and 300 °C. AFM was performed for 175, 200, 250 and 300 °C.

The measured roughness increases with deposition temperature for all techniques, with SE having a sharp increase at 250 °C. XRR and AFM also show an increase, though much weaker. The large discrepancy could indicate methodological differences in how these techniques interpret roughnesses.

4.3.6.3 Topography

The surface was imaged using AFM to observe visual changes and determine surface roughness as the deposition temperature increased. The surface roughness is reported under the previous section. Pictures of the surface is given in Figure 4.22 and Figure 4.23.

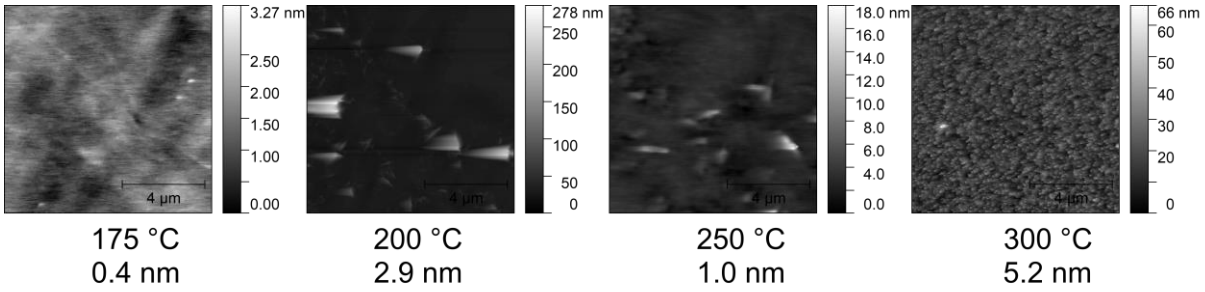

Figure 4.22: 10·10 um² AFM images taken of inlet samples at different deposition temperatures. The roughness of each measurement is included under the picture.

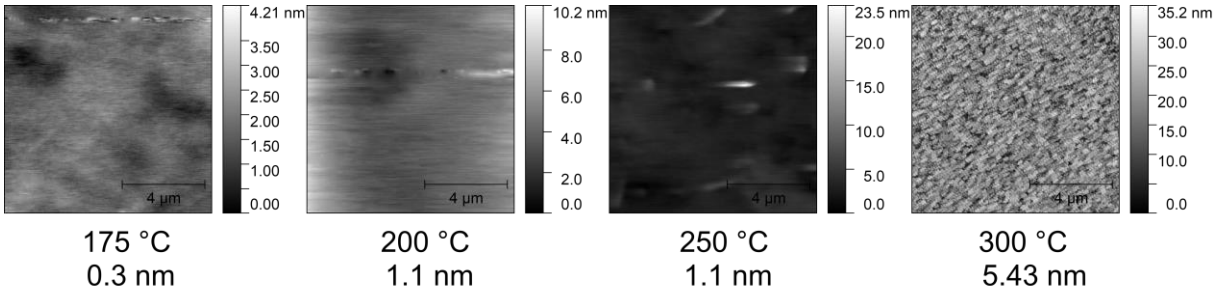

Figure 4.23: 10·10 um² AFM images taken of outlet samples at different deposition temperatures. The roughness of each measurement is included under the picture.

The pictures indicate an even surface at low temperatures. When the temperature increases to 225 °C (250 °C at the outlet) we begin seeing what resembles nucleation of crystallites. For 300 °C the surface is quite rough and could indicate crystalline growth.

4.3.6.4 Crystallinity

Finally, the films were investigated using XRD. This would confirm if growth of crystalline material is occurring at elevated temperatures. The resulting diffractograms are given in Figure 4.24.

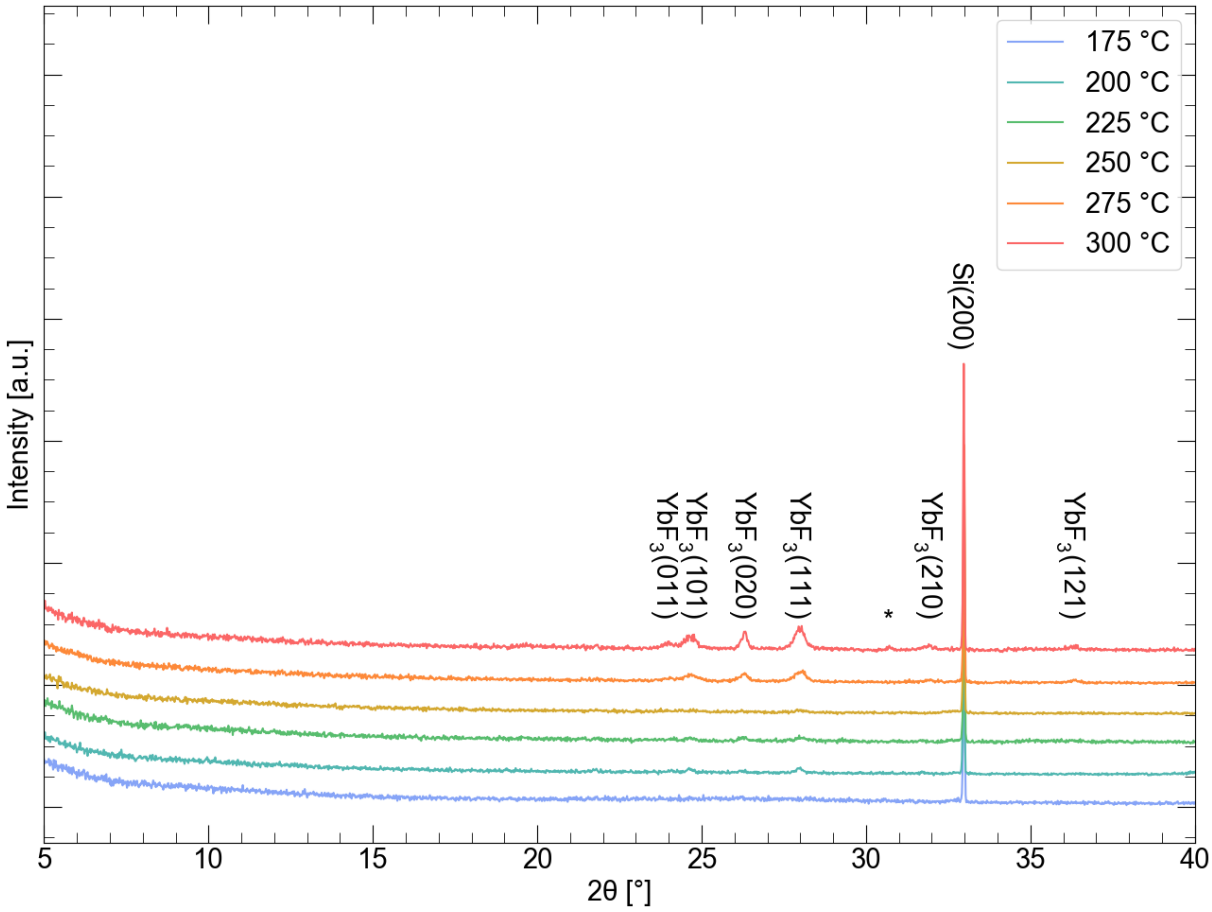

Figure 4.24: XRD spectra of YbF_3 deposited at different temperatures. Peaks are annotated, with * symbolizing an unidentified peak. The spectra are staggered, so measurement intensities are not comparable.

The spectra confirm crystalline growth of YbF_3 at increased temperatures. In fact, already at 200 °C, the peaks indicating crystalline YbF_3 show up, indicating that the growth of crystals begins already there. There is also crystalline growth of an unknown phase visible at 300 °C.

4.3.7 Films

Multiple standard films of LnF_3 were deposited during the project, and these are presented in Table 4.2.

Table 4.2: Film thickness and mean GPC, roughness, and refractive index of LnF_3 thin films. All films were deposited with treated NH_4F, except for ETN4002, which was deposited with untreated NH_4F. The data marked with * was only measured on the inlet.

Sample	**Film thickness [nm]**			**Growth rate [Å/cycle]**	**Roughness [nm]**	**Refractive index**
	Inlet	Center	Outlet			
YbF_3 (ETN4002)	32.6		27.7	0.3	6.3*	1.56*
YbF_3 (ETN4008)	38.2		31.5	0.3	2.6*	1.54*
YbF_3 (ETN4051)	54.5	51.0	55.1	0.5	0.8	1.53
TmF_3 (ETN4054)	59.6	57.1	57.4	0.6	0.1	1.53
NdF_3 (ETN4055)	89.8	64.4	49.9	0.7	24.9	1.61
YF_3 (ETN4031)	69.6	-	50.0	0.6	2.0	1.52

The table shows that all the investigated LnF_3 films grow fairly similarly, with an exception for NdF_3, which grows with a surprisingly high gradient of 57% between inlet and outlet, and an extremely high roughness, where inlet was around 38 nm and outlet was around 16 nm. It also shows a higher index of refraction than the other films, indicating a different growth. The YbF_3 films ETN4002 and ETN4008 were deposited with untreated and treated NH_4F, respectively. They indicate similar growths and refractive indexes.

4.4 Incorporation of Qz in YbF_3

With the pure thin films investigated, it was time to explore the properties that would arise from doping Qz in the LnF_3 films. As presented in 4.2.3, thin films of Y_2Qz_3 and Yb_2Qz_3 did not show luminescence. A possible reason for this may be concentration quenching, and as such they were attempted diluted in YbF_3 to different degrees. Two samples of YbF_3 with Yb_2Qz_3 were prepared with 50 and 250 cycles of separation, respectively

4.4.1 UV-Vis of Yb_2Qz_3-doped YbF_3

UV-Vis was performed on YbF_3 samples with varying amounts of Yb_2Qz_3, along with pure Yb_2Qz_3 as a reference. The spectra are given in Figure 4.25, and show increasing absorption with a higher content of Yb_2Qz_3, up to a maximum for pure Yb_2Qz_3.

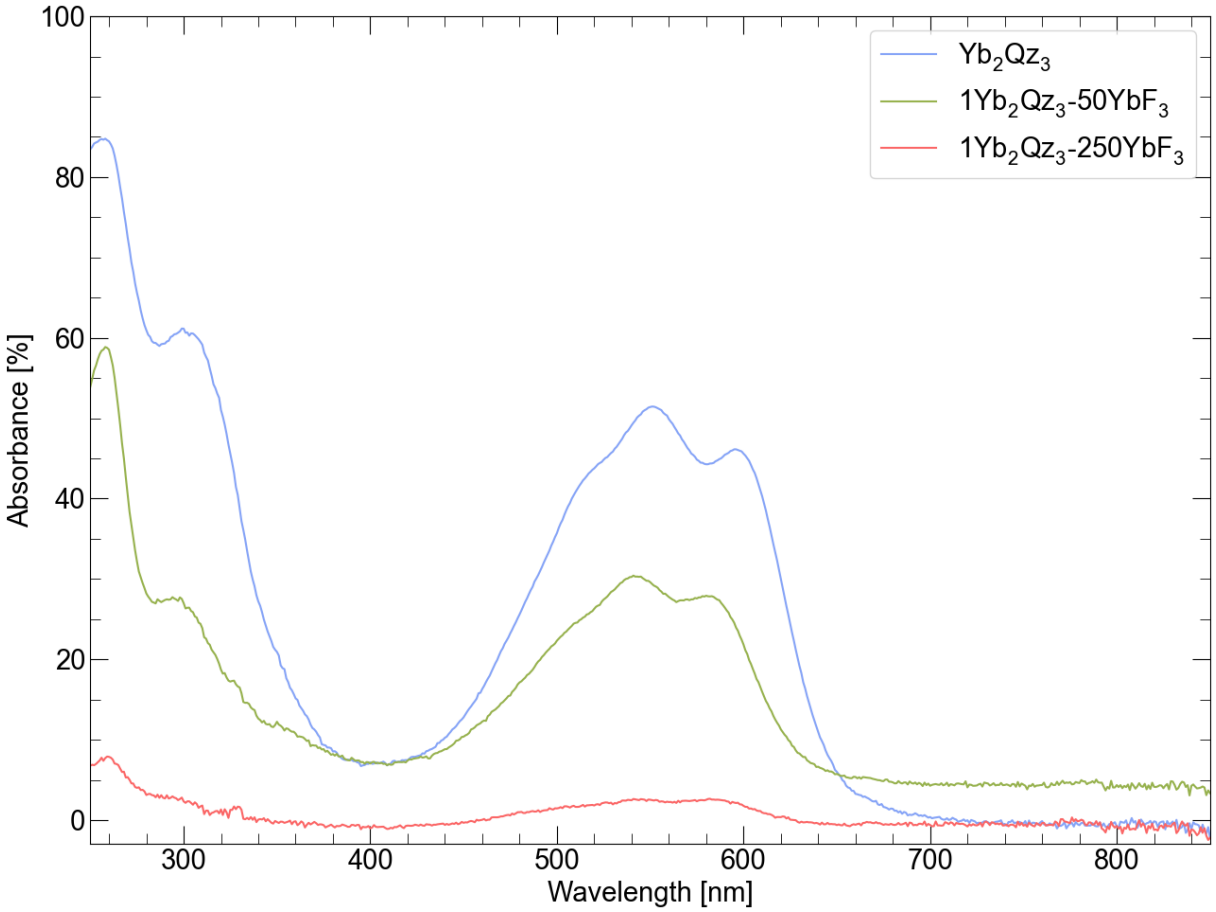

Figure 4.25: Absorption from UV-Vis measurements of Yb_2Qz_3-doped YbF_3 samples (1:50 had 3110 cycles with 60 multilayers, 1:250 had 1003 cycles with 3 multilayers) and a sample of Yb_2Qz_3 (250 cycles) all on silica substrates.

4.4.2 PL of Qz-doped YbF_3

PL was performed on the Qz-doped films, and no luminescence was observed, either at UV, visible or NIR wavelengths.

4.5 Upconversion multilayer films

We performed investigations of upconversion system without sensitization. Multilayer YbF_3 films with doped cycles of NdF_3 and TmF_3 had been prepared by Silje Sørensen to observe the change in energy transfer with varying cycles of separation [12].

4.5.1 CL of multilayer LnF_3 films

The films were investigated using CL-SEM. The strongest peak was integrated over, and its intensity was graphed vs. the separation between NdF_3 and TmF_3. The results are given in Figure 4.26, and show a peak in intensity around 40 cycles of separation, corresponding to 0.8 nm, given Silje Sørensen's growth rate of 0.2 Å/cycle for YbF_3.

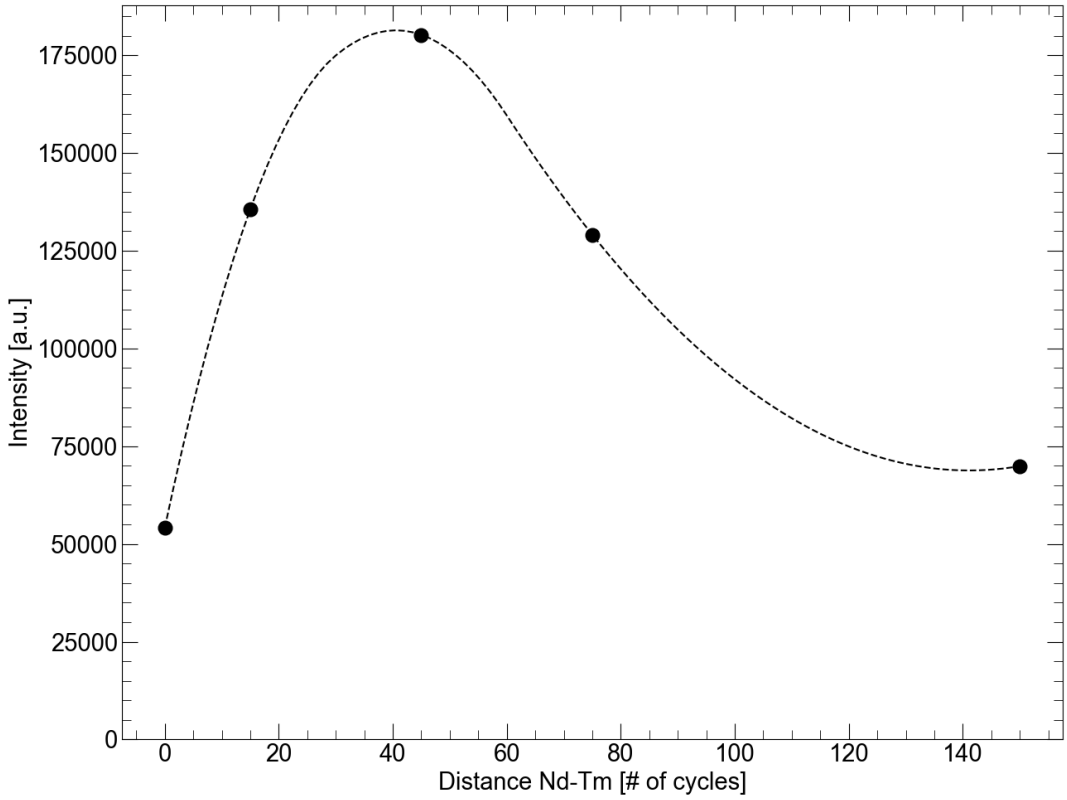

Figure 4.26: CL intensity of 300 nm peak for samples of samples of NdF_3-xYbF_3-TmF_3. The stapled line is a quadratic interpolation of the measurement points.

4.6 Summary of Results

A flowchart summarizing the central results of the chapter is given in Figure 4.27, and gives an overview of the various parts of the project with its general structure.

Figure 4.27: Summary of experimental steps in the performed with their main results.

5 Discussion

This chapter will relate the results to each other and to results from known literature, allowing for an in-depth discussion of the discoveries that have been made during the project. The chapter is divided similarly to the previous chapter, beginning with the eligibility of Qz, before discussing Ln_2Qz_3 films, LnF_3 films, Qz-doped films and finally multilayer films.

5.1 Eligibility of Qz

The investigations of photoluminescence of various salts in ethanol solutions in 4.1 proved that the organic anions (acac and thd) led to reduction of luminescence, with thd almost killing the luminescence entirely. This could be due to multiple reasons.

One possibility is that the large anions sterically hinder Qz from coming in proximity to the cation. This explains the lack of charge transfer, but not the lack of Qz luminescence, as it luminesces without cations present. It should be noted that the ratio between thd and Qz in the solutions were 10:1, and that we do not know the relative chelating ability of neither of these molecules. Energy transfer by exchange interactions drops quickly for distances above 1 nm and is likely heavily impacted by such a hinderance. Coulomb interactions will also be limited, though it can have a range of 3.5 nm. At this point, we do not know what the dominating mechanism is.

Another possibility is that the luminescence is quenched due to a change in pH. Qz has been reported to emit strong fluorescence for pH values below 10, but with a color change from orange to purple (in dichloromethane) and fluorescence quenching for higher values [65]. Hthd has a predicted pKa value of 11.6 [66]. This means it is a weak acid, and as such the pH of the Hthd-solutions will not be above pH 10, as is shown in Appendix A:II.a. However, with Hthd being a weak acid, the thd^- ligand is necessarily a correspondingly strong base. pKb of the thd^- anion is 2.4 and calculating the pH of the thd^--solutions as if water was the solvent, we obtain a value of just under 11, which is above the transition pH for Qz. See Appendix A:II.b for the calculation. This matches well with the different colors of the thd^--solutions in Figure 4.1. However, since Figure 4.3 shows a vast difference in luminescence when using Hthd as well, pH is most probably not the only reason for the observed quenching. It should also be kept in mind

that our solutions are ethanol-based and not water-based, and hence the pH-calculations will be perturbed by the solvent.

The observed quenching could also be due to that Qz and thd form a charge-transfer complex where a temporary electron transfer could quench the luminescence from Qz. This has not been investigated, however.

There may be multiple mechanisms causing the observed quenching, where pH is a likely candidate for the thd^--solutions, and steric hinderance might play a role. The formation of a charge-transfer complex can seem plausible given the quenching of pure Qz-luminescence by addition of Hthd. Since Y^{3+} luminesces even in the presence of thd^-, it increases the likelihood that Qz could function in a solid film under the right conditions.

However, investigations of the dried powder revealed that the solid form of Y_2Qz_3, and Al_2Qz_3 did not luminesce. This can be due to aggregation-caused quenching (ACQ), where luminescent molecules with cyclic structures, similar to Quinizarin, form aggregates [67]. These aggregates form due to π-π stacking interactions and/or dipole-dipole interactions. This leads to either weak fluorescence or no fluorescence at all. A method to reduce ACQ is to dilute the fluorescent molecules in a solid matrix, i.e., using them as dopants.

5.2 Deposition of Ln_2Qz_3

5.2.1 ALD Growth

The QCM results from Y_2Qz_3 in Figure 4.5 show a clear saturation of the precursors with desorption during purges and is a strong indication of ALD-type growth. The overall reaction mechanism can be investigated by inspecting the relative mass increase during reaction of the individual reactants. This is presented as Δm_1 and Δm_2 in Figure 5.1 and is the change in QCM response from the start of a precursor pulse to the end of its purge.

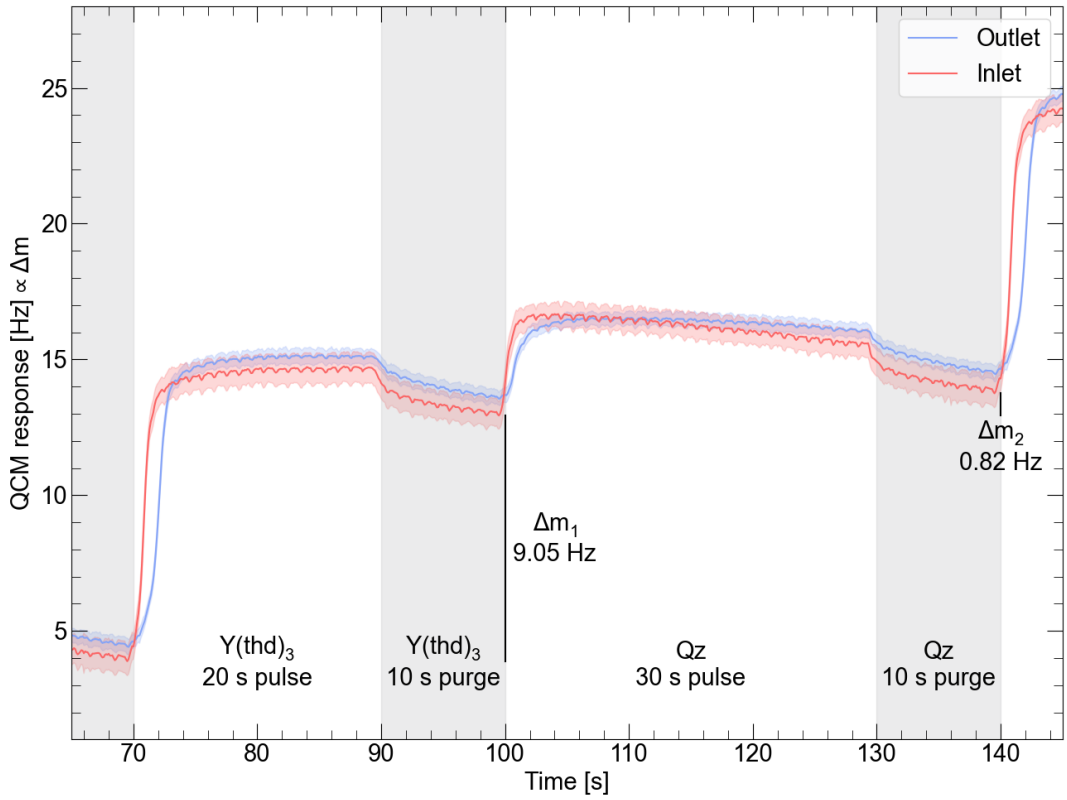

Figure 5.1: Average of 25 QCM long cycles for Y_2Qz_3 growth. The figure is marked with the relative increase for one $Y(thd)_3$ half-cycle (Δm_1) and one Qz half-cycle (Δm_2) for the inlet.

We observe a change in mass of 9.05 Hz for the reaction with $Y(thd)_3$ and 0.82 Hz for the reaction with Qz. Since the change in frequency is proportional to the mass change, the relative difference of Δm_1 and Δm_2 can be compared to the calculated mass change for proposed reaction mechanisms. Assuming a stoichiometry of Y_2Qz_3 the reaction for pulsing of $Y(thd)_3$ can be described by Equation (5.1), while the reaction for pulsing Qz can be described by Equation (5.2).

$$|\text{–}(OH)_{x(s)} + Y(thd)_{3(g)} \rightarrow |\text{–}O_xY(thd)_{3-x(s)} + xHthd_{(g)} \quad (5.1)$$

$$|\text{–}O_xY(thd)_{3-x(s)} + 1.5Qz_{(g)} \rightarrow |\text{–}O_xYQz_{1.5}H_{x(s)} + (3-x)Hthd_{(g)} \quad (5.2)$$

Where |– symbolizes the thin film, and x is the number of surface ligands $Y(thd)_3$ reacts with.

By solving for the observed Δm_1/ Δm_2 (see Appendix A:III.a)) we obtain x = 1.3, which is in accordance with a process that has enough ligands intact to ensure self-limiting growth.

Through the $Y(thd)_3$, Qz pulse and Qz purge, there is a slight decrease in the QCM response. This could be temperature drift in response to a reaction, or it could be a disturbance present throughout the measurement. There is no decrease during the $Y(thd)_3$ pulse, meaning $Y(thd)_3$ in some way is mitigating the drift. We did not perform a detailed investigation of the drift so we cannot be sure of its mechanism. It can have a small impact on the value of *x*, but the drift is quite weak, meaning the overall result is the same.

Hansen et al. deposited thin films of Al_2Qz_3 using TMA and Qz at a deposition temperature of 175 °C, obtaining a growth rate of around 0.3 Å/cycle [13]. They found slow saturation of Qz growth and over-stoichiometry of Al, indicating unreacted Al-CH_3 groups. They elucidated that this could be due to TMA coordinating and reacting with carbonyl groups [68]. In testing another Al-precursor they attempted $Al(acac)_3$, which is similar to thd in structure. However, they were unable to obtain any film. With their results in mind, it is surprising that we have achieved growth with $Ln(thd)_3$ and Qz, especially with such even films and high growth rates. TMA is pyrophoric, and reacts readily with water, as shown by the well-known deposition of Al_2O_3, given in Figure 2.7. Meanwhile, β-diketonates like thd generally react poorly with water, and are often combined with more aggressive oxidants like ozone when depositing oxides, indicating it is a fairly unreactive ligand [69]. In terms of pK_a values, Qz is around 10.8 for the first de-protonation and 12.0 for the second [70], while Hthd has a pK_a value of 11.6 [66]. In turn, the Al-CH_3 bonds in TMA are incredibly basic as the pK_a of CH_4 is around 48 [71]. The pK_a-value of acac is around 8.9 [72]. With the pK_a-values of Qz and Hthd being so similar, it could be that there is a low enough energy barrier for a statistically high enough exchange to occur, thus allowing for growth. Meanwhile for $Al(acac)_3$, Qz could struggle with replacing the ligands, as the Hacac molecules are more acidic than Hthd is. As there is no film growth using $Al(acac)_3$, this could hint at the exchange being more sensitive than expected.

5.2.2 Thin Film Structure

The investigations of Yb_2Qz_3 at different deposition temperatures in 4.2.5 indicated an ordering at lower temperatures from the bump in the XRD pattern, the increased roughness and the crystallites shown in AFM. The Y_2Qz_3 and Yb_2Qz_3 thin films in 4.2.6 showed high refractive indexes of around 1.97. This is quite close to Y_2O_3, which has an index of refraction of 1.92 at the same wavelength [73]. Even so, we can disprove growth of Y_2O_3 from the FTIR results in 4.2.2 which clearly show incorporation of Qz during growth.

Based on the QCM growth analysis, it is plausible that we are growing stoichiometric Y_2Qz_3, although we lack a proper chemical analysis. Growth of Al_2Qz_3 was earlier investigated with XPS in the work by Per-Anders Hansen, with TMA as Al-source [13]. Here, an over-stoichiometry of Al was observed, as well as an indication of many unreacted TMA-groups. This was also reflected in their QCM analysis. An XPS or Time-of-Flight Elastic Recoil Detection Analysis (ToF-ERDA) measurement would give insight into the true chemical composition of our thin film and verify its stoichiometry.

5.2.3 Optical properties of Ln_2Qz_3 films

The Ln_2Qz_3 thin films showed similar optical properties to Qz by itself, as indicated by FTIR and UV-Vis. This confirmed that Qz did work as an absorber when embedded in a thin film, and that its overall structure was intact. The UV-Vis in Figure 4.7 showed a redshift as Qz coordinated to Y^{3+} and Yb^{3+}. This is as expected as the cation-coordination leads to increased aromaticity by coordinating to both the alcohol and carbonyl of the Qz-molecule, and the absorption spectra of organic molecules redshift as the aromaticity increases [74].

None of the pure Ln_2Qz_3 films showed any luminescent activity, like for the powders made from evaporation of ethanol solutions. The reason is possibly ACQ, where the planar structure of Qz leads to stacking in the solid state. Modifications of the fluorescent molecules by altering the ligands have been explored when used in solutions, but this is outside the scope of this project [67]. To mitigate ACQ, we attempted to dilute Qz in a LnF_3 matrix , which will be further discussed after discussion of the deposition of pure LnF_3 films.

5.3 Deposition of LnF_3

5.3.1 NH_4F as a precursor

We chose to use treated NH_4F over untreated. The reason for this is that NH_4F is hygroscopic. As H_2O is a commonly used precursor in oxide growth, using NH_4F containing water could have the potential of growing oxides as well as fluorides. Since we want to avoid any growth of oxides, the choice of treated NH_4F was the safest. The QCM measurements showed that treated and untreated gave equal growth of YbF_3, which could indicate that the NH_4F was sufficiently dry even when stored in the normal container. The untreated powder tended to form hard clumps that would need to be broken up for use as a precursor, which could indicate that NH_4F in fact is absorbing moisture from the air. However, as shown in 4.3.7, YbF_3 with both treated and untreated NH_4F showed nearly identical refractive indexes of around 1.55, quite close to the reported value of 1.50 [75]. This is far from the refractive index of Yb_2O_3 around 1.94 [76], and indicates we are not growing oxide in any of our cases.

While we have not performed any characterization of chemical composition, Atosuo et al. investigated the impurities of GdF_3 deposited with Gd(thd) and NH_4F and found a low impurity of O, N, C and H with an increase for lower temperatures [6]. There was maximum 0.04 at.% of N across all their deposited films, which indicated that there were no reactions with NH_3 from the decomposition of NH_4. They had previously suspected that NH_4F seemed to lead to incorporation of Si in the film from etching of the Si-substrate, however, the content was very low at around 0.2 at.%, indicating it is not a large issue.

5.3.2 ALD Growth

The QCM investigation of YbF_3 in Figure 4.13 show clear saturation during pulses, and visible desorption during purges. This is a good indication of ALD growth. We can investigate the overall reaction mechanism by inspecting the relative mass increase during reaction of the individual reactants. This is presented as Δm_1 and Δm_2 in Figure 5.2, as the change in QCM response from the start of a precursor pulse to the end of its purge.

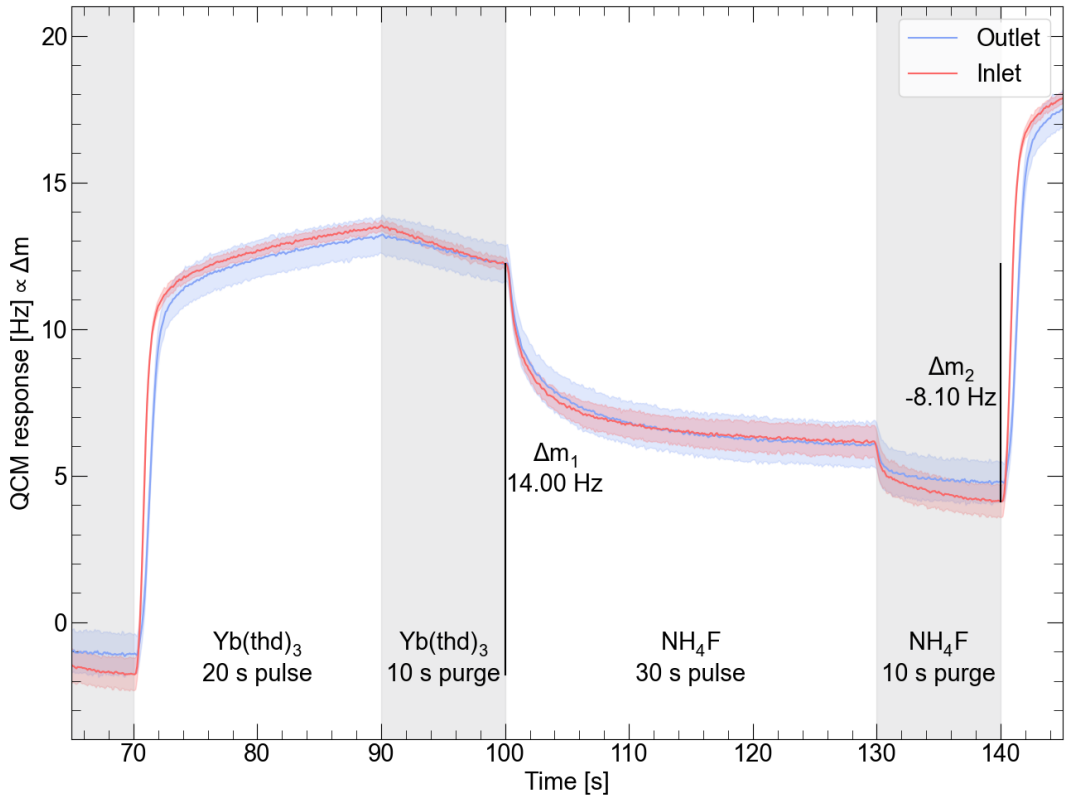

Figure 5.2: Average of 25 QCM long cycles for YbF_3 growth. The figure is marked with the relative increase for one $Y(thd)_3$ half-cycle (Δm_1) and one NH_4F half-cycle (Δm_2) for the inlet.

We observed an increase of 14.0 Hz during reaction of $Yb(thd)_3$, and a decrease of 8.1 Hz during reaction of NH_4F. This gives a $\Delta m_1/\Delta m_2$ of -1.73. This can be compared to the calculated mass change for a proposed reaction mechanism, which is given for the reactions of $Yb(thd)_3$ and HF below in Equation (5.3) and Equation (5.4), respectively. Note that since NH_4F decomposes to NH_3 and HF, and NH_3 does not seem to react, we have simplified the equation to HF.

$$\vdash(H)_{x(s)} + Yb(thd)_{3(g)} \rightarrow \vdash Yb(thd)_{3-x(s)} + xHthd_{(g)} \tag{5.3}$$

$$\vdash Yb(thd)_{3-x(s)} + 3HF_{(g)} \rightarrow \vdash YbF_3H_{x(s)} + (3-x)Hthd_{(g)} \tag{5.4}$$

Where ⊢ symbolizes the thin film, and *x* is the number of surface ligands $Yb(thd)_3$ reacts with.

By solving for a $\Delta m_1/\Delta m_2$ as observed, we obtain x = 0.96, i.e., very close to 1 (see Appendix A:III.b), which is required for a reaction mechanism where enough ligands remain to provide a self-limiting growth mechanism.

We can perform the same $\Delta m_1/\Delta m_2$-analysis on the QCM results for growth of NdF_3,TmF_3 and YF_3, obtaining *x*-values of approximately 2.7, 2.5 and 1.6, respectively. The long pulses of NdF_3 and TmF_3 in Figure 4.15 and Figure 4.17 do show low saturation of the cation pulses and there is likely something more than pure ALD-growth going on reaction-wise. With an *x*-value above 2, it could seem that some cation precursors react with all three ligands, or that a parasitic reaction where NH_4F is embedded or a reaction with a leak or other impurities are taking place. Despite these results, the refractive indexes are close to the expected values of around 1.5-1.6, which indicate fluoride growth [77]. The value for YF_3, is between 1 and 2, which is according to expectations for the expected reaction mechanism. There were some issues with the ALD reactor during the QCM measurements of NdF_3 and TmF_3, and this likely has had an impact on the results. Sørensen did not analyze growth of LnF_3 as thoroughly as we have done, but the results of her QCM analysis of YbF_3 is in accordance with our own [12].

The growth rate of LnF_3 by NH_4F is lower than most LnF_3 by TiF_4, as seen by Table 1.1 and Table 4.2. The growth rate for YF_3 grown by NH_4F is around one third when comparing to Pilvi et al. who grew YF_3 with TiF_4 [23]. This reduced growth is in accordance with what Atosuo et al. has reported [6]. They saw a GPC of 0.2 Å/cycle for GdF_3 by $Gd(thd)_3$ and NH_4F, being about one third of our growth rates of around 0.5 – 0.7 Å/cycle for LnF_3 by NH_4F. They experienced a relatively stable GPC with increasing deposition temperatures from 275 to 375 °C, while our investigation of YbF_3 with varying deposition temperatures show a strongly varying GPC from 175 to 300 °C as seen in Figure 4.20. However, we are focusing on growth at lower temperatures, where possibly amorphous growth occurs, rather than the higher temperatures investigated by Atosuo et al. with crystalline growth. It could be that our GPC flattens out above 300 °C.

5.3.3 Thin Film Structure

The structure of YbF_3 films deposited at different temperatures was investigated with XRD. This showed an amorphous growth at lower temperatures, supported by the low roughness and AFM images in Figure 4.22 and Figure 4.23. The growth transitioned as the temperature increased, with the clearest difference around 225 – 250 °C. The

films became more crystalline at higher temperatures, with XRD showing growth of crystalline YbF_3 (Pnma), as well as an unknown phase. Identifying the phase was not prioritized, but it was proven that it did not match Yb_2O_3. This increase in crystallinity for increased deposition temperatures is in accordance with the LnF_3 thin films from the literature in Table 1.1, though they do not observe the same change in growth rate over increasing deposition temperatures as we do.

We chose to investigate the growth of YbF_3 in more detail assuming the other LnF_3 films were similar. Table 4.2 indicates this could be true for TmF_3 and YF_3, as the roughness and refractive indexes are similar, but NdF_3 seems to grow in a very different way. This could be due to the larger size of Nd compared to the other cations. When growing Ln_2O_3 Hansen et al. obtained cubic crystal structures for all but Nd_2O_3, who grew in a hexagonal phase [22]. By investigating the QCM measurements we can obtain more insight, though it should be noted the ALD reactor had some issues with turbulence during the QCM measurements of NdF_3, TmF_3 and YF_3.

The QCM long pulses of YbF_3 and YF_3 show similar behavior, as seen when comparing Figure 4.12 and Figure 4.18, respectively. This could indicate that they have similar growth mechanisms, but there is a difference in their *x*-values from $\Delta m_1/\Delta m_2$-analysis being 1 for YbF_3 and 1.5 for YF_3. Thin films of YF_3 from $Y(thd)_3$ and NH_4F deposited at 350 °C have previously been analyzed with X-Ray Photoelectron Spectroscopy (XPS), indicating possible growth of $NH_4Y_2F_7$ or other $YF_3{\cdot}NH_4F$ compounds [12]. It could be that we are forming some of these materials as impurities, but the QCM analysis seems to indicate that the proposed reaction mechanisms for growth of YbF_3 fits well, meaning our main product is likely YF_3. This is also supported by our refractive index of 1.62 in Table 4.2 being so close to the reported value of 1.63 [78]. Due to the similar QCM response for YbF_3 and YF_3, we are likely growing YF_3, but a chemical analysis is necessary to confirm this.

Judging from the films in 4.2.6, TmF_3 to YbF_3 seem to indicate a similar growth. However, the QCM results and $\Delta m_1/\Delta m_2$-analysis do also indicate some differences. The turbulence issues with the ALD reactor could be a reason for the different pulsing behavior between YbF_3 in Figure 4.12 and TmF_3 in Figure 4.16.

When comparing NdF_3 to YbF_3, there are some large differences. NdF_3 is an outlier compared to all the other LnF_3-films, and do not indicate saturation even for the long pulse in Figure 4.15. The steep gradients experienced could point towards a decomposition, i.e., CVD-growth, fitting with the large roughness observed. CVD could come from decomposition of $Nd(thd)_3$, though that is unlikely as it has been used both at our temperature and higher previously without this being suspected [22] [12]. It is also unlikely that the precursor is too cold as there is rather too much growth than too little. There is a possibility that impurities are formed. When NH_4F was used to deposit GdF_3, there was an increase in impurities at lower temperatures [6]. However, as we have not performed any chemical analysis on our films, we cannot reach a conclusion from our results. Reactor issues are part of the reason, but there is likely an unknown reaction occurring during the growth of NdF_3.

5.4 Incorporation of Qz in YbF_3

After investigating Ln_2Qz_3-films and observing no luminescence the next step was to attempt dilution of Qz. With LnF_3-films characterized, we attempted to perform the dilution in a matrix of YbF_3, as that was our proposed matrix for the upconversion system (see 2.1.3). UV-Vis indicated that Qz did still absorb in dilution, but like for Ln_2Qz_3, we detected no luminescence. For the thin film with a dilution ratio between Yb_2Qz_3 and YbF_3 of 1:250, we have around 12.5 nm of separation between Qz-layers given the growth rate of 0.5 Å/cycle observed for YbF_3 in 4.3.7. This is large enough to assume it is outside the range of π-π stacking causing ACQ. The absorption spectrum in Figure 4.25 shows a very weak absorption, so the lack of luminescence could be from too weak absorption. The thin film with a dilution ratio of 1:50 has around 2.5 nm of separation. This film gave good absorption, but any excitation occurring was quenched before luminescence, like for the pure Yb_2Qz_3 films. For a benzene dimer, the π-π interaction has been simulated to give a separation of approximately 0.5 nm [79]. From 2.1.2, we know dipole-dipole interactions have a range of about 3.5 nm. Since ACQ is caused by π-π interactions and/or dipole-dipole interactions we cannot confirm that the 1:50 diluted thin film is separated enough, but more separation be at the expense of absorption. Even if the vertical separation is enough, there could easily be in-plane stacking occurring and causing ACQ. If in-plane dilution is possible to achieve by surface passivation using pulsing of other molecules, such as ethanol, this

could be worth a future investigation [80]. However, it would seem Qz is not well-suited as an organic sensitizer using the ALD method. Though Qz is not suitable in our upconversion system, the upconversion system itself was worth investigating.

5.5 Upconversion multilayer films

The CL measurements of YbF_3:Nd,Tm in Figure 4.26 showed a peak in intensity around 0.8 nm. This fits well with exchange interaction dropping quickly beyond 1 nm, and coulomb interactions of dipole-dipole and dipole-quadrupole having ranges of 3.5 and 0.8 nm, respectively. Quadrupole-quadrupole interactions have ranges of 0.2 nm, but it would seem to either not be a part of the mechanisms for energy transfer, or that it is mitigated by concentration quenching occurring at short distances. Longer distances likely lead to non-radiative decay. As Silje Sørensen showed, both Nd^{3+} and Tm^{3+} luminescence was present, and indicates that the upconversion system show good promise [12].

6 Conclusion

The luminescent properties of Qz have been investigated in ethanol solutions, showing activity with both Al^{3+} and Y^{3+}, but with quenched luminescence in solutions containing Hthd and thd^-, indicating a change for pH and possible formation of a charge transfer complex between the Qz and thd^-. Drying the luminescent solutions to a solid residue did not result in a luminescent material, most likely due to ACQ.

Ln_2Qz_3 thin films were deposited using $Y(thd)_3$ and $Yb(thd)_3$ with growth rates of 3.6 and 3.9 Å/cycle, respectively. This shows that the higher reactivity of thd-based precursors as compared to acac-based, is sufficient to obtain well defined growth by ALD. The deposited films were amorphous and showed that Ln_2Qz_3 was a plausible stoichiometry, with UV-Vis and FTIR confirming intact presence of Qz. No luminescence was observed, indicating that Qz must be diluted in a host matrix to be a sensitizer.

Thin films of LnF_3 were deposited with NH_4F as fluorine source, where pretreatment of NH_4F to avoid absorption of moisture was found to have little effect on the growth itself and the film properties. The films had a growth rate of around 0.6 Å/cycle with even gradients, except for NdF_3, which was an outlier compared to the other materials. YbF_3 showed a transition from growth of amorphous to crystalline material around 225 °C with increasing deposition temperatures. LnF_3 was a likely stoichiometry for our Yb and Y fluorides, while QCM investigations using Tm and Nd indicate a more complex type of growth, requiring more thorough analysis of the chemical composition.

Attempts to dilute Qz in LnF_3 show a correlation between the amount of Qz and its optical absorption. No luminescence was observed for any samples, and through investigation with varying degrees of dilution we discovered that the observed quenching could not be prevented without sacrificing the absorption to such a degree that the overall sensitization did not give any effect.

Optical investigation with CL was performed on YbF_3:Nd^{3+},Tm^{3+} thin films with varying Nd-Tm distances, where 0.8 nm gave the highest emission intensity. The upconversion process itself was not investigated, but with both Nd^{3+}- and Tm^{3+}-luminescence present, further work with the system and exploration with organic sensitizers show

great opportunities. Thus, despite lack of luminescence and upconversion in the current samples, our work shows that ALD is well suited for embedding organic molecules into inorganic materials to construct multilayered structures designed for optical conversion.

7 Future Perspectives

The thesis objective was to investigate Qz as an organic sensitizer in upconverting LnF_3 thin films. We learnt that Qz was not an ideal sensitizer, most probably due to self-quenching when embedded into the film structure. However, its growth with $Ln(thd)_3$ was an interesting discovery when considering that prior attempts with $Al(acac)_3$ have not led to any film. Such Ln_2Qz_3 films might prove useful for other applications. The project encompassed many areas, and while some properties were investigated deeply, others still remain for the future.

Firstly, the stoichiometry of Ln_2Qz_3 thin films were investigated with QCM, but chemical composition was not confirmed. If the film is to be investigated further, this should be confirmed using XPS or ToF-ERDA. The film has high absorption in the green area and could potentially function as a color filter. If there are other applications where these films can be used, the relevant properties will need to be characterized, such as porosity of the films by performing ellipsometric porosimetry and surface tension by performing contact angle measurements.

The LnF_3 system with $Ln(thd)_3$ and NH_4F was investigated thoroughly with QCM. YbF_3 was assumed to be representative of the other lanthanides used and was characterized at different deposition temperatures. A similar investigation for the other lanthanides will help reveal if this is true. NdF_3 especially has proven difficult, and deeper investigation of this material could highlight differences from other LnF_3 films.

Even in its diluted state, Qz did not show luminescence. With the likely culprit being ACQ, an investigation of in-plane dilution could reveal if ACQ can be avoided. Another possibility is the exploration of molecules with the opposite effect of aggregation-induced emission (AIE) [67]. Instead of strong emission in solution and weak in solid-state, these materials are weakly emitting in solution, but strongly in solid-state. Materials showcasing AIE generally do so due to restriction of intramolecular motions (RIM), being a combination of rotational and vibrational restrictions. By attaching side chains that can break up the planar structure of Qz, it could show AIE-like properties. If other dyes are to be investigated, it is recommended to look for volatile molecules already showcasing AIE, or with an existing modification process to promote AIE.

The multilayered structures have shown good promise for an upconversion system with YbF_3 as a host matrix. As both dopant incorporation and optimal distances have been investigated, the natural next step is to investigate if there is charge transfer between the different ions. A PL investigation of the deposited films would show if there is any optical conversion occurring.

In the end, the desire is an organic sensitized upconversion thin film that can be used in technologies requiring high-energy UV-radiation. An organic dye must be incorporated into the host matrix, with tuned absorption for the relevant application and successful energy transfer from the dye to the upconversion system. The upconversion itself must then be able to carry the transferred energy and lead to an upconverted emitted photon. By continuing the work outlined here, we are optimistic that an operational organic sensitized upconversion thin film can be created.

References

[1] E. Z. Xu, C. Lee, S. D. Pritzl, A. S. Chen, T. Lohmueller, B. E. Cohen, E. M. Chan, and P. J. Schuck, "(INVITED) Infrared-to-ultraviolet upconverting nanoparticles for COVID-19-related disinfection applications," *Optical Materials: X,* vol. 12, p. 100099, 2021/12/01/ 2021, doi: https://doi.org/10.1016/j.omx.2021.100099.

[2] N. Kandoth, S. Barman, A. Chatterjee, S. Sarkar, A. K. Dey, S. K. Pramanik, and A. Das, "Photoactive Lanthanide-Based Upconverting Nanoclusters for Antimicrobial Applications," *Advanced Functional Materials,* vol. 31, no. 43, p. 2104480, 2021, doi: https://doi.org/10.1002/adfm.202104480.

[3] B. S. Richards, D. Hudry, D. Busko, A. Turshatov, and I. A. Howard, "Photon Upconversion for Photovoltaics and Photocatalysis: A Critical Review," *Chemical Reviews,* vol. 121, no. 15, pp. 9165-9195, 2021/08/11 2021, doi: 10.1021/acs.chemrev.1c00034.

[4] Y. Shang, S. Hao, C. Yang, and G. Chen, "Enhancing Solar Cell Efficiency Using Photon Upconversion Materials," *Nanomaterials,* vol. 5, no. 4, pp. 1782-1809, 2015. [Online]. Available: https://www.mdpi.com/2079-4991/5/4/1782.

[5] M. Barawi, F. Fresno, R. Pérez-Ruiz, and V. A. de la Peña O'Shea, "Photoelectrochemical Hydrogen Evolution Driven by Visible-to-Ultraviolet Photon Upconversion," *ACS Applied Energy Materials,* vol. 2, no. 1, pp. 207-211, 2019/01/28 2019, doi: 10.1021/acsaem.8b01916.

[6] E. Atosuo, K. Mizohata, M. Mattinen, M. Mäntymäki, M. Vehkamäki, M. Leskelä, and M. Ritala, "Atomic layer deposition of GdF3 thin films," *Journal of Vacuum Science & Technology A,* vol. 40, no. 2, p. 022402, 2022, doi: 10.1116/6.0001629.

[7] X. Chen, L. Jin, W. Kong, T. Sun, W. Zhang, X. Liu, J. Fan, S. F. Yu, and F. Wang, "Confining energy migration in upconversion nanoparticles towards deep ultraviolet lasing," *Nature Communications,* vol. 7, no. 1, p. 10304, 2016/01/07 2016, doi: 10.1038/ncomms10304.

[8] X. Liu, C.-H. Yan, and J. A. Capobianco, "Photon upconversion nanomaterials," *Chemical Society Reviews,* 10.1039/C5CS90009C vol. 44, no. 6, pp. 1299-1301, 2015, doi: 10.1039/C5CS90009C.

[9] F. Wang, R. Deng, J. Wang, Q. Wang, Y. Han, H. Zhu, X. Chen, and X. Liu, "Tuning upconversion through energy migration in core–shell nanoparticles," *Nature Materials,* vol. 10, no. 12, pp. 968-973, 2011/12/01 2011, doi: 10.1038/nmat3149.

[10] W. Zou, C. Visser, J. A. Maduro, M. S. Pshenichnikov, and J. C. Hummelen, "Broadband dye-sensitized upconversion of near-infrared light," *Nature Photonics,* vol. 6, no. 8, pp. 560-564, 2012/08/01 2012, doi: 10.1038/nphoton.2012.158.

[11] G. Chen, J. Damasco, H. Qiu, W. Shao, T. Y. Ohulchanskyy, R. R. Valiev, X. Wu, G. Han, Y. Wang, C. Yang, H. Ågren, and P. N. Prasad, "Energy-Cascaded Upconversion in an Organic Dye-Sensitized Core/Shell Fluoride Nanocrystal," *Nano Letters,* vol. 15, no. 11, pp. 7400-7407, 2015/11/11 2015, doi: 10.1021/acs.nanolett.5b02830.

[12] S. H. Sørensen, P. A. Hansen, and O. nilsen, "Organic Sensitization in Lanthanide Fluoride Nanostructures for Upconversion," Master, University of Oslo, 2020. [Online]. Available: http://urn.nb.no/URN:NBN:no-82846

[13] P. A. Hansen and O. Nilsen, "Quinizarin: a large aromatic molecule well suited for atomic layer deposition," *Dalton Trans,* vol. 50, no. 24, pp. 8307-8313, Jun 22 2021, doi: 10.1039/d1dt00683e.
[14] J. N. Kvalvik, K. B. Kvamme, K. Almaas, A. Ruud, H. H. Sønsteby, and O. Nilsen, "LiF by atomic layer deposition—Made easy," *Journal of Vacuum Science & Technology A,* vol. 38, no. 5, p. 050401, 2020, doi: 10.1116/6.0000314.
[15] P.-A. Hansen, T. Zikmund, T. Yu, J. N. Kvalvik, T. Aarholt, Ø. Prytz, A. Meijerink, and O. Nilsen, "Single-step approach to sensitized luminescence through bulk-embedded organics in crystalline fluorides," *Communications Chemistry,* vol. 3, no. 1, p. 162, 2020/11/10 2020, doi: 10.1038/s42004-020-00410-0.
[16] R. L. Puurunen, "A Short History of Atomic Layer Deposition: Tuomo Suntola's Atomic Layer Epitaxy," *Chem. Vap. Deposition,* vol. 20, no. 10-11-12, pp. 332-344, 2014, doi: 10.1002/cvde.201402012.
[17] T. Suntola and J. Antson, "Method for producing compound thin films," Patent US4058430A, 1977.
[18] A. Pakkala and M. Putkonen, "Chapter 8 - Atomic Layer Deposition," in *Handbook of Deposition Technologies for Films and Coatings (Third Edition)*, P. M. Martin Ed. Boston: William Andrew Publishing, 2010, pp. 364-391.
[19] S. M. George, "Atomic Layer Deposition: An Overview," *Chemical Reviews,* vol. 110, no. 1, pp. 111-131, 2010/01/13 2010, doi: 10.1021/cr900056b.
[20] J. Päiväsaari, M. Putkonen, and L. Niinistö, "A comparative study on lanthanide oxide thin films grown by atomic layer deposition," *Thin Solid Films,* vol. 472, no. 1, pp. 275-281, 2005/01/24/ 2005, doi: https://doi.org/10.1016/j.tsf.2004.06.160.
[21] Atomiclimits. "Database of ALD processes." This work is licensed under a Creative Commons Attribution 4.0 International License <http://creativecommons.org/licenses/by/4.0/>. https://doi.org/10.6100/alddatabase (accessed May 13, 2022).
[22] P.-A. Hansen, H. Fjellvåg, T. Finstad, and O. Nilsen, "Structural and optical properties of lanthanide oxides grown by atomic layer deposition (Ln = Pr, Nd, Sm, Eu, Tb, Dy, Ho, Er, Tm, Yb)," *Dalton Transactions,* 10.1039/C3DT51270C vol. 42, no. 30, pp. 10778-10785, 2013, doi: 10.1039/C3DT51270C.
[23] T. Pilvi, E. Puukilainen, F. Munnik, M. Leskelä, and M. Ritala, "ALD of YF3 Thin Films from TiF4 and Y(thd)3 Precursors," *Chemical Vapor Deposition,* vol. 15, no. 1-3, pp. 27-32, 2009, doi: https://doi.org/10.1002/cvde.200806721.
[24] T. Pilvi, E. Puukilainen, K. Arstila, M. Leskelä, and M. Ritala, "Atomic Layer Deposition of LaF3 Thin Films using La(thd)3 and TiF4 as Precursors," *Chemical Vapor Deposition,* vol. 14, no. 3-4, pp. 85-91, 2008, doi: https://doi.org/10.1002/cvde.200706681.
[25] E. Atosuo, J. Ojala, M. J. Heikkilä, M. Mattinen, K. Mizohata, J. Räisänen, M. Leskelä, and M. Ritala, "Atomic layer deposition of TbF3 thin films," *Journal of Vacuum Science & Technology A,* vol. 39, no. 2, p. 022404, 2021, doi: 10.1116/6.0000790.
[26] V. Miikkulainen, M. Leskelä, M. Ritala, and R. L. Puurunen, "Crystallinity of inorganic films grown by atomic layer deposition: Overview and general trends," *Journal of applied physics,* vol. 113, no. 2, p. 21301, 2013, doi: 10.1063/1.4757907.

[27] Y. Lee, H. Sun, M. J. Young, and S. M. George, "Atomic Layer Deposition of Metal Fluorides Using HF–Pyridine as the Fluorine Precursor," *Chemistry of Materials,* vol. 28, no. 7, pp. 2022-2032, 2016/04/12 2016, doi: 10.1021/acs.chemmater.5b04360.
[28] M. Ylilammi and T. Ranta-aho, "Metal Fluoride Thin Films Prepared by Atomic Layer Deposition," *Journal of The Electrochemical Society,* vol. 141, no. 5, pp. 1278-1284, 1994/05/01 1994, doi: 10.1149/1.2054910.
[29] I. A. Wiik, P. A. Hansen, and O. Nilsen, "Light Conversion Materials for Solar Cell Applications - Synthesis and Characterisation of Lanthanide Fluoride Thin Films by Atomic Layer Deposition," Master, University of Oslo, 2016. [Online]. Available: http://urn.nb.no/URN:NBN:no-54852
[30] T. Pilvi, E. Puukilainen, U. Kreissig, M. Leskelä, and M. Ritala, "Atomic Layer Deposition of MgF2 Thin Films Using TaF5 as a Novel Fluorine Source," *Chemistry of Materials,* vol. 20, no. 15, pp. 5023-5028, 2008/08/01 2008, doi: 10.1021/cm800948k.
[31] N. Hornsveld, W. M. M. Kessels, R. A. Synowicki, and M. Creatore, "Atomic layer deposition of LiF using LiN(SiMe3)2 and SF6 plasma," *Physical Chemistry Chemical Physics,* 10.1039/D0CP05428C vol. 23, no. 15, pp. 9304-9314, 2021, doi: 10.1039/D0CP05428C.
[32] M. F. J. Vos, H. C. M. Knoops, R. A. Synowicki, W. M. M. Kessels, and A. J. M. Mackus, "Atomic layer deposition of aluminum fluoride using Al(CH3)3 and SF6 plasma," *Applied Physics Letters,* vol. 111, no. 11, p. 113105, 2017, doi: 10.1063/1.4998577.
[33] M. Putkonen, A. Szeghalmi, E. Pippel, and M. Knez, "Atomic layer deposition of metal fluorides through oxide chemistry," *Journal of Materials Chemistry,* vol. 21, no. 38, pp. 14461-14465, 2011, doi: 10.1039/C1JM11825K.
[34] O. Tiurin, N. Solomatin, M. Auinat, and Y. Ein-Eli, "Atomic layer deposition (ALD) of lithium fluoride (LiF) protective film on Li-ion battery LiMn1.5Ni0.5O4 cathode powder material," *Journal of Power Sources,* vol. 448, p. 227373, 2020/02/01/ 2020, doi: https://doi.org/10.1016/j.jpowsour.2019.227373.
[35] F. Helmer and O. Nilsen, "Thin films prepared with gas phase deposition technique," Norway Patent NO20045674D0, 2004.
[36] P. Sundberg and M. Karppinen, "Organic and inorganic–organic thin film structures by molecular layer deposition: A review," *Beilstein journal of nanotechnology,* vol. 5, no. 1, pp. 1104-1136, 2014.
[37] M. Tuomisto, Z. Giedraityte, L. Mai, A. Devi, V. Boiko, K. Grzeszkiewicz, D. Hreniak, M. Karppinen, and M. Lastusaari, "Up-converting ALD/MLD thin films with Yb3+, Er3+ in amorphous organic framework," *Journal of Luminescence,* vol. 213, pp. 310-315, 2019/09/01/ 2019, doi: https://doi.org/10.1016/j.jlumin.2019.05.028.
[38] J. Emsley, *The shocking history of phosphorus : a biography of the Devil's element*. London: Macmillan, 2000.
[39] C. R. Ronda, *Luminescence : from theory to applications*. Weinheim: Wiley-VCH, 2008, pp. xv, 260 p.
[40] F. Vetrone and J. A. Capobianco, "Lanthanide-doped fluoride nanoparticles: luminescence, upconversion, and biological applications," *International Journal of Nanotechnology,* vol. 5, no. 9-12, pp. 1306-1339, 2008, doi: 10.1504/ijnt.2008.01984.
[41] X. Wang, R. R. Valiev, T. Y. Ohulchanskyy, H. Ågren, C. Yang, and G. Chen, "Dye-sensitized lanthanide-doped upconversion nanoparticles," *Chemical*

Society Reviews, 10.1039/C7CS00053G vol. 46, no. 14, pp. 4150-4167, 2017, doi: 10.1039/C7CS00053G.
[42] R. Naccache, Q. Yu, and J. A. Capobianco, "The Fluoride Host: Nucleation, Growth, and Upconversion of Lanthanide-Doped Nanoparticles," *Advanced Optical Materials,* vol. 3, no. 4, pp. 482-509, 2015, doi: https://doi.org/10.1002/adom.201400628.
[43] J. W. Stouwdam and F. C. J. M. van Veggel, "Near-infrared Emission of Redispersible Er3+, Nd3+, and Ho3+ Doped LaF3 Nanoparticles," *Nano Letters,* vol. 2, no. 7, pp. 733-737, 2002/07/01 2002, doi: 10.1021/nl025562q.
[44] J.-H. Zeng, J. Su, Z.-H. Li, R.-X. Yan, and Y.-D. Li, "Synthesis and Upconversion Luminescence of Hexagonal-Phase NaYF4:Yb, Er3+ Phosphors of Controlled Size and Morphology," *Advanced Materials,* vol. 17, no. 17, pp. 2119-2123, 2005, doi: https://doi.org/10.1002/adma.200402046.
[45] G. Chen, T. Y. Ohulchanskyy, A. Kachynski, H. Ågren, and P. N. Prasad, "Intense Visible and Near-Infrared Upconversion Photoluminescence in Colloidal LiYF4:Er3+ Nanocrystals under Excitation at 1490 nm," *ACS nano,* vol. 5, no. 6, pp. 4981-4986, 2011, doi: 10.1021/nn201083j.
[46] W. Yang, X. Li, D. Chi, H. Zhang, and X. Liu, "Lanthanide-doped upconversion materials: emerging applications for photovoltaics and photocatalysis," *Nanotechnology,* vol. 25, no. 48, p. 482001, 2014/11/14 2014, doi: 10.1088/0957-4484/25/48/482001.
[47] D. M. Bubb, D. Cohen, and S. B. Qadri, "Infrared-to-visible upconversion in thin films of LaEr(MoO4)3," *Applied Physics Letters,* vol. 87, no. 13, p. 131909, 2005, doi: 10.1063/1.2067712.
[48] X. Zhang, C. Serrano, E. Daran, F. Lahoz, G. Lacoste, and A. Muñoz-Yagüe, "Infrared-laser-induced upconversion from Nd3+:LaF3 heteroepitaxial layers on CaF2 (111) substrates by molecular beam epitaxy," *Physical Review B,* vol. 62, no. 7, pp. 4446-4454, 08/15/ 2000, doi: 10.1103/PhysRevB.62.4446.
[49] C. Lin, M. T. Berry, R. Anderson, S. Smith, and P. S. May, "Highly Luminescent NIR-to-Visible Upconversion Thin Films and Monoliths Requiring No High-Temperature Treatment," *Chemistry of Materials,* vol. 21, no. 14, pp. 3406-3413, 2009/07/28 2009, doi: 10.1021/cm901094m.
[50] G. Dingemans, A. Clark, J. A. v. Delft, M. C. M. v. d. Sanden, and W. M. M. Kessels, "Er3+ and Si luminescence of atomic layer deposited Er-doped Al2O3 thin films on Si(100)," *Journal of Applied Physics,* vol. 109, no. 11, p. 113107, 2011, doi: 10.1063/1.3595691.
[51] L.-J. Xu, G.-T. Xu, and Z.-N. Chen, "Recent advances in lanthanide luminescence with metal-organic chromophores as sensitizers," *Coordination Chemistry Reviews,* vol. 273-274, pp. 47-62, 2014/08/15/ 2014, doi: https://doi.org/10.1016/j.ccr.2013.11.021.
[52] Z. Giedraityte, M. Tuomisto, M. Lastusaari, and M. Karppinen, "Three- and Two-Photon NIR-to-Vis (Yb,Er) Upconversion from ALD/MLD-Fabricated Molecular Hybrid Thin Films," *ACS Applied Materials & Interfaces,* vol. 10, no. 10, pp. 8845-8852, 2018/03/14 2018, doi: 10.1021/acsami.7b19303.
[53] O. J. Svendsen, P. A. Hansen, and O. Nilsen, "Nedskifting av lys med tynne filmer," Master, University of Oslo, 2014. [Online]. Available: http://urn.nb.no/URN:NBN:no-44143
[54] Y. Wang, K. Zheng, S. Song, D. Fan, H. Zhang, and X. Liu, "Remote manipulation of upconversion luminescence," *Chemical Society Reviews,* vol. 47, no. 17, pp. 6473-6485, 2018, doi: 10.1039/C8CS00124C.

[55] Ingrid Vee, K. B. Klepper, P. A. Hansen, H. Fjellvåg, and O. Nilsen, "Fluorholdige hybridmaterialer med atomlagsavsetting : Syntese og karakterisering," Master, University of Oslo, 2012. [Online]. Available: http://urn.nb.no/URN:NBN:no-32992

[56] A. Brennhagen, K. B. Kvamme, K. S. S. Sverdlilje, and O. Nilsen, "Synthesis and electrochemical characterization of thin film iron phosphates as cathode material for Li-ion batteries," Master, University of Oslo, 2019. [Online]. Available: http://urn.nb.no/URN:NBN:no-73667

[57] H. Fujiwara and I. Wiley, *Spectroscopic ellipsometry : principles and applications*. Chichester, England ; Hoboken, NJ: John Wiley & Sons (in English), 2007.

[58] Y. Leng, *Materials Characterization: Introduction to Microscopic and Spectroscopic Methods, Second Edition*, Second ed. Wiley-VCH, 2013.

[59] D. M. Jens Als-Nielsen, *Elements of Modern X-ray Physics*, Second Edition ed. 2011.

[60] P. K. David Nečas. "Gwyddion User Guide: Statistical Analysis." http://gwyddion.net/documentation/user-guide-en/statistical-analysis.html (accessed 09.04.2022.

[61] G. Sauerbrey, "Verwendung von Schwingquarzen zur Wägung dünner Schichten und zur Mikrowägung," *Zeitschrift für Physik,* vol. 155, no. 2, pp. 206-222, 1959/04/01 1959, doi: 10.1007/BF01337937.

[62] E. T. North. "E.T.North-MSc.ThesisCode." Github. https://github.com/CyberMancerGamer/E.T.North-MSc.ThesisCode (accessed May 15, 2022).

[63] D. Nečas and P. Klapetek, "Gwyddion: an open-source software for SPM data analysis," *Open Physics,* vol. 10, no. 1, pp. 181-188, 2012, doi: doi:10.2478/s11534-011-0096-2.

[64] J. W. Sons. "1,4-Dihydroxyanthraquinone - FTIR - Spectrum - SpectraBase." Inc. SpectraBase. https://spectrabase.com/spectrum/6bxGJZ9BHEf (accessed May 4, 2022).

[65] J. Guo, Z. Kuai, Z. Zhang, Q. Yang, Y. Shan, and Y. Li, "A simple colorimetric and fluorescent probe with high selectivity towards cysteine over homocysteine and glutathione," *RSC Advances,* 10.1039/C6RA28829D vol. 7, no. 31, pp. 18867-18873, 2017, doi: 10.1039/C6RA28829D.

[66] ChemicalBook. "2,2,6,6-TETRAMETHYL-3,5-HEPTANEDIONE | 1118-71-4." ChemicalBook. https://www.chemicalbook.com/ChemicalProductProperty_EN_CB1373637 (accessed May 3, 2022).

[67] Q. Zhao and J. Z. Sun, "Red and near infrared emission materials with AIE characteristics," *Journal of Materials Chemistry C,* 10.1039/C6TC03359H vol. 4, no. 45, pp. 10588-10609, 2016, doi: 10.1039/C6TC03359H.

[68] Y. Kwon, O. Scadeng, R. McDonald, and F. G. West, "α-Hydroxycyclopentanones via one-pot oxidation of the trimethylaluminum-mediated Nazarov reaction with triplet oxygen," *Chemical Communications,* vol. 50, no. 42, pp. 5558-5560, 2014, doi: 10.1039/C4CC02330G.

[69] T. Hatanpää, M. Ritala, and M. Leskelä, "Precursors as enablers of ALD technology: Contributions from University of Helsinki," *Coordination Chemistry Reviews,* vol. 257, no. 23, pp. 3297-3322, 2013/12/01/ 2013, doi: https://doi.org/10.1016/j.ccr.2013.07.002.

[70] A. K. Rivas-Sánchez, D. S. Guzmán-Hernández, M. T. Ramírez-Silva, M. Romero-Romo, and M. Palomar-Pardavé, "Quinizarin characterization and quantification in aqueous media using UV-VIS spectrophotometry and cyclic voltammetry," *Dyes and Pigments,* vol. 184, p. 108641, 2021/01/01/ 2021, doi: https://doi.org/10.1016/j.dyepig.2020.108641.
[71] K. J. Blakeney, "Synthesis Of Volatile And Thermally Stable Aluminum Hydride Complexes And Their Use In Atomic Layer Deposition Of Metal Thin Films," Wayne State University, 2018.
[72] "Acetylacetone | C5H8O2 - PubChem." National Center for Biotechnology Information (2022). PubChem Compound Summary for CID 31261. https://pubchem.ncbi.nlm.nih.gov/compound/Acetylacetone (accessed May 14, 2022).
[73] Y. Nigara, "Measurement of the Optical Constants of Yttrium Oxide," *Japanese Journal of Applied Physics,* vol. 7, no. 4, pp. 404-408, 1968/04 1968, doi: 10.1143/jjap.7.404.
[74] Y. Xu, Q. Chu, D. Chen, and A. Fuentes, "HOMO–LUMO Gaps and Molecular Structures of Polycyclic Aromatic Hydrocarbons in Soot Formation," (in English), *Frontiers in Mechanical Engineering,* Original Research vol. 7, 2021-November-17 2021, doi: 10.3389/fmech.2021.744001.
[75] T. Amotchkina, M. Trubetskov, D. Hahner, and V. Pervak, "Characterization of e-beam evaporated Ge, YbF3, ZnS, and LaF3 thin films for laser-oriented coatings," *Appl. Opt.,* vol. 59, no. 5, pp. A40-A47, 2020/02/10 2020, doi: 10.1364/AO.59.000A40.
[76] O. Medenbach, D. Dettmar, R. D. Shannon, R. X. Fischer, and W. M. Yen, "Refractive index and optical dispersion of rare earth oxides using a small-prism technique," *Journal of Optics A: Pure and Applied Optics,* vol. 3, no. 3, pp. 174-177, 2001/03/14 2001, doi: 10.1088/1464-4258/3/3/303.
[77] R. Laiho and M. Lakkisto, "Investigation of the refractive indices of LaF3, CeF3, PrF3 and NdF3," *Philosophical Magazine B,* vol. 48, no. 2, pp. 203-207, 1983/08/01 1983, doi: 10.1080/13642818308226470.
[78] D. F. Bezuidenhout, K. D. Clarke, and R. Pretorius, "The optical properties of YF3 films," *Thin Solid Films,* vol. 155, no. 1, pp. 17-30, 1987/12/15/ 1987, doi: https://doi.org/10.1016/0040-6090(87)90449-4.
[79] M. O. Sinnokrot, E. F. Valeev, and C. D. Sherrill, "Estimates of the ab initio limit for pi-pi interactions: the benzene dimer," *J Am Chem Soc,* vol. 124, no. 36, pp. 10887-93, Sep 11 2002, doi: 10.1021/ja025896h.
[80] L. Hu, W. Qi, and Y. Li, "Coating strategies for atomic layer deposition," *Nanotechnology Reviews,* vol. 6, no. 6, pp. 527-547, 2017, doi: doi:10.1515/ntrev-2017-0149.

Appendix A: Calculations

I. QCM response

QCM response is exported in Hz, but can often give more information by converting it to mass per area per cycle. By correcting for drift a more accurate result can be obtained, and using density of the thin film we can convert Hz to $^{ng}/_{cm^3 \cdot cycle}$.

Firstly, the direct QCM response is multiplied by a correction factor. This correction factor is a polynomial fit to the responses given for each buffer layer in the QCM deposition. By performing this multiplication, all responses are normalized to one buffer layer. The next step is determining the mass involved in deposition of one such buffer layer.

We assume a substrate being deposited as a monolayer of a film with density, ρ, and growth per cycle, g. The QCM response given as mass per cycle per area of can then be calculated using the following formula:

$$Response = \rho \cdot g$$

As an example, YbF_3 has a density of 6.98 g/cm^3 and a GPC of 0.545 nm/cycle. The formula is then:

$$6.98 \cdot 0.545 \cdot {}^{g \cdot nm}/_{cm^3 \cdot cycle} = 3.80 \, {}^{g \cdot nm}/_{cm^3 \cdot cycle}$$

Adjusting for units:

$$1\, nm = 10^{-7}\, cm, 1\, g = 10^9\, ng \rightarrow 10^{-7}\, cm \cdot 10^9\, ng = 100\, ng \cdot cm$$

We finally obtain:

$$100 \cdot 3.80 \, {}^{g \cdot nm}/_{cm^3 \cdot cycle} = \mathbf{380} \, {}^{\boldsymbol{ng}}/_{\boldsymbol{cycle \cdot cm^2}}$$

By multiplying this to the correction factor, we can obtain the mass deposited per cycle, instead of the frequency per cycle.

II. Ethanol solution pH

Our ethanol solutions containing Qz seemed to show a change in luminescence depending on the pH. The following sections calculate the estimated pH of the solutions as if the solvent was water.

a. Hthd solutions

The ethanol solutions contained 10^{-3} M Hthd, which has a pKa of 11.60. *pKa* is related to Ka using the following equation:

$$pKa = -\log(Ka)$$

This means that *Ka* would be $2.5 \cdot 10^{-12}$. Using the equation for *Ka* we can insert our concentrations and calculate:

$$Ka = 2.5 \cdot 10^{-12} = \frac{[H^+][thd^-]}{[Hthd]}$$

We make a table showing the changes in concentration as Hthd interacts with the solution:

	$[Hthd]$	H^+	$[thd^-]$
Before	10^{-3}	0	0
Change	$-x$	x	x
Equilibrium	$10^{-3} - x$	x	x

We want to solve for x at the equilibrium and so place this in the equation for *Ka*:

$$2.5 \cdot 10^{-12} = \frac{x \cdot x}{10^{-3} - x}$$

$$2.5 \cdot 10^{-12}(10^{-3} - x) = x^2$$

$$x^2 + 2.5 \cdot 10^{-12}x - 2.5 \cdot 10^{-15} = 0$$

This gives us $x = 5 \cdot 10^{-8}$ and $pH = -\log(5 \cdot 10^{-8}) = 7.3$

Since x is small for weak acids we could also simplify it to:

$$2.5 \cdot 10^{-12} = \frac{x \cdot x}{10^{-3}}$$

$$x^2 = 2.5 \cdot 10^{-15}$$

$$x = \sqrt{2.5 \cdot 10^{-15}} = 5 \cdot 10^{-8}$$

We can then calculate the pH to be:

$$\boldsymbol{pH = -\log(5 \cdot 10^{-8}) = 7.3}$$

b. thd$^-$-solutions

The pK_b-value of thd$^-$ can be calculated from the pK_a of Hthd, 11.60:

$$pK_a + pK_b = 14$$

$$pK_b = 14 - 11.6 = 2.4$$

This gives thd a K_b of $10^{-2.4} \approx 4 \cdot 10^{-3}$, and is defined as:

$$K_b = \frac{[OH^-][Hthd]}{[thd^-]}$$

The change in concentrations can be seen using the table below:

	$[thd^-]$	OH^-	$[Hthd]$
Before	10^{-3}	0	0
Change	$-x$	x	x
Equilibrium	$10^{-3} - x$	x	x

Inserting the values at equilibrium we obtain:

$$4 \cdot 10^{-3} = \frac{x^2}{10^{-3} - x}$$

This can be reordered as a quadratic formula:

$$4 \cdot 10^{-3}(10^{-3} - x) = x^2$$

$$x^2 + 4 \cdot 10^{-3}x - 4 \cdot 10^{-6} = 0$$

Solving the quadratic formula gives $x \approx 8.3 \cdot 10^{-4}$, leading to a value for pOH:

$$pOH = -\log(8.3 \cdot 10^{-4}) \approx 3.1$$

From here we can calculate the pH:

$$pOH + pH = 14$$

$$\boldsymbol{pH = 14 - 3.1 = 10.9}$$

III. $\Delta m_1/\Delta m_2$ analysis

To obtain more information from a QCM analysis, we can compare the mass gains for the half cycles to see if it matches with a proposed reaction mechanism. The mass gain for the reactions belonging to each half cycles is defined, and an equation set is solved in order to obtain a value, *x*, representing the number of surface ligands our thd-compounds react with.

a. Y_2Qz_3

The mass change can be calculated as below by observing the reactions in Equation (5.1) and Equation (5.2):

$$\Delta m_1 = M_r(Y(thd)_3) - xM_r(Hthd)$$

$$\Delta m_2 = 1.5 \cdot M_r(H_2Qz) - (3 - x)M_r(Hthd)$$

Since we want to find a value of x that corresponds to our observed values, we can combine the formulas, insert our values and solve for x:

$$\frac{\Delta m_1}{\Delta m_2} = \frac{M_r(Y(thd)_3) - xM_r(Hthd)}{1.5 \cdot M_r(H_2Qz) - (3 - x)M_r(Hthd)}$$

$$x = \frac{M_r(Y(thd)_3) + \left(3M_r(Hthd) - 1.5M_r(H_2Qz)\right)\frac{\Delta m_1}{\Delta m_2}}{\left(\frac{\Delta m_1}{\Delta m_2} + 1\right)M_r(Hthd)}$$

We insert the molecular weights from the table below along with our experimental value for $\frac{\Delta m_1}{\Delta m_2} = \frac{9.05}{0.82}$.

Molecule	M_r [g/mol]
$Y(thd)_3$	638.71
Hthd	184.28
H_2Qz	240.21

This gives *x* a value of 1.3.

b. YbF_3

The mass changes are calculated as follows from Equation (5.3) and Equation (5.4):

$$\Delta m_1 = M_r(Yb(thd)_3) - xM_r(Hthd)$$

$$\Delta m_2 = 3M_r(HF) - (3-x)M_r(Hthd)$$

These are combined to and then simplified to:

$$\frac{\Delta m_1}{\Delta m_2} = \frac{M_r(Yb(thd)_3) - xM_r(Hthd)}{3M_r(HF) - (3-x)M_r(Hthd)}$$

$$x = \frac{M_r(Yb(thd)_3) + \left(M_r(Hthd) - M_r(HF)\right)3\frac{\Delta m_1}{\Delta m_2}}{\left(\frac{\Delta m_1}{\Delta m_2} + 1\right)M_r(Hthd)}$$

Where the value of $\frac{\Delta m_1}{\Delta m_2} = \frac{14.00}{-8.10}$ is inserted along with the molecular weights in the table below.

Molecule	M_r [g/mol]
$Yb(thd)_3$	722.86
Hthd	184.28
HF	20.01

This gives *x* a value of 0.96, close to 1.0.